Vibrational spectroscopy and the structure of solids: The example of carbonate minerals

by

© **Stephen Campbell**

A thesis submitted to the School of Graduate Studies in partial fulfillment of the requirements for the degree of Doctor of Philosophy.

Department of Physics and Physical Oceanography

Memorial University

August 2023

St. John's, Newfoundland and Labrador, Canada

Abstract

Studying material structure on the atomic scale in solids can give clues as to how that material was formed, aged, or used. Atoms in solids are constantly in motion. A material's specific composition and crystal arrangement results in a unique profile of atomic vibrations. These vibrations, or modes, can be grouped into two main types; internal modes are higher energy vibrations related to atomic motion of single atoms or moieties within the unit cell, whereas external modes are lower in energy and correspond to the collective movement of multiple coordinated atoms or moieties. Past investigations focused on the vibrations of solids have explored the effect of crystalline ordering on internal modes both experimentally and computationally. In this thesis, I explore the viability of established experimental and computational methods to examine the influence of structural differences on the the external mode vibrations using calcium carbonate as a case study material. The experimental projects focus on infrared spectroscopy. This tool is sensitive enough to observe subtle differences in the internal modes that are linked to structural differences but has yet to be explored for the external modes.

We study calcium carbonate systems using infrared spectroscopic methods to understand the impact of structure on vibrational properties. Our initial goal was to correlate novel external mode vibration data trends with the established understanding of internal mode changes and atomic structure data. We found that the broadness of the external modes makes extracting structural information using the previous analysis protocols impractical. The results highlight potential pitfalls for researchers who are new to these spectroscopic techniques. We preach caution when attempting to interpret energy shifts of external modes as structural differences amongst samples without correlating with additional experimental methods.

Further experiments focused on photoacoustic infrared spectroscopy, a specialized version of the technique. Previous works have highlighted but failed to explain how this specialized setup can enhance the detection of weak internal modes. We sought to determine the mechanism for this documented phenomenon. While we could not identify the cause of the enhancement, our experiments and analysis showed that it is intrinsic to the photoacoustic method and eliminated detector saturation, often thought to be the cause, as the root mechanism.

Finally, I used computational molecular dynamics methods to simulate calcium carbonate vibrations. Using previously published parameters, I was able to generate a vibrational density of states (VDOS) for the calcium carbonate polymorph aragonite. This work is valuable as alternative computational methods to simulate the external vibrations of calcium carbonates are computationally expensive. The computed VDOS of aragonite shows a reasonable level of qualitative agreement with experimental measurements. This work serves as a proof-of-concept and starting point to observe disorder's effects on the calculated vibrational density of states.

For Regan, and our future together.

Acknowledgements

I want to express my heartfelt appreciation to my supervisor, Dr. Kristin M. Poduska, for her seemingly endless supply of support, encouragement, and kindness. This document only exists because of her guidance, patience, and innate ability to draw out my research potential.

Further, I would like to thank the Poduska group, past and present. Their support, ideas, samples, and goodwill will forever exist on these pages. I want to thank Dr. Kirk Michaelian for his invaluable insight into all things photoacoustic, Dr. Wanda Aylward for the collection of PXRD data, Drs. Ivan Saika-Voivod and Shahrazad Malek for the crash course in molecular dynamics simulation, and Drs. Alison Malcolm and James LeBlanc for serving as my supervisory committee.

To my beloved wife, Regan, parents, Karen and Michael, and sister, Emily, you have supported me my whole life. Without each of you, this would have been impossible.

Lastly, I thank the financial support from Natural Sciences and Engineering Research Council by way of my supervisor's grants, the School of Graduate Studies, and the Department of Physics and Physical Oceanography.

Contents

List of Tables

List of Figures

List of symbols

^{12}C	Carbon-12, a carbon atom with 6 protons and 6 neutrons
^{13}C	Carbon-13, a carbon atom with 6 protons and 7 neutrons
$CaCO_3$	Calcium carbonate
cm^{-1}	Inverse centimeters, a unit of energy common in IR spectroscopy
f	Frequency
H	Mass-weighted Hessian matrix
I	Intensity
Im	Imaginary spectrum
k_B	Boltzmann constant
k_BT	Thermal energy
M	Atomic mass matrix
P_0	Power of incident IR radiation
q_n	Normalized spectrum
q_r	Reference spectrum
q_s	Sample spectrum
R	Eigenvector column matrix
R_s	IR light reflected by sample
Re	Real spectrum
U	Potential acting on atom
V	Mirror speed
α	Thermal diffusivity
β	Absorption coefficient
Δx	Mirror displacement
λ_i	Normal mode eigenvalues
μ_s	Sample thermal diffusion length
ν	Vibrational mode
ν_1	In-plane symmetric stretching mode
ν_2	Out-of-plane bending mode
ν_3	In-plane antisymmetric stretching mode
ν_4	In-plane bending mode
ω_i	Normal mode eigenfrequencies

List of abbreviations

ACC	Amorphous calcium carbonate
ATR	Attenuated total reflectance
DFT	Density functional theory
Far-IR	Far-range infrared
FIR	Far-range infrared
FFT	Fast Fourier transform
FTIR	Fourier transform infrared spectroscopy
FTIR-Op	Optical FTIR
FTIR-PAS	Photoacoustic FTIR
IR	Infrared
Mid-IR	Mid-range infrared
MIR	Mid-range infrared
NVT	Constant number of particles, volume and temperature
NPT	Constant number of particles, pressure and temperature
PAS	Photoacoustic spectroscopy
PXRD	Powder X-ray diffraction
THz-TDS	Terahertz time domain spectroscopy
UV	Ultra-violet
VDOS	Vibrational density of states
VS	Vibrational spectroscopic
XRD	X-Ray diffraction
ZPD	Zero path difference

Chapter 1

Brief introduction to vibrational spectroscopy and characterizing solid materials

The interdisciplinary field of materials science focuses on understanding how material structure and properties are related. Materials science research is often motivated by the drive to design or discover new materials that can improve application-specific performance, such as heat-resistance concrete in construction applications[10], flame-retardant coatings[13] or lightweight high-strength materials for aerospace and automotive applications[32]. As with many things, inspiration can often be found in nature, where biological organisms have refined remarkable and complex materials for eons.

The nature of the thesis relies on an in-depth understanding of the methods (infrared spectroscopy) and the materials (carbonate minerals). In this way, background information about carbonate materials is presented before introducing infrared spectroscopy so the reader can understand the interplay underpinning their relationship in the following chapters.

1.1 Overview

Atomic vibrations are a physical property that can be used to understand the nano-scale structure of a material. Crystal symmetry and composition dictate the allowed motions of atoms about their lattice sites. The motions of the atoms are influenced by differences in their environment at local and

long-range length scales. Structures of real materials incorporate defects such as atomic substitutions or holes, resulting in changes to the periodicity of the structure either on large scales like lattice distortion (compression, expansion) or locally (microstrain fluctuations). Changes in symmetry result in changes to the vibrations of the atoms. By looking at differences in these vibrations, researchers can gain information as to how that material formed, aged, or was used.[27,28,30,34,35,40]

Vibrational spectroscopic (VS) techniques offer a non-destructive way to examine the vibrational properties of a material. A material's vibrational modes are excited using photons of comparable energy (infrared, IR) or visible photons (Raman). In this way, vibrations of the material can be analyzed without inducing a change to the material structure, as these photons are non-ionizing in both cases. This can be important in contexts where the material is too precious to risk damage or alteration.[27,28,30,35,40] Before describing the details of vibrational spectroscopy, I will describe some of the kinds of materials questions that vibrational spectroscopy can help answer.

Nacre, known commonly as mother-of-pearl, is an organic/inorganic composite material heavily researched because of its remarkable mechanical properties. It is the inner shell layer of some bivalve creatures. Microscopically, it is made of stacked calcium carbonate platelets with thin layers of elastic biopolymer in between, much like macroscopic brick-and-mortar construction.[5,7,41] This combination of roughly 95% by weight brittle aragonite, the specific calcium carbonate polymorph, and 5% by weight soft organic polymer results in increased fracture toughness of roughly 3000 times that of the aragonite polymorph alone.[6,11,41] Nacre has been studied for decades at multiple length scales to understand how the complex hierarchical structure gives rise to its remarkable properties.

Past research focused on explaining the fracture resistance of nacre started with micro-scale experiments designed to explore the properties of laminates.[12,31] The discovery of the biopolymers gluing the tablets together came about due to scanning electron microscopy.[1,18,19] The polymer and protein matrices were determined to play a crucial role in aragonite crystal nucleation and growth.[14,36] Transmission electron microscopy showed that the aragonite tablets were not single-crystal but rather nanograin aragonite crystals with proteins in between the nanograins.[1,16] Understanding the enhanced toughness of nacre compared to aragonite requires analysis of the hierarchical structure across these length scales.[41] Thus, it is also important to understand the structure of the aragonite

nanograins themselves.

There are few vibrational mode studies done previously on nacre.[24,26,29,33,36,37] Most commonly, vibrational spectroscopic (VS) methods are used on powdered nacre samples for chemical identification of marine bivalve samples.[24,26,29,33] Powdering the nacre samples has the drawback of destroying the hierarchical structure, which is thought to be the source of the high fracture resistance.[41] Two studies by Verma *et al.*[36,37] focused explicitly on the structure of nacre using specialized types of vibrational spectroscopy. These investigations looked at the aragonite-protein interface and the water organization, respectively. These investigations advanced the understanding of how the complex structure of nacre responds to applied stresses.

Looking beyond nacre, others have examined the structure of geogenic and anthropogenic calcium carbonate samples using VS methods for archaeological contexts. Regev *et al.* developed grinding curves, an analysis method for VS data using calcite samples. They showed that specific trend lines could be linked to the geogenic or anthropogenic origins of the mineral.[30] Poduska and colleagues combined these grinding curves for calcite with simulations of local disorder to decouple experimental optical effects from sample-related crystallinity differences, further extending the usefulness of vibrational spectroscopic data analysis.[27] Toffolo and Boaretto used similar experimental techniques to show the unexpected presence of aragonite in archaeological samples as well as used these methods to track the nucleation of aragonite under controlled conditions to explain how the aragonite crystals could persist in such samples.[35] Xu *et al.* were the first to link the structural disorder signatures from powder X-ray diffraction, a ubiquitous structural characterization technique, in rock and plaster calcite samples with vibrational data.[40]

1.2 Vibrations in solids

In solid materials, the basis atoms are not rigidly pinned to the lattice site; instead, they can move about their equilibrium positions to varying degrees based on the symmetry of the crystal. This motion is random and driven by thermal energy fluctuations in real unperturbed systems. When the system is perturbed in some way, such as by absorbing a photon, the atoms will vibrate at natural frequencies intrinsic to the system. These are known as vibrational modes.

In its simplest form, the atomic vibrations of solid materials are complex, as they contain numbers of atoms on the order of Avogadro's number (10^{23}). While detailed analysis of this topic has been explained in many undergraduate and graduate textbooks, such as Marder[17] or Kittel[15], it is essential to highlight some important aspects of it here again.

It is possible to describe the fundamental behavior of the vibrational modes using a basic diatomic mass-spring model where the masses are atoms in the solid, and the chemical bonds are the springs.[15,17] The potential energy of a harmonic (Hooke-ian) oscillator is $\frac{1}{2}Kq^2$, where K is the force constant of the spring and q is the displacement of the oscillator. In our example, the spring constant, K, is determined by the chemical bonds and local environment, and the atoms are the oscillators with displacement q. To solve for the energy states of the system, one can use the time-independent Schrödinger equation,

$$-(\tfrac{\hbar}{2m})^2\tfrac{\partial^2\Psi}{\partial q^2}+(E-\tfrac{1}{2}Kq^2)\Psi=0 \tag{1.1}$$

which results in the energies of the vibrations, E_n,

$$E_n=(n+\tfrac{1}{2})h\nu, \tag{1.2}$$

where n is the vibrational quantum number, h is the Planck constant, and ν is the vibrational frequency of the diatomic system. For two different masses, A and B, ν is given by $\frac{1}{2}\sqrt{\frac{K}{\mu}}$, where μ is the reduced mass of the system, $\frac{(m_A m_B)}{(m_A+m_B)}$. Solids are significantly more complex than the preceding diatomic example. Nevertheless, the fundamentals of the vibrational energy states remain the same. The most important thing to note is the influence of mass on the energy states.

For this thesis work, we consider two main types of vibrational modes in solids: external and internal. External modes are the collective translations of multiple correlated atoms. Internal modes are vibrations of a moiety within the unit cell.

1.3 Vibrational spectroscopy

Information related to a material's structure can be gained by examining differences in the internal vibrational modes.[39,40] Vibrational spectroscopic techniques excite vibrational modes, or phonons, in the sample by irradiating the system with light and measuring the response. Spectroscopic methods are often used for chemical identification, as each compound will have a unique vibrational spectrum.[8,22]

Infrared spectroscopy, one of the most commonly used types of vibrational spectroscopy, excites the vibrational modes of a solid by perturbing it with infrared photons.[8,23] For a vibrational mode to be IR-active, it must cause a dipole moment in the molecular bond. In contrast, Raman Spectroscopy, another vibrational spectroscopy, explores the vibrational modes *via* Stokes or anti-Stokes (inelastic) scattering of visible photons.[17] For the inelastic scattering to occur, it must induce a polarizability change in the molecular bond. Infrared spectroscopy is the experimental method employed in this dissertation.

Photons are quantized amounts of electromagnetic energy. Vibrational modes in solids are the energy states of the molecular bonds and are also quantized. When a photon of equal energy to a vibrational state is incident on the molecule, it will be absorbed, causing the bonds to vibrate with the same frequency. Only photons of the correct energies can be absorbed to excite that material's specific vibrational modes. These vibrations are linked to the chemical composition and the lattice arrangement. In this way, it is possible to distinguish between different materials or even polymorphs based on the unique vibrations that are excited.

Modern infrared spectroscopy uses interferometry and the Fourier Transform to quickly measure sample absorption of the infrared radiation; this is known as Fourier Transform infrared spectroscopy (FTIR).[2,8,22] Even amongst FTIR instrumentation, multiple sub-types exist, each with advantages and disadvantages. While the data collection is similar, often using the same spectrometer, data processing and interpretation can significantly differ. A knowledge gap in the literature exists related to the nuances among specific methods.

The most basic and widely used method is transmission FTIR. The sample is mixed with an optical

dilutant material, pressed into a pellet, and placed directly in the beam path. The sample preparation required for transmission FTIR leads to potential problems of sample-to-sample reproducibility, not to mention the preparation time required.[3,4,27] Attenuated total-reflectance (ATR) FTIR is an alternative method that works by passing the IR beam into a high refractive index crystal.[2] The sample is then placed directly in contact with the ATR crystal, allowing IR light to be absorbed. The advantage here over transmission FTIR is less required sample preparation. Photoacoustic spectroscopy (PAS) is the method of choice for samples that are strongly absorbing solids or viscous liquids that cannot be ground or are insoluble in common solvents.[22,23] Rather than measuring the transmitted infrared radiation, PAS measures thermal waves induced in the sample after absorbing the infrared light. These techniques are well established in the literature for sample composition identification. Only recently have investigators begun to use these methods to assess structural differences in samples.[27,39,40]

In the past two decades, multiple research groups have used infrared spectroscopic methods to assess structural differences between calcium carbonate mineral samples.[27,30,40] Regev *et al.* developed an analysis based on the variation of internal vibrational peak height ratios in transmission FTIR measurements. Calcium carbonates with different formation methods followed unique trend lines ("grinding-curves"), enabling researchers to quickly distinguish between geogenic and anthropogenic calcite samples. Later work extended grinding-curves' usefulness by combining simulations with spectral analysis to decouple spectral peak narrowing due to particle size and peak broadening due to atomic disorder effects in FTIR measurements.[27] Xu *et al.* combined FTIR peak height measurements with powder X-ray diffraction measurements to link shifts in grinding-curves with atomic disorder of calcite samples in the way of lattice stain and microstrain fluctuations.[40] These previous investigations focused on analyzing the internal carbonate vibrations using infrared spectroscopy. There remains much to be understood about what structural information can be gained by exploring trends in the external vibrational modes.

1.4 Summary of thesis work

My research focuses on how the nuances of different infrared spectroscopic methods may be used to understand material structure better. For this reason, it was necessary to select a sample material

suitable for all measurements and calculations. Calcium carbonate was selected for the following reasons:

- relevant samples can be purchased, synthesized easily, or collected outdoors,
- calcium carbonate polymorphs have distinct, yet simple, spectra for the internal carbonate vibrations and are well studied in the literature,[27,28,30,34,35,39,40]
- minimal experimental or computational work has been done to date related to the external vibrations of these materials.

This dissertation involves the interpretation of data collected experimentally and generated computationally. It consists of two experimental projects as well as a related computational component.

1.4.1 Chapter 3: Far infrared external modes

Infrared spectroscopic data of external vibrational modes for calcite samples highlighted data interpretation challenges related to the overlapping broad spectral peaks and is the subject of Chapter 3[3]. Asynchronous data collection of internal and external modes was done for the samples. The same samples were measured without being disturbed. Only a swap to the apparatus optics (beamsplitter and detector) was necessary. Observed changes in the vibrational modes were then correlated with powder X-ray diffraction (PXRD) data to determine the effects of structural differences on all modes, internal and external. Nomenclature in this work refers to internal carbonate modes as "local" modes and external modes as "lattice".

This work is published as S. Campbell and K. M. Poduska. Incorporating far-infrared data into carbonate mineral analyses. Minerals, 10(7):628, 2020. doi: 10.3390/min10070628.

1.4.2 Chapter 4: Photoacoustic enhancement

An alternative FTIR detection method, photoacoustic FTIR (PAS), enhances typically weak spectral features compared to transmission FTIR.[4] The use of this technique on calcium carbonates and an investigation into the enhancements observed is the subject of Chapter 4. Due to limitations related to

internal optics, this method was limited to the Mid-IR range. This makes the technique non-optimal when focused on understanding the external modes, but it is not without a place in developing a broader approach to structural characterization. Previous work by our group and others using PAS has highlighted significant enhancements to the peak intensities of the weaker modes in the Mid-IR region.[20,21,25,38] As this energy range is one of the anchor points in this study, understanding whether this enhancement is intrinsic to the method as well as the mechanism for this signal increase is a high priority.

This work is published as S. Campbell, M. Dusseault, B. Xu, K. H. Michaelian, and K. M. Poduska. Photoacoustic detection of weak absorption bands in infrared spectra of calcite. Applied Spectroscopy, 75(7):795–801, 2021. doi: 10.1177/00037028211009212. PMID: 33783238.

1.4.3 Chapter 5: Simulations of aragonite

The computational component, which is the focus of Chapter 5, uses molecular dynamics simulation methods and, as such, is written in a self-contained fashion while also being discussed in Chapter 6.

Computational modeling of the vibrational modes of calcite and aragonite is compelling. It enables the investigator to make targeted changes to the sample that would be impractical or impossible to control with synthesized or natural samples. Modeling the internal carbonate vibrations of these materials has successfully been done using Density Functional Theory (DFT) methods. DFT simulations previously used to explore the internal vibrational modes of calcium carbonate are not computationally feasible to explore the external modes[9]. The external modes are also quite dispersive. Molecular dynamics simulations of calcium carbonate using mature and available software should allow for generating a vibrational density of states (VDOS), a similar type of data to that collected experimentally using vibrational spectroscopic methods. Initial investigations into the use of molecular dynamics simulations to examine the vibrational density of states (VDOS) of aragonite, a calcium carbonate polymorph, is the subject of Chapter 5. This work explores the viability of currently available force-field parameters of calcium carbonate using the molecular dynamics package GROMACS to simulate the crystal vibrations. Our ultimate goal is to use these simulations to understand how the vibrational modes change with different types of structural disorder.

This chapter is written in a manuscript style but is not yet submitted for publication.

1.5 Statement of Contribution

The Chapters of this thesis are written in a manuscript-style format. Chapters 3 and 4 are reproduced verbatim from co-authored papers published in Minerals and Applied Spectroscopy, respectively, and reprinted with appropriate permissions. The contributions of the co-authors mentioned above are described in detail at the beginning of each chapter. For the remaining chapters, I performed all the data generation (computational), collection (experimental), and analysis and wrote them. My supervisor, Dr. Kristin M. Poduska, and my supervisory committee, Dr. Alison Malcolm and Dr. James LeBlanc, provided me with comments and feedback.

Figures 2.5 and 2.3 are used under the terms of their respective licenses. Figure 2.1 is reproduced and modified with permission from Elsevier. All others are my own.

Bibliography

[1] F. Barthelat, C.-M. Li, C. Comi, and H. D. Espinosa. Mechanical properties of nacre constituents and their impact on mechanical performance. Journal of Materials Research, 21(8):1977–1986, 2006.

[2] M.-M. Blum and H. John. Historical perspective and modern applications of attenuated total reflectance–Fourier transform infrared spectroscopy (ATR-FTIR). Drug Testing and Analysis, 4 (3-4):298–302, 2012.

[3] S. Campbell and K. M. Poduska. Incorporating far-infrared data into carbonate mineral analyses. Minerals, 10(7):628, 2020. doi: 10.3390/min10070628.

[4] S. Campbell, M. Dusseault, B. Xu, K. H. Michaelian, and K. M. Poduska. Photoacoustic detection of weak absorption bands in infrared spectra of calcite. Applied Spectroscopy, 75(7):795–801, 2021. doi: 10.1177/00037028211009212. PMID: 33783238.

[5] E. R. Cruz-Chú, S. Xiao, S. P. Patil, K. Gkagkas, and F. Gräter. Organic filling mitigates flaw-sensitivity of nanoscale aragonite. ACS Biomaterials Science & Engineering, 3(3):260–268, 2017.

[6] J. D. Currey. Mechanical properties of mother of pearl in tension. Proceedings of the Royal Society of London. Series B. Biological Sciences, 196(1125):443–463, 1977.

[7] L. J. Gibson. Cellular Solids: Structure and Properties. Cambridge solid state science series. Cambridge University Press, Cambridge, second edition. edition, 1997. ISBN 9781139878326.

[8] P. R. Griffiths and J. A. de Haseth. Fourier transform infrared spectrometry, volume 83 of Chemical Analysis. Wiley, 1st edition, 1986.

[9] R. Gueta, A. Natan, L. Addadi, S. Weiner, K. Refson, and L. Kronik. Local atomic order and infrared spectra of biogenic calcite. Angewandte Chemie International Edition, 46(1-2):291–294, Jan. 2007. ISSN 1521-3773. doi: 10.1002/anie.200603327.

[10] M. Hussin, M. Bhutta, M. Azreen, P. Ramadhansyah, and J. Mirza. Performance of blended ash geopolymer concrete at elevated temperatures. Materials and Structures, 48(3):709–720, 2015.

[11] A. Jackson, J. F. Vincent, and R. Turner. The mechanical design of nacre. Proceedings of the Royal Society of London. Series B. Biological Sciences, 234(1277):415–440, 1988.

[12] A. Jackson, J. Vincent, and R. Turner. A physical model of nacre. Composites Science and Technology, 36(3):255–266, 1989.

[13] B. Jin, H. Wang, H. Xu, H. Wu, W. Wu, Z. Yuan, Z. Huang, Y. Wang, and J. Wu. Bio-inspired nacre-like composites with excellent mechanical properties, gas-barrier function and fire-retardant performances based on self-assembly between hyperbranched poly(amido amine)s and montmorillonite. RSC advances, 13(6):3661–3668, 2023.

[14] K. S. Katti, D. R. Katti, and B. Mohanty. Biomimetic lessons learnt from nacre. Biomimetics Learning from Nature, page 193, 2010.

[15] C. Kittel et al. Introduction to Solid State Physics, volume 8. Wiley New York, 1976.

[16] X. Li, W.-C. Chang, Y. J. Chao, R. Wang, and M. Chang. Nanoscale structural and mechanical characterization of a natural nanocomposite material: the shell of red abalone. Nano Letters, 4 (4):613–617, 2004.

[17] M. P. Marder. Condensed Matter Physics. John Wiley and Sons, 2 edition, 2010.

[18] M. A. Meyers, P.-Y. Chen, A. Y.-M. Lin, and Y. Seki. Biological materials: structure and mechanical properties. Progress in Materials Science, 53(1):1–206, 2008.

[19] M. A. Meyers, A. Y.-M. Lin, P.-Y. Chen, and J. Muyco. Mechanical strength of abalone nacre: role of the soft organic layer. Journal of the Mechanical Behavior of Biomedical Materials, 1(1): 76–85, 2008.

[20] K. Michaelian, Q. Wen, B. Billinghurst, J. Shaw, and V. Lastovka. Far-and mid-infrared photoacoustic spectra of tetracene, pentacene, perylene and pyrene. Vibrational Spectroscopy, 58: 50–56, 2012.

[21] K. Michaelian, S. Oladepo, J. Shaw, X. Liu, D. Bégué, and I. Baraille. Raman and photoacoustic infrared spectra of fluorene derivatives: Experiment and calculations. Vibrational Spectroscopy, 74:33–46, 2014.

[22] K. H. Michaelian. Photoacoustic Infrared Spectroscopy. Wiley-Interscience, Hoboken, N.J., 2003. ISBN 0471134775. Errata inserte.

[23] K. H. Michaelian. Photoacoustic IR Spectroscopy: Instrumentation, Applications and Data Analysis. Wiley-VCH, 2010.

[24] K. Narasimhulu and J. L. Rao. EPR and IR spectral studies of the sea water mussel Mytilus conradinus shells. Spectrochimica Acta Part A: Molecular and Biomolecular Spectroscopy, 56 (7):1345–1353, 2000.

[25] M. Natale and L. N. Lewis. Application of PAS for the investigation of overtones and combinations in the near IR. Applied Spectroscopy, 36(4):410–413, 1982.

[26] M. Ni and B. D. Ratner. Nacre surface transformation to hydroxyapatite in a phosphate buffer solution. Biomaterials, 24(23):4323–4331, 2003.

[27] K. M. Poduska, L. Regev, E. Boaretto, L. Addadi, S. Weiner, L. Kronik, and S. Curtarolo. Decoupling local disorder and optical effects in infrared spectra: Differentiating between calcites with different origins. Advanced Materials, 23(4):550–554, 2011. ISSN 1521-4095. doi: 10.1002/adma.201003890.

[28] K. M. Poduska, L. Regev, F. Berna, E. Mintz, I. Milevski, H. Khalaily, S. Weiner, and E. Boaretto. Plaster characterization at the PPNB site of Yiftahel (Israel) including the use of ^{14}C: implications for plaster production, preservation, and dating. Radiocarbon, 54(3-4):887–896, 2012.

[29] C. L. Raju, K. Narasimhulu, N. Gopal, J. Rao, and B. Reddy. Electron paramagnetic resonance, optical and infrared spectral studies on the marine mussel Arca burnesi shells. Journal of Molecular Structure, 608(2-3):201–211, 2002.

[30] L. Regev, K. M. Poduska, L. Addadi, S. Weiner, and E. Boaretto. Distinguishing between calcites formed by different mechanisms using infrared spectrometry: archaeological applications. Journal of Archaeological Science, 37(12):3022–3029, 2010.

[31] M. Sarikaya, K. Gunnison, M. Yasrebi, and I. Aksay. Mechanical property-microstructural relationships in abalone shell. MRS Online Proceedings Library, 174:109–116, 1989.

[32] G. Shi, Z. Wu, and H. Wang. A novel metal-ceramic composite combining the structures of nacre and nanofiber reinforced foam. Journal of Materials Science & Technology, 157:189–199, 2023.

[33] T. Tan, D. Wong, and P. Lee. Iridescence of a shell of mollusk Haliotis Glabra. Optics Express, 12(20):4847–4854, 2004.

[34] M. B. Toffolo. The significance of aragonite in the interpretation of the microscopic archaeological record. Geoarchaeology, 36(1):149–169, 2021. doi: https://doi.org/10.1002/gea.21816.

[35] M. B. Toffolo and E. Boaretto. Nucleation of aragonite upon carbonation of calcium oxide and calcium hydroxide at ambient temperatures and pressures: a new indicator of fire-related human activities. Journal of Archaeological Science, 49:237–248, 2014.

[36] D. Verma, K. Katti, and D. Katti. Photoacoustic FTIR spectroscopic study of undisturbed nacre from red abalone. Spectrochimica Acta Part A: Molecular and Biomolecular Spectroscopy, 64 (4):1051–1057, 2006.

[37] D. Verma, K. Katti, and D. Katti. Nature of water in nacre: a 2D fourier transform infrared spectroscopic study. Spectrochimica Acta Part A: Molecular and Biomolecular Spectroscopy, 67 (3-4):784–788, 2007.

[38] B. Xu. Assessing different types of disorder in carbonate minerals with vibrational spectroscopy. PhD thesis, Memorial University of Newfoundland, St. John's, Newfoundland, October 2015.

[39] B. Xu and K. M. Poduska. Linking crystal structure with temperature-sensitive vibrational modes in calcium carbonate minerals. Physical Chemistry Chemical Physics, 16(33):17634–17639, 2014.

[40] B. Xu, M. B. Toffolo, L. Regev, E. Boaretto, and K. M. Poduska. Structural differences in archaeologically relevant calcite. Analytical Methods, 7(21):9304–9309, 2015.

[41] N. Zhang, S. Yang, L. Xiong, Y. Hong, and Y. Chen. Nanoscale toughening mechanism of nacre tablet. Journal of the Mechanical Behavior of Biomedical Materials, 53:200–209, 2016.

Chapter 2

Experimental details

This dissertation focuses on data interpretation of different experimental infrared (IR) spectroscopy techniques. To discuss these topics adequately, one must understand the instrumentation and sample preparation differences for the different flavors of IR spectroscopy: transmission, attenuated total reflectance (ATR), and photoacoustic (PAS). While these types of IR spectroscopy are all designed to measure the vibrational modes of the sample, how this happens in practice is very different. Additionally, I compare these with the instrumentation and sample preparation for powder X-ray diffraction (PXRD), a complementary material characterization technique.

Using a well-understood sample material is important to address the measurement-related effects on the collected data. I use calcium carbonate as the case study material for this dissertation in part due to the expertise of my research group. Further, calcium carbonates are topical in various fields, such as geoscience, astronomy, archaeology, construction materials, and biomineralization.[8,19,21,31,35,36,44] Investigations in these research areas commonly make use of PXRD to identify materials by their crystal structures. They also often use vibrational spectroscopic methods due to their ability to identify the presence of calcium carbonate, either uniquely or in conjunction with chemical species related to its formation or degradation.[8,10,19,21,32,33,40–43]

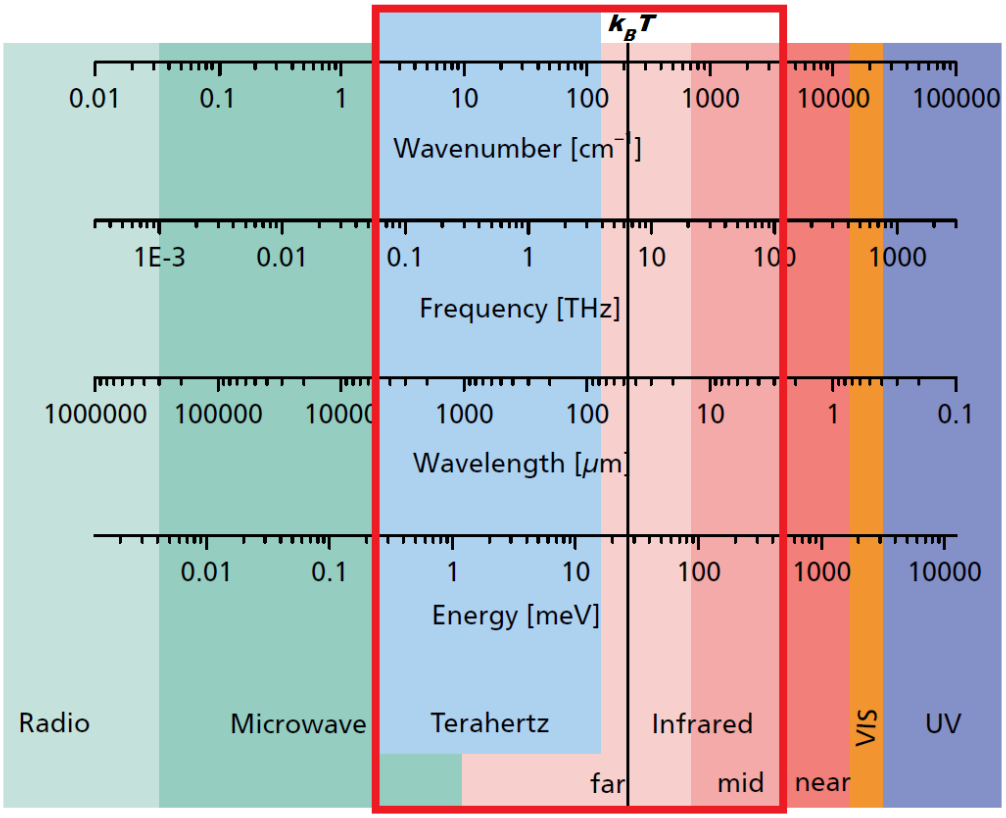

Figure 2.1 The electromagnetic spectrum, from the radio to UV regions, in various energy units. Energies relevant to this thesis are boxed in red. k_BT indicated for reference. Figure modified from El Haddad *et al.*[16] Used with permission.

2.1 Infrared spectroscopic methods

Infrared spectroscopy offers researchers a non-destructive way to examine the material structure, even in cases where the material is poorly crystalline or amorphous. The energies of infrared light and the vibrational modes of a solid are on the same order of magnitude. Thus, it is possible to excite these vibrational modes by irradiating the system with infrared light. This way, it is possible to quickly distinguish between different materials or polymorphs based on the unique combination of vibrational modes. These spectra are often referred to as fingerprint spectra since they are used to identify a material or mixture of materials.[1–5,15,25,26,28,29] The vibrations are linked to the chemical composition and the lattice arrangement. However, it is impossible to use infrared spectroscopy alone to determine crystal structure or identify specific structural disorder types.[42]

The most commonly used energy regime for infrared spectroscopy is the Mid-range infrared (Mid-IR) covering 400-4000 cm^{-1} (about 2.5-25 μm). The internal carbonate vibrational modes of calcium carbonate fall in this range. Much less common in the literature is the Far infrared region (80-650 cm^{-1}, equivalent to 15.4-125 μm), which hosts the external vibrational modes of calcium carbonate minerals. Figure 2.1 highlights the Mid-IR and Far-IR regions of the electromagnetic spectrum and contrasts them with other typical spectroscopic regimes. External vibrational modes are lower in energy than their internal mode counterparts. For calcium carbonates, these modes are related to the relative motion of the calcium and carbonate units.

2.1.1 Fourier Transform Infrared Spectroscopy

Fourier transform infrared (FTIR) spectroscopy, a type of infrared spectroscopy, has effectively identified crystallinity-related differences in calcite.[32,33,36,40,41] Differences in the Mid-IR vibrational signatures of calcite with different origins were linked to structural differences identified using Powder X-Ray diffraction (PXRD). The spectra of more crystalline samples showed sharper, narrowed peaks, while peak broadening and reduced intensities indicated samples with more disorder.[32,36,40] Changes in the local atomic environment affect the Mid-IR vibrations by shifting the energies of peaks, peak broadening, and relative peak intensity differences.

Two sub-types of FTIR spectroscopy, attenuated total reflectance and photoacoustic, are the experimental focus of this thesis work. Both methods make use of the same primary spectrometer with a different attachment. What follows is a summary of the basic operating principles of the technique, with more specific details about each to follow.

The FTIR spectrometer

FTIR was developed to reduce the data acquisition times of the original dispersive IR spectrometers.[7] Figure 2.2 shows a schematic diagram of an FTIR spectrometer that uses a Michelson interferometer. The infrared beam is created by a broadband thermal source (globar) (Figure 2.2A) as it emits light approximately like a black body (Planck radiator) over the wavenumber region of interest (Mid-IR 4000-400 cm^{-1}, Far-IR 400-80 cm^{-1}). The infrared beam enters the Michelson interferometer, which

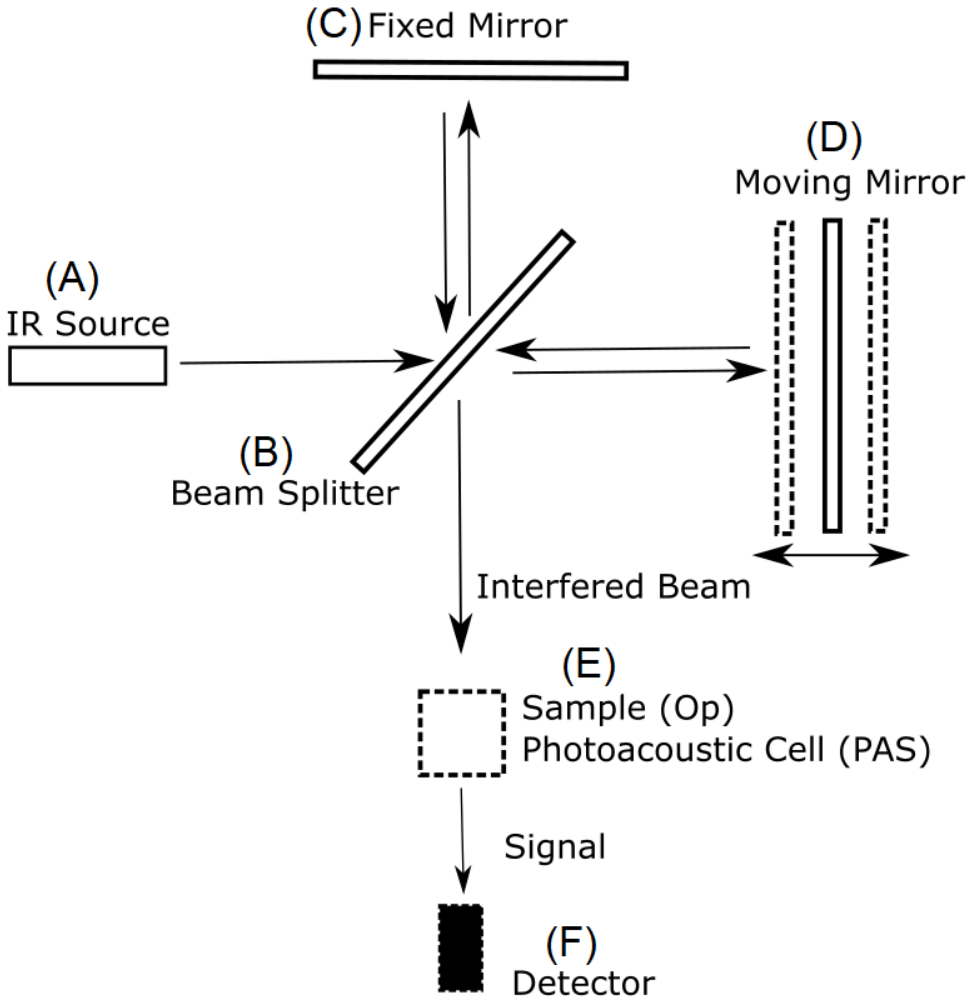

Figure 2.2 A schematic picture of the FTIR spectrometer highlighting the use of a Michelson interferometer. The infrared source (A) generates the initial beam. The beam splitter (B) divides the initial IR beam into two beams with half the source intensity. The stationary mirror (C) and the moving mirror (D) are used to create a path difference for the two beams, resulting in interference. The interfered IR beam is incident on the sample (E), with the final interferogram being recorded at the detector (F, FTIR-Op, and ATR) or in the PAS cell (E, FTIR-PAS).

consists of a beam splitter, a fixed mirror, and a moving mirror (Figure 2.2B, C, and D, respectively). The beam is split into two beams of equal intensity *via* the beam splitter. The beams are reflected by both the fixed and moving mirrors. The moving mirror oscillates at a rate referred to as the mirror speed that is set *via* the control software.

Moving one mirror creates a path difference, which causes the beams to interfere. As a result, each wavelength generated from the broadband source is modulated at a different frequency. This way, the entire wavelength range is recorded simultaneously as an interferogram: light intensity, I as a function of mirror displacement, Δx. The Fourier transform is then used to convert the interferogram (I vs. Δx) into a spectrum (I vs. wavenumber, λ). In practice, the data is processed *via* the Fast Fourier Transform (FFT) algorithm. The specific value of the mirror speed determines the modulation frequency at the wavenumber of a helium-neon laser (15800 cm^{-1}) and is sometimes reported synonymously as this modulation frequency (OPUS software). Every subsequent wavenumber of the IR beam is modulated at a proportionally lower frequency.

Data collection for transmission (absorption) FTIR methods is often straightforward in the Mid-IR range (4000-400 cm^{-1}). The preparation involves grinding solid samples, diluting them with a non-Mid-IR active material (often potassium bromide, KBr), and pressing them into a sample pellet. The pellet is placed in the beam path where infrared radiation is absorbed by the atoms at energies corresponding to the specific mode energies.[32,41] With minor changes to the optics of many commercially available spectrometers (swapping the beamsplitter and detector), it is possible to collect vibrational data for lower energy external vibrations in the Far-IR region (400-80 cm^{-1}). Far-IR data collection also requires alternative optical dilutants, as KBr strongly absorbs these energies. ATR-FTIR was used for the experimental investigation into calcium carbonate external modes as it avoids this sample preparation.

Attenuated total reflectance infrared spectroscopy

Attenuated total reflectance (ATR) is a phenomenon that occurs due to a specific ratio of indices of refraction between two materials.[7] Figure 2.3 shows how this is applied in IR spectroscopy. The modulated IR beam is passed into a specialized apparatus that contains an ATR crystal, often a diamond,

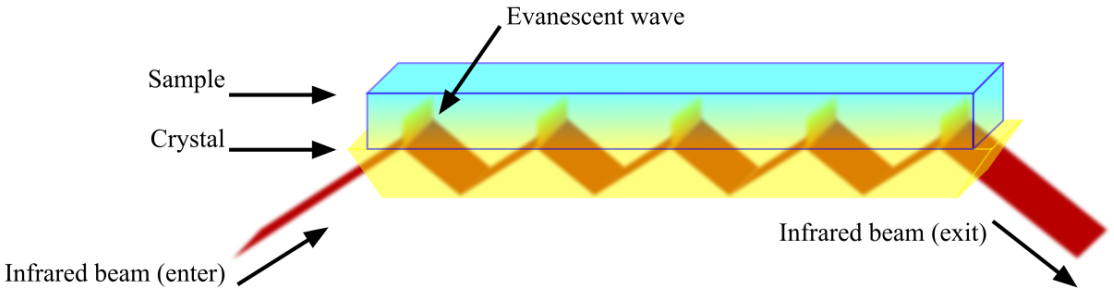

Figure 2.3 Schematic diagram of the attenuated total reflectance leveraged in ATR-FTIR. The components of the evanescent wave absorbed by the sample are absent when the spectrometer records the interferogram. Image created by Fulvio314, used under CC BY-SA 3.0 `https://creativecommons.org/licenses/by-sa/3.0`, via Wikimedia Commons

where it undergoes total internal reflectance. The sample is in direct contact with the ATR crystal. At this interface, an evanescent wave penetrates the sample normal to the crystal. As with other IR spectroscopic measurements, specific beam energies that correspond to the vibrational modes of the sample are absorbed. The remaining beam passes out of the ATR attachment and is measured by the spectrometer, again as an interferogram. A Fourier transform results in the sample spectrum.

Photoacoustic infrared spectroscopy

As an alternative to transmission or ATR measurements, commercially available spectrometer attachments can be used to leverage the photoacoustic effect.[6] Transmission and ATR sample spectra are produced by taking the ratio of the unadulterated IR beam with the sample signal. In cases where samples are strongly absorbing, this results in a zero-division and appears as a saturation of the detectors. Photoacoustic FTIR spectroscopy (FTIR-PAS) relies on applying the photoacoustic effect. Some energy is absorbed when modulated infrared light is incident on a sample. This results in heating within the sample and producing thermal waves within the bulk. The thermal waves cause a cyclic expansion and contraction of the material. Photoacoustic detectors for FTIR spectrometers are specifically designed to measure these thermal waves. The spectrum is produced by dividing the sample signal intensity by a strongly absorbing reference material signal, usually carbon-black, eliminating the possibility of a zero-division. FTIR-PAS does not require sample preparation, which is useful for samples that are challenging to grind and press into a pellet, as is required for transmission measurements. Much like ATR-FTIR previously discussed, photoacoustic FTIR is non-destructive, able to characterize small

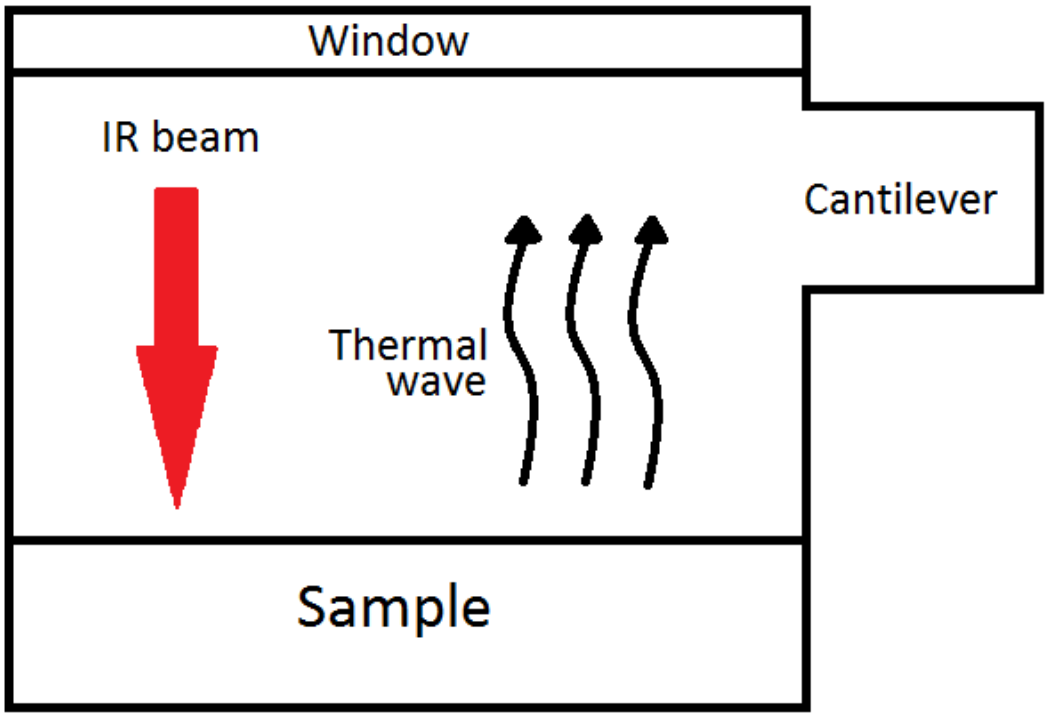

Figure 2.4 Schematic diagram of the photoacoustic cell. The interfered IR beam (red) is directed into the cell from the IR spectrometer and incident on the sample. The carrier gas transfers the thermal waves (black) created in the sample to the cantilever.

amounts of sample, and can also be used to examine poorly crystalline or amorphous samples.

Figure 2.4 shows a schematic diagram of a photoacoustic cell. Modulated IR light is directed into the photoacoustic cell and onto the sample. Part of the radiation is absorbed by the sample, causing temperature oscillations. For greater details on this process, the reader is referred to Photoacoustic IR Spectroscopy: Instrumentation, Applications and Data Analysis by Kirk H. Michaelian.[27] The following is a summary based on those details. The temperature oscillations are proportional to $P_0(1-R_s)\beta e^{-\beta x}$, where P_0 is the power of the incident IR light, R_s is the amount reflected by the sample, β is the samples' absorption coefficient, and x is the depth in the sample at which the temperature oscillations are induced. The thermal diffusion length, $\mu_s = \sqrt{\frac{\alpha}{\pi f}}$, is defined as the distance at which the thermal wave amplitude decays to $\frac{1}{e}$ of its original magnitude, where α is the thermal diffusivity of the sample and f is the modulation frequency of the IR light. The sample is in contact with the atmosphere inside the detector, known as the carrier gas. The cyclic expansion of the sample produces a pressure wave in the carrier gas, which is detected acoustically *via* the cantilever. The Fourier transform of the acoustic

wave is the photoacoustic signal of the sample.

Data collected in the ambient atmosphere will have peaks related to water vapor and carbon dioxide as they are abundant IR-absorbing molecules. The PAS cell can be purged using another dry gas, such as nitrogen or helium, to reduce these unwanted signatures. These diatomic molecules do not have dipole moments and, thus, will not absorb the infrared radiation. Aside from eliminating unwanted ambient signals, this has the added benefit of improving the signal-to-noise ratio as the lighter gases carry the photoacoustic signal more efficiently.[25] Often, nitrogen is used as it is less expensive and more readily available.

At times, it is desirable to have a photoacoustic (PA) sample spectrum that resembles the same samples' transmission (absorption) spectrum. Certain features may be saturated in a photoacoustic experiment depending on sample properties. Spectral linearization, first developed by Burggraf and Leyden, is a calculation that uses the photoacoustic signal amplitude and phase.[9] The Fast Fourier Transform of a PA interferogram yields a Real, Re, and Imaginary, Im, spectrum. The typical PA spectrum reported is the power spectrum, $q_s = (Re_s^2 + Im_s^2)^{\frac{1}{2}}$. Then, a normalized PA spectrum is the ratio of a sample spectrum and a reference spectrum, $q_n = \frac{q_s}{q_r}$. A linearized spectrum is instead calculated as $q_l = \frac{q_s^2}{(Re_s Im_r - Im_s Re_r)}$, using the Real and Imaginary components of both the sample and reference spectra. This procedure greatly reduces saturation effects observed in PA spectra.[12] For greater details and application situations, the interested reader is again referred to the superb text, Photoacoustic IR Spectroscopy: Instrumentation, Applications and Data Analysis by Kirk H. Michaelian.[27]

All IR data presented in this thesis were collected using Bruker FTIR spectrometers. Transmission, ATR, and PAS measurements were done at Memorial University using a Bruker Vertex 70V spectrometer equipped with a Platinum Diamond ATR attachment (ATR) or a cantilever-based Gasera PA301 photoacoustic cell (PAS). Additional PAS measurements using a Bruker IFS 66v/S with an MTEC 300 microphone-based cell were done at the Canadian Light Source (CLS) mid-infrared beamline. Further details for ATR measurements are given in Section 3.2 of Chapter 3, whereas details related to PAS measurements are given in Section 4.2 of Chapter 4.

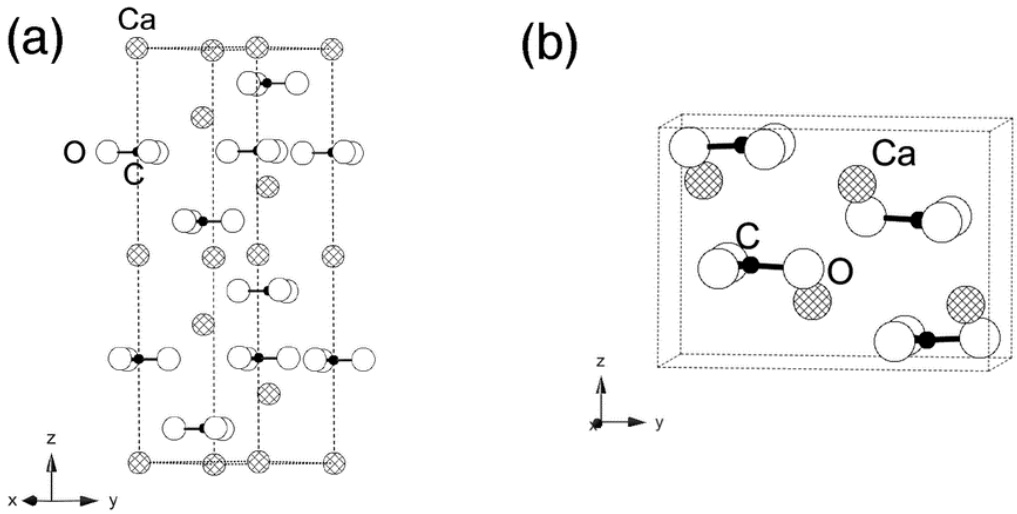

Figure 2.5 Schematic of the crystal structures of (a) calcite and (b) aragonite. Image modified from Xu and Poduska (2014)[40]. Used under the terms of the Creative Commons Attribution-NonCommercial 3.0 License (CC BY-NC 3.0)

2.2 Vibrational modes in $CaCO_3$ polymorphs

The calcite crystal structure, shown in Figure 2.5(a), can be described with a hexagonal unit cell (space group $P\bar{3}1m$) that contains four formula units, arranged in an alternating layered pattern (in the x-y plane) of calcium ions and carbonate (CO_3^{-2}) units.[34] The crystal structure of aragonite (Figure 2.5b) is orthorhombic. Rather than the stacked layered structure of calcite, aragonite is made of four formula units in a staggered arrangement.

The vibrational modes for calcite are derived from an analysis of its primitive rhombohedral unit cell, which contains ten atoms (two formula units). Many different theoretical and experimental studies have verified the energies and symmetries of calcite's 27 possible optical vibrational modes[8,20,22,37]. Four possible vibrations within a single carbonate moiety exist, but only three have a dipole moment that makes them IR-active. In the literature, these three modes have the following labels: ν_2 designates out-of-plane bending, ν_3 is asymmetric stretching, and ν_4 is in-plane bending or wagging.[37,43]

The external vibrational modes are more challenging to describe because they involve relative translations and librations of the calcium and carbonate ions. Due to the comparable energies of two

pairs of two vibrations, I opt not to use the spectroscopic designations, ν_X. The spectral peaks associated with these external modes are more often detected and reported as three bands: 300 cm^{-1} (comprised of ν_6 and ν_8, which we designate in this work as B1), 220 cm^{-1} (corresponding to ν_9, which we call B2), and 100 cm^{-1} (comprised of ν_7 and ν_{10}, which we refer to as B3).[8,10,21,37] Experimentally determined vibrational mode frequencies for calcite measured by Hellwege *et al.* are summarized in Table 2.1.[18] Similarly, vibrational mode frequencies measured by Couture are summarized in Table 2.2.[14]

Table 2.1 Experimentally reported values of IR vibrational mode frequencies of calcite. Spectroscopic designations are taken from Farmer[37], energy values (cm^{-1}) taken from Hellwege *et al.*[18]

Designation	ν_{exp} [cm^{-1}]	ν_{exp} [THz]	Description
ν_7	92	2.8	external mode
ν_{10}	102	3.1	external mode
ν_9	223	6.7	external mode
ν_8	297	8.9	external mode
ν_6	303	9.1	external mode
ν_4	712	21.3	internal mode (wag)
ν_2	872	26.1	internal mode (bend)
ν_3	1407	42.2	internal mode (stretch)
$\nu_1 + \nu_4$	1798	53.9	internal mode (combination)

Table 2.2 Experimentally reported values of IR vibrational mode frequencies of aragonite. Spectroscopic designations are taken from Farmer[37], energy values (cm^{-1}) taken from Couture[14].

Designation	ν_{exp} [cm^{-1}]	ν_{exp} [THz]	Description
–	113	3.4	external mode
–	146	4.4	external mode
–	155	4.6	external mode
–	183	5.5	external mode
–	193	5.8	external mode
–	208	6.2	external mode
–	217	6.5	external mode
–	222	6.7	external mode
–	250	7.5	external mode
–	263	7.9	external mode
–	276	8.3	external mode
–	287	8.6	external mode
ν_4	699,712	21.0, 21.3	internal mode (wag)
ν_2	870,875	26.1, 26.2	internal mode (bend)
ν_1	1085	32.5	internal mode (stretch)
ν_3	1490	44.7	internal mode (stretch)

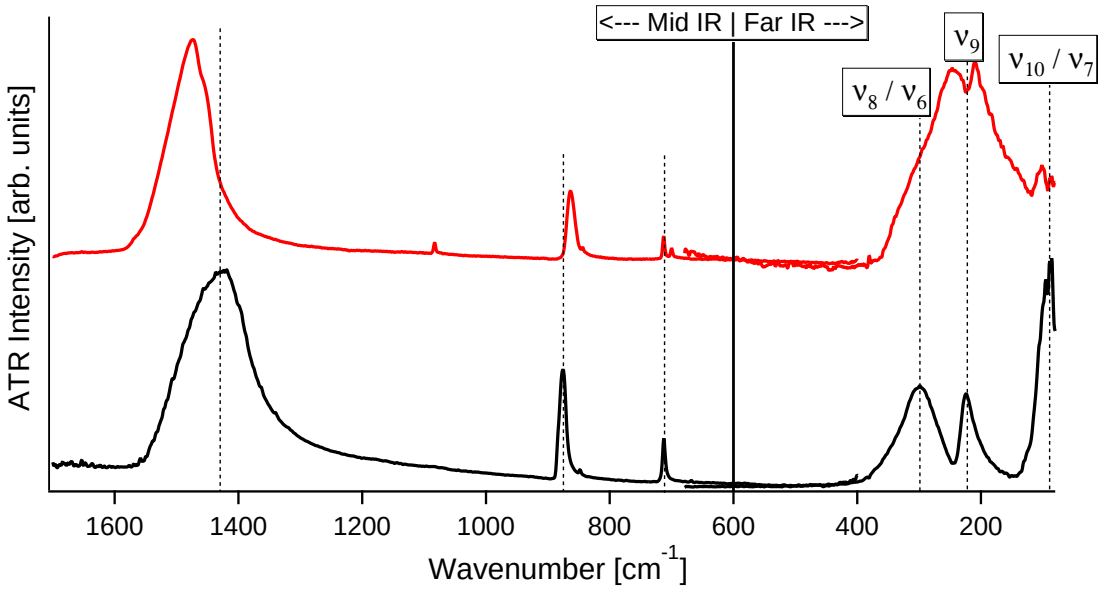

Figure 2.6 Example infrared spectrum of calcium carbonate polymorph calcite (black) and a calcite-aragonite mixture (red). Vibrational mode centers for calcite are indicated with dashed lines. The structural arrangement difference between the two polymorphs is apparent based on the changes to the spectra.

Figure 2.6 shows characteristic ATR-FTIR data for calcite (black curve) and a calcite-aragonite mixture (red curve). The division between the Mid-IR and Far-IR regions is indicated at 600 cm^{-1}, but the specific wavenumber value is arbitrary. The division is meant to separate the internal and external modes visually.[37] Mid-IR and Far-IR spectra are collected using the same instrumentation following a change to the optics. Each region (MIR, FIR) is normalized to the most intense feature to facilitate relative peak intensity comparisons within, but not between, the regions. No meaning should be drawn from relative intensities between regions nor differences in the overlap area (roughly 680 cm^{-1} to 400 cm^{-1}). Overlap region differences are due to optical effects in the instrumentation and not sample differences.

Changes in the material structure are inferred by examining the spectrum for differences in peak positions, shapes, widths, and absolute and relative intensities.[13,17,32,39] Peak positions correspond to the energy of the vibrational mode, which depends on the atoms involved and their configuration in both the local environment (i.e., a unit cell) and over longer range ordering related to the overall sample crystallinity. These FTIR peak positions can be calculated using density functional theory (DFT)[13,17]. Changes in peak widths have been linked to atomic ordering and optical absorption effects[32]. Relative peak intensities are also affected by atomic ordering in calcium carbonate materials

with varying degrees of crystallinity[32,33,35,41,42].

2.3 Powder X-ray diffraction

Powder X-ray diffraction (PXRD) data were collected for a subset of samples outlined in Chapter 3 to correlate observed vibrational mode differences in the FTIR data with crystal structure ordering. PXRD data collection was only possible for samples with adequate amounts of material, as PXRD requires more than ATR-FTIR. Further details about the measurement specifics are described in Section 3.2 of Chapter 3.

PXRD is used to determine lattice plane distances and lattice constants by having monochromatic X-rays interfere constructively off of the crystal planes. Constructive interference of the X-ray light occurs according to Bragg's Law,

$$n\lambda = 2d\sin\theta, \tag{2.1}$$

where n is an integer, λ is the wavelength of the X-rays, d is the crystal plane spacing, and θ is the angle between the incident light and the crystal plane. Each crystal plane has a specific angle, θ, to cause constructive interference. Using a powdered sample means that all possible diffractions will be recorded by scanning through a range of angles, as the random orientation of the powder results in all possible crystal orientations. Plane spacing and lattice constants can be calculated based on the scattering angles. Additionally, Williamson-Hall analysis can extract the samples' crystalline domain sizes and microstrain fluctuations from the PXRD data.[38,41] The relationship given by equation 2.2 relates Bragg peak properties to the crystalline domain size and microstrain fluctuations as follows:

$$\mathrm{FWHM}\cos\theta = \frac{K\lambda}{r} + 4\sigma\sin\theta\ , \tag{2.2}$$

where FWHM is the full-width at half maximum for a given diffraction peak, θ is the Bragg diffraction angle of the same peak, r is the crystalline domain size, σ is the microstrain fluctuation, λ is the incident X-ray wavelength and K is a dimensionless shape factor.

It is crucial to note that PXRD requires crystalline samples to be effective. Poorly crystalline samples, such as those often found in heat-formed calcium carbonates, produce broad Bragg peaks unsuitable for lattice refinements or Williamson-Hall analysis.

2.4 Project methods in subsequent Chapters

2.4.1 Chapter 3: Far infrared external modes

This paper is the first to explicitly connect the Far-IR and Mid-IR spectra for calcite and aragonite. FTIR-ATR spectroscopy is well suited for external vibrational mode measurements of calcium carbonate samples and the primary experimental method of Chapter 3.[10]. FTIR-ATR eliminates the need for an IR transparent matrix material for standard transmission FTIR methods. Similarly, optical windows in the PAS-FTIR cell block Far-IR wavelengths, making that method unsuitable. Further, the use of ATR-FTIR allows for additional consistency across measurements. Changing the apparatus optics (beamsplitter and detector) allows asynchronous data collection of both the internal and external modes without disturbing the sample.

Powder X-ray diffraction (PXRD) was used to provide structural confirmation by an independent method. An attempt was made to correlate the observed vibrational modes differences with structural information (microstrain fluctuations, crystalline domain size) determined from PXRD data as previously done with transmission FTIR measurements of calcite samples.[40,41]

This work is published as S. Campbell and K. M. Poduska. Incorporating far-infrared data into carbonate mineral analyses. Minerals, 10(7):628, 2020. doi: 10.3390/min10070628.

2.4.2 Chapter 4: Photoacoustic enhancement

Photoacoustic (PAS) FTIR has enhanced intensities for weak spectral features in the Mid-IR region compared to transmission FTIR and ATR-FTIR, with no published theoretical explanation.[23,24,30,39] Chapter 4 eliminates different possible explanations through carefully designed experiments.[11] We use purchased calcite as a sample due to the clear, non-overlapping spectral bands present in the Mid-IR energy range. The optics within the PAS cell limit this investigation to this range, as they

block the beam in the Far-IR region. As the main cause of this enhancement is often thought to be detector saturation, we began with basic experiments in which data were collected at increasing scan speeds (mirror velocity). The amount of PAS signal is proportional to mirror speed, as slower speeds result in greater thermal wave generation. We observed no relative peak intensity or shape changes in the spectra as the scan speed increased. As additional support, we calculated linearized spectra, which showed that the varied modulation frequency across the spectral range was not a factor. To further this point, we collected step-scan data in which the entire spectral range is collected at the same modulation frequency, ultimately showing no significant difference. Lastly, we collected data for the same calcite samples using two available PAS cells with different transducers (microphone and cantilever). All these experiments show the repeatability of the weak peak enhancement while decisively eliminating saturation as the cause.

This work is published as S. Campbell, M. Dusseault, B. Xu, K. H. Michaelian, and K. M. Poduska. Photoacoustic detection of weak absorption bands in infrared spectra of calcite. Applied Spectroscopy, 75(7):795–801, 2021. doi: 10.1177/00037028211009212. PMID: 33783238.

Bibliography

[1] A. Badawi. Photoacoustic study of alloyed $Cd_{1-x}Pb_xS$ quantum dots sensitized solar cells electrodes. Journal of Materials Science: Materials in Electronics, 27(8):7899–7907, 2016.

[2] A. Badawi, N. Al-Hosiny, S. Abdallah, S. Negm, and H. Talaat. Photoacoustic study of optical and thermal properties of CdTe quantum dots. Journal of Materials Science and Engineering A, 2:1–6, 2012.

[3] G. Bekiaris, S. Bruun, C. Peltre, S. Houot, and L. S. Jensen. FTIR–PAS: A powerful tool for characterising the chemical composition and predicting the labile C fraction of various organic waste products. Waste Management, 39:45 – 56, 2015. ISSN 0956-053X. doi: http://dx.doi.org/10.1016/j.wasman.2015.02.029.

[4] G. Bekiaris, J. M. Triolo, C. Peltre, L. Pedersen, L. S. Jensen, and S. Bruun. Rapid estimation of the biochemical methane potential of plant biomasses using fourier transform mid-infrared photoacoustic spectroscopy. Bioresource Technology, 197:475 – 481, 2015. ISSN 0960-8524. doi: http://dx.doi.org/10.1016/j.biortech.2015.08.050.

[5] G. Bekiaris, C. Peltre, L. Jensen, and S. Bruun. Using FTIR-photoacoustic spectroscopy for phosphorus speciation analysis of biochars. Spectrochimica Acta Part A: Molecular and Biomolecular Spectroscopy, 168:29–36, 2016. doi: 10.1016/j.saa.2016.05.049.

[6] A. G. Bell. On the production and reproduction of sound by light. American Journal of Science, Series 3 Vol. 20(118):305–324, 1880. doi: 10.2475/ajs.s3-20.118.305.

[7] M.-M. Blum and H. John. Historical perspective and modern applications of attenuated total

reflectance–Fourier transform infrared spectroscopy (ATR-FTIR). Drug Testing and Analysis, 4 (3-4):298–302, 2012.

[8] T. N. Brusentsova, R. E. Peale, D. Maukonen, G. E. Harlow, J. S. Boesenberg, and D. Ebel. Far infrared spectroscopy of carbonate minerals. American Mineralogist, 95(10):1515–1522, 2010.

[9] L. Burggraf and D. Leyden. Quantitative photoacoustic spectroscopy of intensely light-scattering thermally thick samples. Analytical Chemistry, 53(6):759–764, 1981.

[10] S. Campbell and K. M. Poduska. Incorporating far-infrared data into carbonate mineral analyses. Minerals, 10(7):628, 2020. doi: 10.3390/min10070628.

[11] S. Campbell, M. Dusseault, B. Xu, K. H. Michaelian, and K. M. Poduska. Photoacoustic detection of weak absorption bands in infrared spectra of calcite. Applied Spectroscopy, 75(7):795–801, 2021. doi: 10.1177/00037028211009212. PMID: 33783238.

[12] R. Carter III. The application of linear PA/FT-IR to polymer-related problems. Applied Spectroscopy, 46(2):219–224, 1992.

[13] C. Carteret, M. De La Pierre, M. Dossot, F. Pascale, A. Erba, and R. Dovesi. The vibrational spectrum of $CaCO_3$ aragonite: A combined experimental and quantum-mechanical investigation. The Journal of Chemical Physics, 138(1):014201, 2013. ISSN 0021-9606. doi: 10.1063/1.4772960.

[14] L. Couture. Etude des spectres de vibrations de monocristaux ioniques. In Annales de physique, volume 12, pages 5–94. EDP Sciences, 1947.

[15] C. Du, J. Zhou, H. Wang, X. Chen, A. Zhu, and J. Zhang. Determination of soil properties using Fourier transform mid-infrared photoacoustic spectroscopy. Vibrational Spectroscopy, 49(1): 32–37, Jan. 2009. ISSN 0924-2031. doi: 10.1016/j.vibspec.2008.04.009.

[16] J. El Haddad, B. Bousquet, L. Canioni, and P. Mounaix. Review in terahertz spectral analysis. TrAC Trends in Analytical Chemistry, 44:98–105, 2013. ISSN 0165-9936. doi: https://doi.org/10.1016/j.trac.2012.11.009.

[17] R. Gueta, A. Natan, L. Addadi, S. Weiner, K. Refson, and L. Kronik. Local atomic order and infrared spectra of biogenic calcite. Angewandte Chemie International Edition, 46(1-2):291–294, Jan. 2007. ISSN 1521-3773. doi: 10.1002/anie.200603327.

[18] K. Hellwege, W. Lesch, M. Plihal, and G. Schaack. Zwei-phononen-absorptionsspektren und dispersion der schwingungszweige in kristallen der kalkspatstruktur. Zeitschrift für Physik A Hadrons and Nuclei, 232(1):61–86, 1970.

[19] M. Hussin, M. Bhutta, M. Azreen, P. Ramadhansyah, and J. Mirza. Performance of blended ash geopolymer concrete at elevated temperatures. Materials and Structures, 48(3):709–720, 2015.

[20] C.-L. Jiang, W. Zeng, F.-S. Liu, B. Tang, and Q.-J. Liu. First-principles analysis of vibrational modes of calcite, magnesite and dolomite. Journal of Physics and Chemistry of Solids, 131:1–9, 2019.

[21] L. L. Long, M. R. Querry, R. J. Bell, and R. W. Alexander. Optical properties of calcite and gypsum in crystalline and powdered form in the infrared and far-infrared. Infrared Physics, 34:191–201, 1993. URL https://api.semanticscholar.org/CorpusID:12236767.

[22] D. Lou, F. Sun, and L. Li. Study on vibrational modes by group theory and infrared spectra by DFT for calcite crystal. Chinese Optics Letters, 5(6):370–372, 2007.

[23] K. Michaelian, Q. Wen, B. Billinghurst, J. Shaw, and V. Lastovka. Far-and mid-infrared photoacoustic spectra of tetracene, pentacene, perylene and pyrene. Vibrational Spectroscopy, 58: 50–56, 2012.

[24] K. Michaelian, S. Oladepo, J. Shaw, X. Liu, D. Bégué, and I. Baraille. Raman and photoacoustic infrared spectra of fluorene derivatives: Experiment and calculations. Vibrational Spectroscopy, 74:33–46, 2014.

[25] K. H. Michaelian. Photoacoustic Infrared Spectroscopy. Wiley-Interscience, Hoboken, N.J., 2003. ISBN 0471134775. Errata inserte.

[26] K. H. Michaelian. Invited article: Linearization and signal recovery in photoacoustic infrared spectroscopy. Review of Scientific Instruments, 78(5):051301, 2007. doi: http://dx.doi.org/10.1063/1.2735447.

[27] K. H. Michaelian. Photoacoustic IR Spectroscopy: Instrumentation, Applications and Data Analysis. Wiley-VCH, 2010.

[28] K. H. Michaelian, R. H. Hall, and K. I. Kenny. Photoacoustic infrared spectroscopy of Syncrude post-extraction oil sand. Spectrochimica Acta Part A: Molecular and Biomolecular Spectroscopy, 64(3):703–710, June 2006. ISSN 1386-1425. doi: 10.1016/j.saa.2005.07.072.

[29] K. H. Michaelian, B. E. Billinghurst, J. M. Shaw, and V. Lastovka. Far-infrared photoacoustic spectra of tetracene, pentacene, perylene and pyrene. Vibrational Spectroscopy, 49(1):28–31, Jan. 2009. ISSN 0924-2031. doi: 10.1016/j.vibspec.2008.04.005.

[30] M. Natale and L. N. Lewis. Application of PAS for the investigation of overtones and combinations in the near IR. Applied Spectroscopy, 36(4):410–413, 1982.

[31] J. Pan, H. Zhao, M. E. Tucker, J. Zhou, M. Jiang, Y. Wang, Y. Zhao, B. Sun, Z. Han, and H. Yan. Biomineralization of monohydrocalcite induced by the halophile halomonas smyrnensis WMS-3. Minerals, 9(10):632, 2019.

[32] K. M. Poduska, L. Regev, E. Boaretto, L. Addadi, S. Weiner, L. Kronik, and S. Curtarolo. Decoupling local disorder and optical effects in infrared spectra: Differentiating between calcites with different origins. Advanced Materials, 23(4):550–554, 2011. ISSN 1521-4095. doi: 10.1002/adma.201003890.

[33] K. M. Poduska, L. Regev, F. Berna, E. Mintz, I. Milevski, H. Khalaily, S. Weiner, and E. Boaretto. Plaster characterization at the PPNB site of Yiftahel (Israel) including the use of ^{14}C: implications for plaster production, preservation, and dating. Radiocarbon, 54(3-4):887–896, 2012.

[34] Powder Diffraction File. Joint commission on powder diffraction standards – international centre for diffraction data, 2003. URL `www.icdd.com`.

[35] L. Regev, K. M. Poduska, L. Addadi, S. Weiner, and E. Boaretto. Distinguishing between calcites formed by different mechanisms using infrared spectrometry: archaeological applications. Journal of Archaeological Science, 37(12):3022–3029, 2010.

[36] M. B. Toffolo and E. Boaretto. Nucleation of aragonite upon carbonation of calcium oxide and calcium hydroxide at ambient temperatures and pressures: a new indicator of fire-related human activities. Journal of Archaeological Science, 49:237–248, 2014.

[37] W. B. White. The Carbonate Minerals. In The Infrared Spectra of Minerals. Mineralogical Society of Great Britain and Ireland, 01 1974. ISBN 9780903056052. doi: 10.1180/mono-4.12.

[38] G. Williamson and W. Hall. X-ray line broadening from filed aluminium and wolfram. Acta Metallurgica, 1(1):22–31, 1953.

[39] B. Xu. Assessing different types of disorder in carbonate minerals with vibrational spectroscopy. PhD thesis, Memorial University of Newfoundland, St. John's, Newfoundland, October 2015.

[40] B. Xu and K. M. Poduska. Linking crystal structure with temperature-sensitive vibrational modes in calcium carbonate minerals. Physical Chemistry Chemical Physics, 16(33):17634–17639, 2014.

[41] B. Xu, M. B. Toffolo, L. Regev, E. Boaretto, and K. M. Poduska. Structural differences in archaeologically relevant calcite. Analytical Methods, 7(21):9304–9309, 2015.

[42] B. Xu, M. B. Toffolo, E. Boaretto, and K. M. Poduska. Assessing local and long-range structural disorder in aggregate-free lime binders. Industrial and Engineering Chemistry Research, 55(30): 8334–8340, 2016.

[43] B. Xu, A. Hirsch, L. Kronik, and K. M. Poduska. Vibrational properties of isotopically enriched materials: the case of calcite. RSC Advances, 8(59):33985–33992, 2018.

[44] Y. Zhu, N. Ma, W. Jin, S. Wu, and C. Sun. Genomic and transcriptomic insights into calcium carbonate biomineralization by marine actinobacterium Brevibacterium linens BS258. Frontiers in Microbiology, 8:602, 2017.

Chapter 3

Incorporating far infrared data into carbonate mineral analyses

This chapter was published as S. Campbell and K. M. Poduska. Incorporating far-infrared data into carbonate mineral analyses. Minerals, 10(7):628, 2020. doi: 10.3390/min10070628.

Following discussions with thesis examiners during the defense proceedings, additions, alterations and further clarifications related to this published work are reported in Appendix C. Of particular note, nomenclature in this work refers to internal carbonate modes as “local modes” and external modes as “lattice modes”.

Co-authorship statement

This work represents a collaborative effort by me and my supervisor, Dr. Kristin M. Poduska. As first author, the laboratory experiments, data curation, and original draft preparation were my responsibility. Conceptualization, resources, supervision, project administration, and funding acquisition were handled by Dr. Poduska. The methodology, formal analysis, review and editing of the text were done

collaboratively by Dr. Poduska and me.

Abstract

Polycrystalline carbonate minerals (including calcite, Mg-calcite, and aragonite) can show distinctive variations in their far-infrared (FIR) spectra. We describe how to identify mixed-phase samples by correlating FIR spectral changes with mid-infrared spectra, X-ray diffraction data, and simple peak overlap simulations. Furthermore, we show how to distinguish portlandite-containing ($Ca(OH)_2$) mixtures that are common in heated calcium carbonate samples. Ultimately, these results could be used for tracking how minerals are formed and how they change during environmental exposure or processing after extraction.

3.1 Introduction

Calcium carbonate minerals ($CaCO_3$), including calcite and aragonite, are relevant for geoscience, archaeology, construction materials, and biomineralization[1,4,8,12,14,22]. Mixtures of these carbonate phases often exist together, and detecting the components that exist in these mixtures can be important for tracking how minerals are formed and how they change during environmental exposure or processing after extraction[12,14,18,19]. However, there are distinct challenges with these carbonates because there are multiple polymorphs of $CaCO_3$ (calcite, aragonite, vaterite), and there is the tendency for amorphous or poorly crystalline phases to exist. This means that standard powder X-ray diffraction measures alone are not always sufficient to characterize carbonate mineral mixtures effectively.

A quick and easy way to assess small volumes of carbonate materials is infrared spectroscopy, which is one of the most widely used forms of vibrational spectroscopy. Not only are alloys and polymorphs often detectable from peak shifts, but amorphous forms of carbonate minerals also show distinctive infrared spectral variations in the mid-infrared (MIR) range[3]. This range of energies (400-4000 cm^{-1}, which is equivalent to 12-120 THz or 25-2.5 microns) corresponds to vibrations within single carbonate moieties. Even in crystalline calcite, MIR spectra show distinctive peak broadening trends that are correlated with crystallinity differences arising from greater microstrain fluctuation values and smaller crystalline domain sizes[19]. Earlier theoretical work demonstrated that analogous

crystallinity differences do indeed trigger systematic peak broadening trends[3,15].

Carbonates are not often investigated in the Far-IR (FIR) energy range (80-650 cm^{-1}, which is equivalent to 2.4-19.5 THz or 125-15.4 microns), but FIR spectra can offer valuable insights about lower energy lattice vibrations that correspond to vibrations among – rather than within – different carbonate units. In principle, lattice modes should be subject to similar kinds of peak shifts, relative intensity differences, and broadening effects that are observed in the MIR energy range. However, there are gaps in the FIR knowledge base for two primary reasons. First, the spectrometer optical components required for this energy range must be different than the standard ionic alkali halide (KBr) windows that absorb heavily in the FIR range. Second, theoretical calculations related to lattice mode energies are lacking because the quantum chemical calculations that work well to study MIR vibrations are not feasible for lattice modes with high dispersion[3].

In this work, we show how experimentally obtained FIR spectra can be a valuable part of carbonate composition analyses. To do this, we make new and explicit links between FIR and MIR spectra, and we support our findings with complementary X-ray diffraction data and simple, yet effective, peak overlap simulations.

3.2 Materials and Methods

3.2.1 Calcite crystal structure and vibrational modes

The crystal structure of calcite is often described with an hexagonal unit cell (space group $P\bar{3}1m$) that contains four formula units which are arranged in a way that produces alternating layers (in the x-y plane) of calcium ions and carbonate units (which are rotated 60° with respect to each other)[11]. The vibrational modes for calcite are typically derived from an analysis of its primitive rhombohedral unit cell which contains 10 atoms (two formula units). The energies and symmetries of calcite's 27 possible vibrational modes have been verified by many different theoretical and experimental studies[1,5,6,16]. There are four possible vibrations within a single carbonate moiety, but only three have a dipole moment that makes them IR-active. In the literature, these three modes have the following labels: ν_2 designates out-of-plane bending, ν_3 is asymmetric stretching and ν_4 is the in-plane bending or

wagging. There are five additional IR-active lattice vibrational modes that are more challenging to describe because they involve relative translations of the calcium and carbonate ions. These lattice modes also have spectroscopic designations (ν labels), but because some are close in energy, the spectral peaks associated with these lattice modes are usually reported as three bands: 300 cm^{-1} (comprised of ν_6 and ν_8, which we designate in this work as B1), 220 cm^{-1} (corresponding to ν_9, which we call B2), and 100 cm^{-1} (comprised of ν_7 and ν_{10}, which we refer to as B3). Excellent animations of all IR-active local and lattice modes in calcite can be viewed online[15].

3.2.2 Samples

Table 3.1 lists nine samples that are the focus of this study. We used a purchased calcite ($CaCO_3$) powder (Alfa Aesar) as a reference. Other as-received samples were geogenic calcite (Woody Point, Newfoundland & Labrador, Canada) and biogenic Mg-calcite (sea urchin, Newfoundland & Labrador, Canada).

Heated samples H1 and H2 were formed by exposing limestone (calcite) to a wood fire outdoors[12]. H3, H4, H5 were produced from calcium carbonate powders that were heated in a laboratory oven to temperatures of 800-900 °C, and then slaked with water. The chemistry of heat-treated and slaked calcite is well-documented in the production of lime binders,[14], with mixtures of calcite, aragonite, and portlandite ($Ca(OH)_2$) being characteristic products of this process. We note that, because the temperature-dependent sample fabrication process yields inherently mixed-phase samples, it is not feasible to separate and then quantify the overall aragonite and calcite content within these types of samples[12,14].

Aragonite (sample AR) was synthesized by a solution-based precipitation method involving 25 mL 60 mM Na_2CO_3 (pH=10.9) added into 25 mL 60 mM $CaCl_2$ (pH=7.2), drop by drop over the span of three minutes while stirring at 400 rpm and heating at 90°C. After cooling to room temperature, the precipitates were separated from the suspension by centrifugation (4000 rpm for 10 minutes), filtered, and dried at ambient temperature for 12 hours.

Name	Description
C1	Purchased calcite
C2	Geogenic calcite
M1	Biogenic Mg-calcite
H1	Field-heated calcite[12]
H2	Field-heated calcite[12]
H3	Lab-synthesized lime binder[20]
H4	Lab-synthesized lime binder[20]
H5	Lab-synthesized lime binder[20]
AR	Lab-synthesized aragonite

Table 3.1 Summary of calcium carbonate samples used in this work.

3.2.3 Attenuated total reflectance IR spectroscopy

All data were collected using a Bruker Vertex 70v vacuum Fourier transform infrared (FTIR) spectrometer with Platinum Diamond attenuated total reflectance (ATR) attachment and a globar (blackbody) light source. Measurements were made under vacuum with 2 cm^{-1} resolution. Due to absorbance characteristics of the spectrometer optics, data were collected two separate spectral ranges using either a KBr beamsplitter (4000 cm^{-1} - 400 cm^{-1}), or a Mylar beamsplitter (650 cm^{-1} - 80 cm^{-1}).

The data collection procedure involved repeated measurements, regrinding by hand using a mortar and pestle following each. The rationale for using multiple grinding treatments for our ATR-FTIR measurements is based on previous experience that shows that grinding sharpens transmission FTIR spectra when preparing samples in dilute KBr pellets[9,12]. Although the scattering geometry for ATR samples is very different from samples diluted in KBr pellets, we observed similar ATR peak sharpening using successive grinding treatments. Because large particle size are known to broaden ATR peaks, we use repeated grindings (typically 3-4 times) until the peak shapes show minimal changes, whether remounting and measuring the same powder, or by grinding and remeasuring a different portion of the same sample batch. Repeated measurements on the same powder showed variations of detected peak position ± 2 cm^{-1} (see Supplemental Materials). This allows us to minimize sample-to-sample differences that could be caused by non-uniform particle size in an efficient and expedient way.

FTIR data in this work are displayed according to the common convention of ATR intensity vs. wavenumber, where the wavenumber axis is displayed with decreasing values from left to right.

3.2.4 Powder X-ray diffraction

Powder X-Ray diffraction (PXRD) data were collected for a subset of samples using a Rigaku Ultima IV in $2\theta/\theta$ system using a Cu Kα source. The range $20^\circ \leq 2\theta \leq 70^\circ$ was measured in continuous scanning mode, with a sampling width of 0.02 degrees and a scan speed of 1 degree/minute. Prior to measurement, each sample ($\sim$ 2 g) was ground by hand using a mortar and pestle for several minutes. JADE 2010 software (MDI)[7] aided peak indexing and lattice constant refinements on z-corrected and background-subtracted spectra using 18 calcite peaks.

3.3 Results

Figure 3.1 shows combined MIR (2000 cm^{-1}- 400 cm^{-1}) and FIR (650 cm^{-1}- 80 cm^{-1}) data for the calcite-containing samples listed in Table 3.1. All spectra show the three local vibrational modes of calcite (ν_3 near 1425 cm^{-1}, ν_2 at 875 cm^{-1} and ν_4 at 712 cm^{-1}) and the three lattice mode bands (band 1 (B1), near 300 cm^{-1} (ν_6 and ν_8), band 2 (B2) centered near 220 cm^{-1} (ν_9), and band 3 (B3) near 100 cm^{-1} (ν_7 and ν_{10})). The energies of these vibrational modes have been verified by many different theoretical and experimental studies[1,5,6,16].

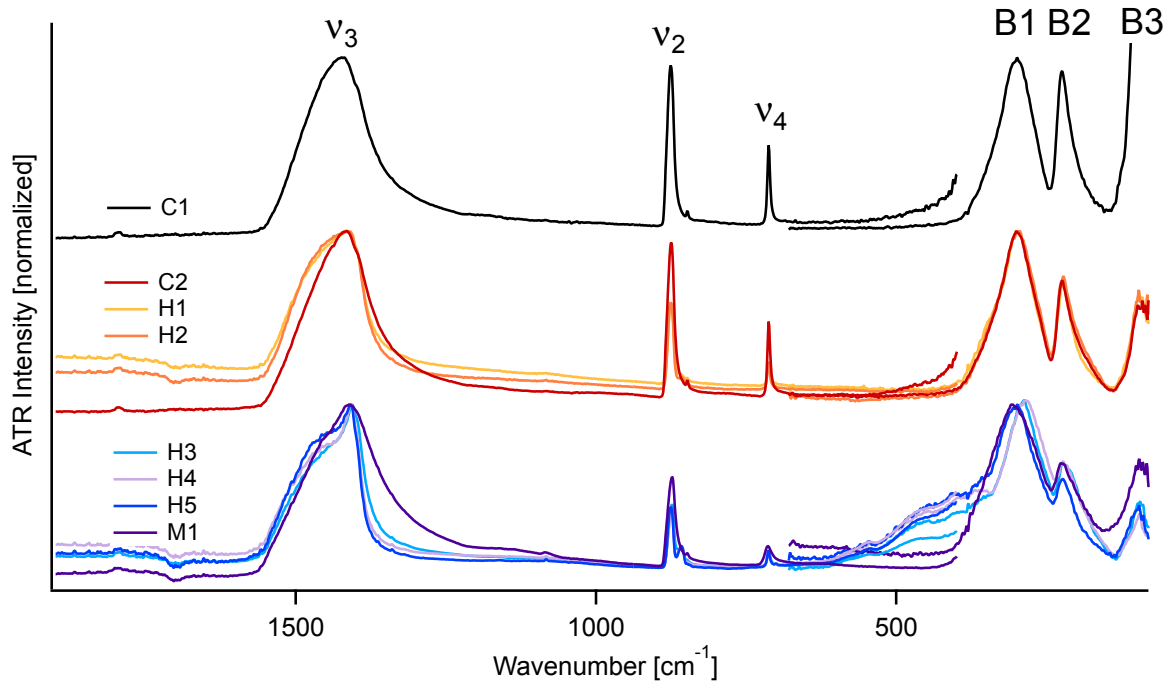

Figure 3.1 Representative MIR (2000 cm^{-1}- 400 cm^{-1}) and FIR (650 cm^{-1}- 80 cm^{-1}) spectra for eight calcite-containing samples, shown on the same plot to demonstrate the extent and overlap of the spectral ranges. The intensity of each spectrum is normalized to either the ν_3 peak (MIR configuration) or the B1 peak (FIR configuration). Spectra are grouped and offset for clarity.

The spectra in Figure 3.1 are grouped in a way that draws attention to similar types of features. Our calcite reference (C1, black) is the top curve. Below that are two groupings. The middle group (C2, H1, and H2, in shades of red) are most similar to the calcite reference, but with slightly broadened ν_3 peaks and decreased B2 and B3 relative peak intensities. The bottom group (H3, H4, H5, M1, in shades of blue) has a sharp ν_3 point, very distinctive broad shoulders from 550-350 cm^{-1}, shifted B1 peaks, and very decreased B2 and B3 relative peak intensities.

In the following sections, we discuss the FIR data first, and then correlate our interpretations of the FIR spectral changes with MIR spectra, PXRD data, and peak overlap simulations.

3.3.1 FIR-ATR

Figure 3.2 gives an expanded view of the FIR (600 cm^{-1}- 80 cm^{-1}) spectra, each of which is normalized to its own B1 peak. The reference calcite (C1) and the middle grouping (H1, H2, C2) have nearly identical spectral band positions and widths for B1 and B2. The main difference with the reference calcite is that it has a higher relative B2 band intensity. We do not attempt to ascribe relative intensity comparisons for band B3 because that spectral feature extends below our low-wavenumber detection limit.

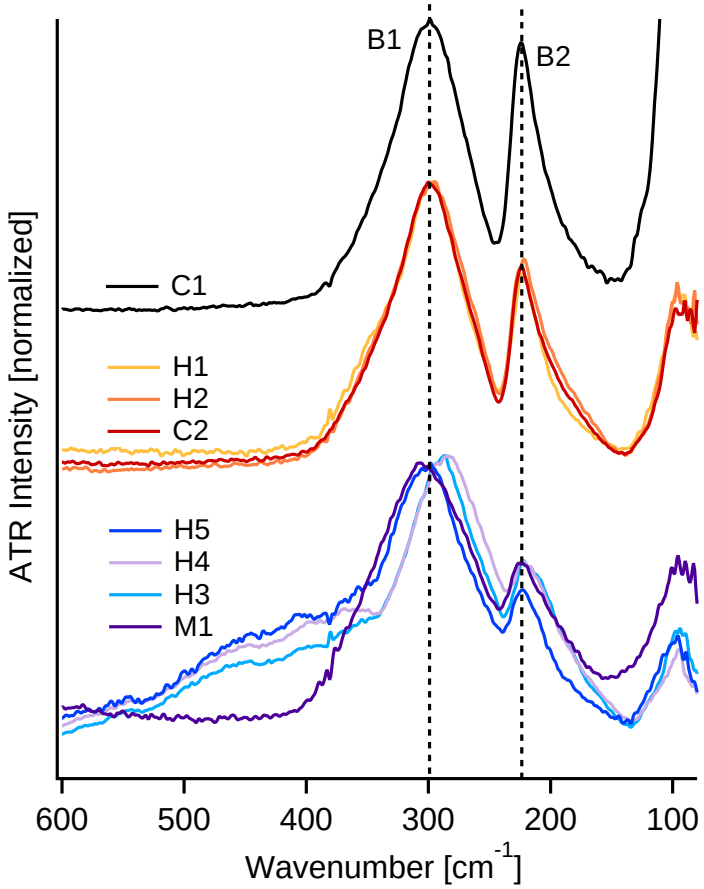

Figure 3.2 Representative FIR spectra (600 cm^{-1}- 80 cm^{-1}) for the same samples shown in Figure 3.1. Here, the intensity of each spectrum is normalized to the B1 peak, and the dashed lines denote the positions of the B1 and B2 peak maxima in the spectrum for the reference calcite. Spectra are grouped and offset for clarity.

In contrast, the bottom set of spectra (H5, H4, H3, M1) show much more variation in their spectral features. In all cases, B1 broadens and shows slight position shifts relative to the reference calcite. Although the position of band B2 remains consistent, that peak is reduced in its relative intensity. Furthermore, samples H3, H4 and H5 have a broad shoulder on the high-wavenumber side of the B1

peak that extends well into the MIR region.

3.3.2 MIR-ATR

To explain the FIR spectral differences, it is helpful to link our observations described above with MIR data for the same samples. Figure 3.3) shows enlarged views of four key MIR regions.

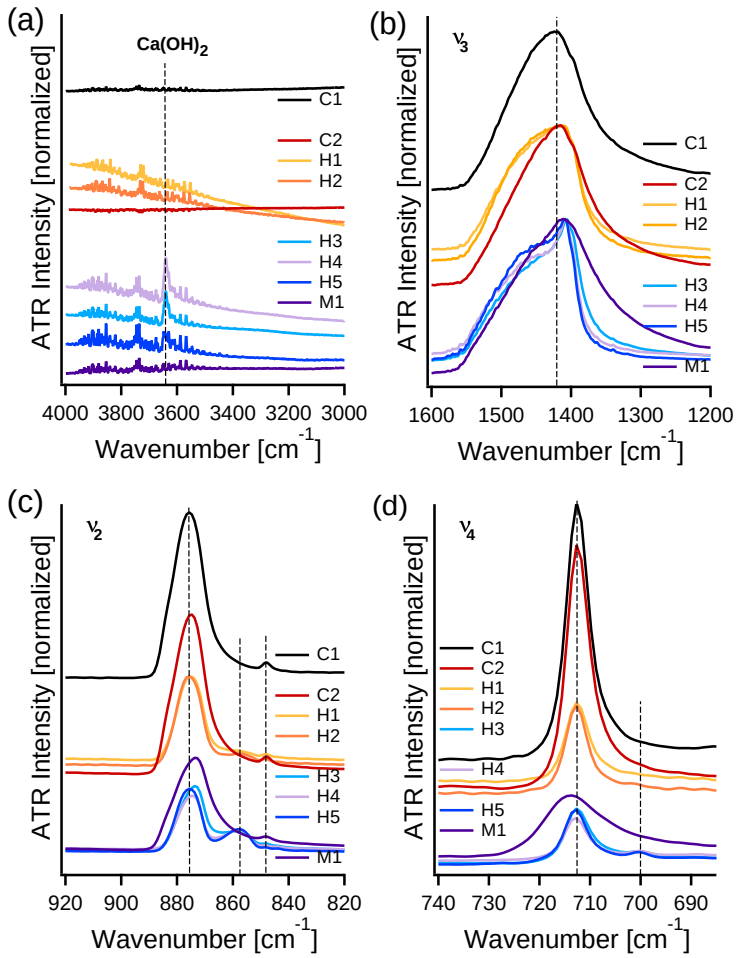

Figure 3.3 Representative MIR spectra, highlighting regions related to (a) OH, (b) ν_3, (c) ν_2, (d) ν_4 peaks. Each spectrum is normalized to the intensity of the ν_3 peak, and spectra are offset and grouped for clarity. In (a), the dominant portlandite ($Ca(OH)_2$) peak position is shown with a dashed line; other peaks are related to water vapor. In (b), the dashed line corresponds to the calcite ν_3 maximum. In (c), the dashed lines correspond to calcite ν_2 (875 cm^{-1}), aragonite ν_2 (858 cm^{-1}), and calcite ^{13}C ν_2 (850 cm^{-1}). In (d), the dashed lines correspond to calcite ν_4 (712 cm^{-1}) and aragonite ν_4 (700 cm^{-1}).

The hydroxide region (Figure 3.3a) shows minor water vapor vibrations for all samples in the 4000-3400 cm^{-1} range. This is a common spectral feature for calcium carbonate powders such as

ours that were not desiccated prior to measurement. For samples, H3, H4, and H5, there are additional peaks near 3640 cm^{-1} that are characteristic of portlandite ($Ca(OH)_2$), which is a well-known intermediate phase that exists in these kinds of lime binder specimens[14].

The same samples that show evidence of $Ca(OH)_2$ in Figure 3.3a also show distinctive ν_3 peak shapes relative to the other samples. In Figure 3.3b, H3, H4, H5 (in the bottom grouping) show a sharp peak on the low-wavenumber side of the ν_3 band. This band shape has been reported previously in FTIR reflectance spectra of lime plasters,[10] but it is not as noticeable in transmission FTIR spectra[9]. In contrast, our reference calcite (C1) shows a broad featureless peak centered near 1425 cm^{-1}. Spectra in the middle grouping (H1, H2, C2) show asymmetric broadening on the high wavenumber side of the ν_3 band; on the other hand, M1 shows extreme broadening on the low-wavenumber side of the ν_3 peak.

The ν_2 and ν_4 peaks (Figure 3.3c, d, respectively) give further insights into the origins of the spectral differences. Our reference calcite (C1) shows characteristic peaks centered at 875 cm^{-1} and 712 cm^{-1}, along with a smaller peak corresponding to the isotopic ^{13}C ν_2 vibrational mode at 850 cm^{-1}[21]. Heated samples H1 and H2 have the same peak positions as the calcite reference with an additional weak peak at 858 cm^{-1} due to aragonite. The relative intensities of the calcite peaks are reduced compared to the reference. Heated samples H3, H4, and H5 show a further weak peak at 700 cm^{-1}, also due to aragonite, as well as the 858 cm^{-1} peak found in the other heated samples. Thus, the heated samples with the most distinctive MIR and FIR spectra are a calcite-rich mixture that contains both aragonite and portlandite as secondary phases.

The biogenic M1 sample shows a broadened ν_2 peak as well as a ν_4 peak that is broad and shifted to slightly higher wave numbers. This ν_4 shift is characteristic of Mg-containing calcite, wherein the lighter mass Mg leads to a higher wavenumber ν_4 peak position[12].

3.3.3 PXRD

PXRD data were collected for the subset of samples that appeared to be closest to pure calcite (C1, H1, H2) to look for evidence of secondary phases or structural differences within the calcite portion of the sample. As an example, Figure 3.4 shows two cases where aragonite appeared as a minor secondary

phase. Close inspection of the MIR data (Figure 3.3c,d) confirms a small aragonite peak at 858 cm^{-1}. The presence of aragonite is not surprising given the previous high-temperature exposure of these samples[12].

Focusing on the dominant calcite phase, we extracted lattice constants for the conventional hexagonal unit cell (Table 3.2) to determine that H1, H2, and C2 have comparable a lattice constants, but that the heated samples have slightly contracted c lattice constants. We attempted Williamson-Hall (WH) analyses to extract crystallite size and microstrain fluctuation values, but the results proved to be inconclusive, likely due to instrumental broadening dominating the widths of our diffraction peaks (see Supplemental Material).

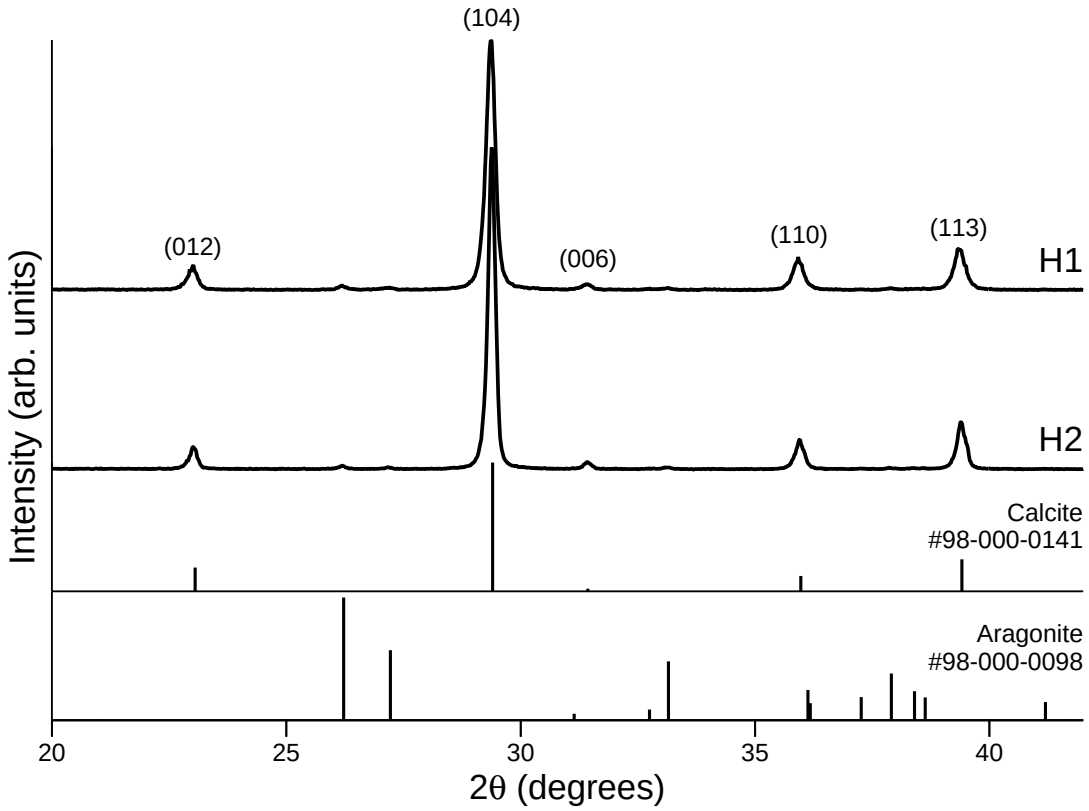

Figure 3.4 PXRD data for H1 and H2 samples, with calcite peak hkl indices labeled. JCPDS references for calcite peaks and aragonite are included as bars below the diffraction data[11].

Name	a (Å)	c (Å)
Literature[2]	4.989	17.061
C1	4.9895(4)	17.061(1)
H1	4.988(1)	17.049(2)
H2	4.990(1)	17.048(2)

Table 3.2 Refined lattice constants for the conventional hexagonal calcite unit cell. Uncertainty estimates, based on whole pattern fitting with at least 18 calcite peaks, are shown in parentheses. The literature value corresponds to JCPDS powder diffraction file 98-000-0141[2,11]

.

3.4 Discussion

Previous work examining calcium carbonate vibrations in the FIR/THz energy range (650 cm^{-1} - 80 cm^{-1}) is sparse. Nevertheless, we are aware of two detailed studies that focused on identifying mode energies for a wide range of carbonate minerals,[1] and identifying Mg-containing carbonate alloy phases[13].

Brunsentsova *et al.* report FIR spectra for calcite, dolomite ($Ca_{0.5}Mg_{0.5}CO_3$) and magnesite ($MgCO_3$), and their data show that the B1 band shifts to higher wavenumbers with higher amounts of Mg incorporation[1]. In a separate study, Sakai *et al.* used Terahertz Time-Domain Spectroscopy (THz-TDS) to collect calcium carbonate lattice vibrational data for the 1-6 THz (30-200 cm^{-1}) range, which includes the B3 band (100 cm^{-1})[13]. They reported that changes in B3 intensity could be used to differentiate among high- and low-Mg calcites, and that the intensity of that band was also influenced by relative amounts of calcite and aragonite in mixed-phase samples.

In the sections below, we put our observed peak position changes and relative intensity changes in the context of this previous work to make explicit links between FIR, MIR, and PXRD studies of calcium carbonate and related minerals. In doing so, we pay special attention to identifying phase mixtures in carbonate minerals that have been exposed to high temperatures, since this has not been reported by others.

3.4.1 FIR peak positions

In our FIR spectra (Figure 3.2), it is the region near the B1 band shows the most variation among different samples.

The most obvious difference is the broad shoulder that extends from 350-550 cm^{-1} in a subset of the heated samples (H3, H4, H5). We attribute this feature to portlandite ($Ca(OH)_2$), since it correlates perfectly with MIR spectra peaks that are consistent with $Ca(OH)_2$ (Figure 3.3a). As noted earlier, $Ca(OH)_2$ is a well-known intermediate phase that appears in lime binders,[12,14] so it is not surprising to find this phase in our heated samples. We note that the $Ca(OH)_2$-related shoulder in FIR spectra is much easier to identify than the weak peaks that appear for this hydroxide phase in the Mid-IR region (near 3640 cm^{-1}) in Figure 3.3a). In this way, it is much easier to detect portlandite in FIR spectra than in MIR spectra. However, the fact that this feature is a broad shoulder rather than a peak means that we do not assign a specific wavenumber to this feature.

Among the heated samples (H1-5), another distinct trend in the FIR spectra is that the B1 band position varies, while the B2 band does not. Comparing with data in the MIR range, these heated samples do not show any shifts in their calcite-related peaks (Figure 3.3c,d). However, all heated samples show evidence of aragonite as a secondary phase, based on MIR features (H1-5 in Figure 3.3c,d) or PXRD data (H1, H2 in Figure 3.4).

We attribute this apparent shift of the B1 peak to the aragonite-calcite phase mixtures in these heated samples. Previous work by others shows that calcite and aragonite each have broad B1 bands that overlap in energy[1]. To demonstrate the implications of this, Figure 3.5a shows how a change in relative intensity between two broad, overlapping peaks can lead to a continuous shift in the energy position of the maximum of the combined peaks. Applying this idea to our samples, a more aragonite-rich mixture could cause the B1 band maximum to shift to lower wavenumber values.

Although the simulated peak overlaps in Figure 3.5a are a simple mathematical exercise, it shows excellent qualitative agreement with the B1 peak changes that we observe in our mixed calcite-aragonite samples. Samples H1 and H2 have lesser amounts of aragonite (much lower aragonite MIR peaks intensities, but aragonite present in PXRD data) and show a B1 shift that is so small that it

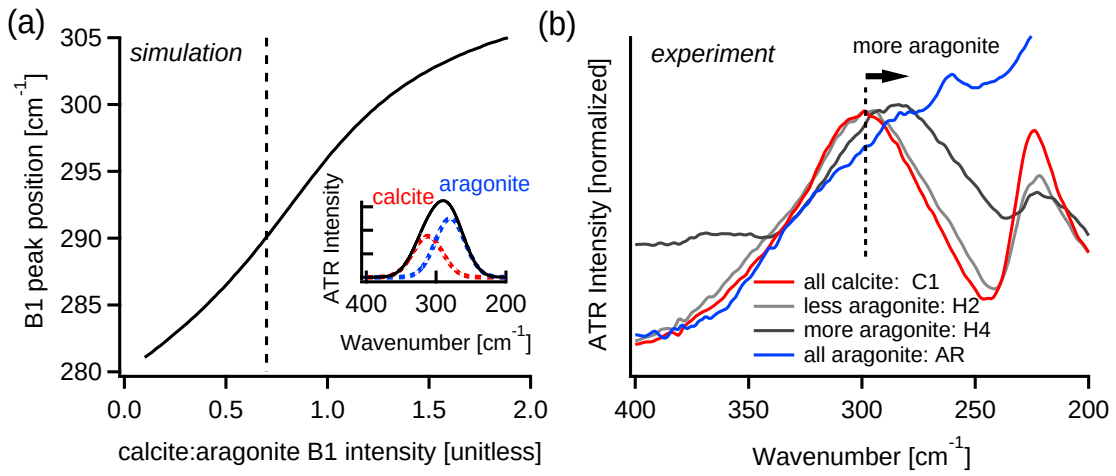

Figure 3.5 (a) A simulation based on a linear combination of two broad, overlapping Gaussian peaks highlights the effect of changing relative peak intensities on the resulting position of the peak maximum. The inset shows two Gaussian peaks (dashed) centered at 312 cm^{-1} and 280 cm^{-1}, and the resultant linear combination (black) with a position of 290 cm^{-1}. Correspondingly, a dashed line vertical line shows that a calcite:aragonite ratio near 0.7 leads to a B1 position of 290 cm^{-1}. In this simulation, changing the relative calcite:aragonite B1 intensity causes a monotonic change in the resulting B1 peak position. (b) Experimental data show a shift of band B1 (near 300 cm^{-1}) to lower wavenumbers for calcite-aragonite mixtures.

is near our minimum detectable shift (see Supporting Material). More apparent B1 peak shifts occur for H3 and H4, both of which have higher relative aragonite peak intensities (Figure 3.3c,d). We note that H5 has a higher amount of aragonite, yet does not have a discernible B1 band shift. In this case, we suspect that the relatively high amount of $Ca(OH)_2$ may be a contributor to the B1 band, which could disrupt the simple trend that we suggest for aragonite:calcite mixtures. It is possible that the band position change is dominated by the portlandite contribution, while the overall band shape change is related to the aragonite. Thus, less portlandite could mean a peak shape change with minimal (or no) B1 shift.

Our comparisons in Figure 3.5 highlight a simple – but important – distinction that makes interpreting FIR spectral trends very different than what has been reported for carbonates in the MIR. In this work, we show that apparent peak shifts may occur due to phase mixing (contamination) resulting in changes to the relative intensities of overlapping broad peaks. This is important because a peak shift in MIR and FIR spectra is generally attributed to an alloy (composition) change[1,12].

Finally, we had one unique sample in our FIR data: the spectrum for biogenic M1 shows a slight B1 band shift to higher wavenumbers. Earlier FIR studies of Mg-containing calcite-type minerals

(dolomite and magnesite), showed that the B1 band moves to higher wavenumbers with higher levels of Mg incorporation[1]. Recent THz-TDS studies of high- and low-Mg calcite alloys focus on lower energy lattice modes (B3 and others) and do not cover this higher-energy B1 mode[13]. Fortunately, there is extensive MIR literature for Mg-containing calcites, and the blue-shift and broadening of the MIR ν_4 mode that we observe (Figure 3.3d) is entirely consistent with low (<10%) Mg incorporation into calcite, as is common for marine biogenic specimens like our sea urchin shell[12]. Thus, we attribute the B1 band shift for our biogenic M1 sample to Mg incorporation.

3.4.2 FIR relative peak intensities

We note that there are as of yet no comparable quantum chemical calculations that allow us to track changes in FIR peak positions or relative intensities; this is distinctly different from transmission MIR experiments which have the benefit of quantum chemical calculations to back them[3,9,15,21]. This knowledge gap in the FIR is related in part to the computational expense of the large supercells required to accommodate lattice vibrational modes, and also in part to the inherent energy dispersion of lattice modes[3].

There is also a very important distinction between the work we present here (based on ATR-FTIR) and these previous transmission MIR data: ATR peaks have different line profiles and relative intensity profiles compared with spectra collected from diluted powders that are well-dispersed in a KBr pellet for transmission FTIR measurements[10]. These spectral differences between ATR and transmission IR data may seem small, but our experience shows us that they are important. The first challenge is that the peaks in ATR spectra are visibly asymmetric, which makes it unwise to use peak deconvolution with Gaussian, Lorentzian, or pseudo-Voigt functions. In contrast, transmission IR peaks are often well-enough approximated by Gaussian functions to allow for peak deconvolution. The second challenge is that our bands B1 and B3 are known to be comprised of more than one vibrational mode, but their energies are so close – relative to the width of the peaks – that it is not feasible to resolve individual peaks.

We note that previous MIR studies of calcites have utilized grinding curves to quantify differences in peak intensity ratios[9,12,18]. As tempting as it is to explore, grinding curves are not rigorously

applicable to our ATR-FTIR data. Nevertheless, we find that our MIR ATR data have qualitatively similar relative peak intensities to the transmission MIR data: ν_3 has higher intensity than ν_2 which has higher intensity than ν_4. Thus, we make only qualitative peak intensity comparisons in our FIR-ATR spectra by analogy with transmission MIR data that has been verified by quantum chemical calculations.

The most robust relative peak intensity differences occur between the B1 and B2 bands (300 cm^{-1} and 220 cm^{-1}, respectively, in Figure 3.2). H1 and H2 show a larger relative B2 intensity compared to the other heated samples (H3, H4, H5); all heated samples have a smaller relative B2 intensity compared to the calcite reference C1. We note that these groupings of FIR relative peak intensity trends mirror the relative peak intensity trends that we see in MIR data (ν_2 and ν_4) for the same samples. Thus, although we can see similar changes in the FIR B2:B1 that mirror qualitatively the MIR ν_4:ν_2, these data do not allow us to determine if the relative intensity differences is related to compositional differences or crystallinity differences. The limitations we encounter in evaluating examining crystallinity-related lattice mode changes in our mixed phase samples could potentially be addressed in a future study by using carefully controlled pure-phase samples to assess spectral changes due to crystallinity differences more definitively.

3.5 Conclusions

Our explicit links between FIR and MIR data are the first of its kind, and it helps move us toward our ultimate goal of using spectroscopic analysis strategies for tracking structural differences in materials that are due to processing, aging, or use-based changes. We demonstrate that calcite-aragonite-portlandite mixtures can show apparent peak shifts in FTIR-ATR spectra (650 cm^{-1} - 80 cm^{-1}). We show that relative peak intensity changes between overlapping peaks – without peak energy shifts in the constituent peaks – are sufficient to explain peak position changes. These results are particularly useful in heat-treated calcium carbonate samples wherein phase mixtures are common.

Author Contributions

Conceptualization, resources, supervision, project administration, and funding acquisition: K.M.P.; methodology, formal analysis, writing–review and editing: S.C. and K.M.P.; laboratory experiments, data curation, writing–original draft preparation: S.C. Both authors have read and agreed to the published version of the manuscript.

Funding

This research and the article processing charges are funded by the Natural Sciences and Engineering Research Council (Canada) Discovery Grant number 2018-04888.

Acknowledgments

Thanks to Dr. L. Regev (Weizmann Institute of Science), Dr. M. Toffolo (Université Bordeaux Montaigne), and B. Gao (Memorial University) for carbonate samples, thanks to J. Aimee (Memorial University) for coding the initial stages of the peak overlap simulation. PXRD data were collected through the CREAIT network (Memorial University) with the help of Dr. W. Aylward.

Conflicts of Interest

The authors declare no conflict of interest. The funders had no role in the design of the study; in the collection, analyses, or interpretation of data; in the writing of the manuscript, or in the decision to publish the results.

Supplementary Materials

Attenuated total reflectance (ATR) measurement repeatability

Repeated measurements of a single powdered sample highlights that attenuated total reflectance (ATR) Fourier transform infrared (FTIR) spectroscopic measurements have some variability in peak

positions and shapes. Large particle sizes can cause broad and asymmetric peak shapes. This effect can be reduced by grinding powder samples thoroughly prior to measurement. Even after repeated grindings, spectra that involved repressing the same powder against the ATR crystal multiple times resulted in a peak position shift of as much as ± 4 cm^{-1}. As an example, Figure 3.6 shows representative spectra near the B1 band for a calcite reference sample. Thus, while it is necessary to have a well ground sample, it is also important to record spectra when the powder is repressed against the ATR crystal in different ways. Failure to do so could lead to mis-attributing subtle spectral changes to crystallinity-related differences that are, in fact, related to heterogeneous particle distributions that are in contact with the ATR crystal.

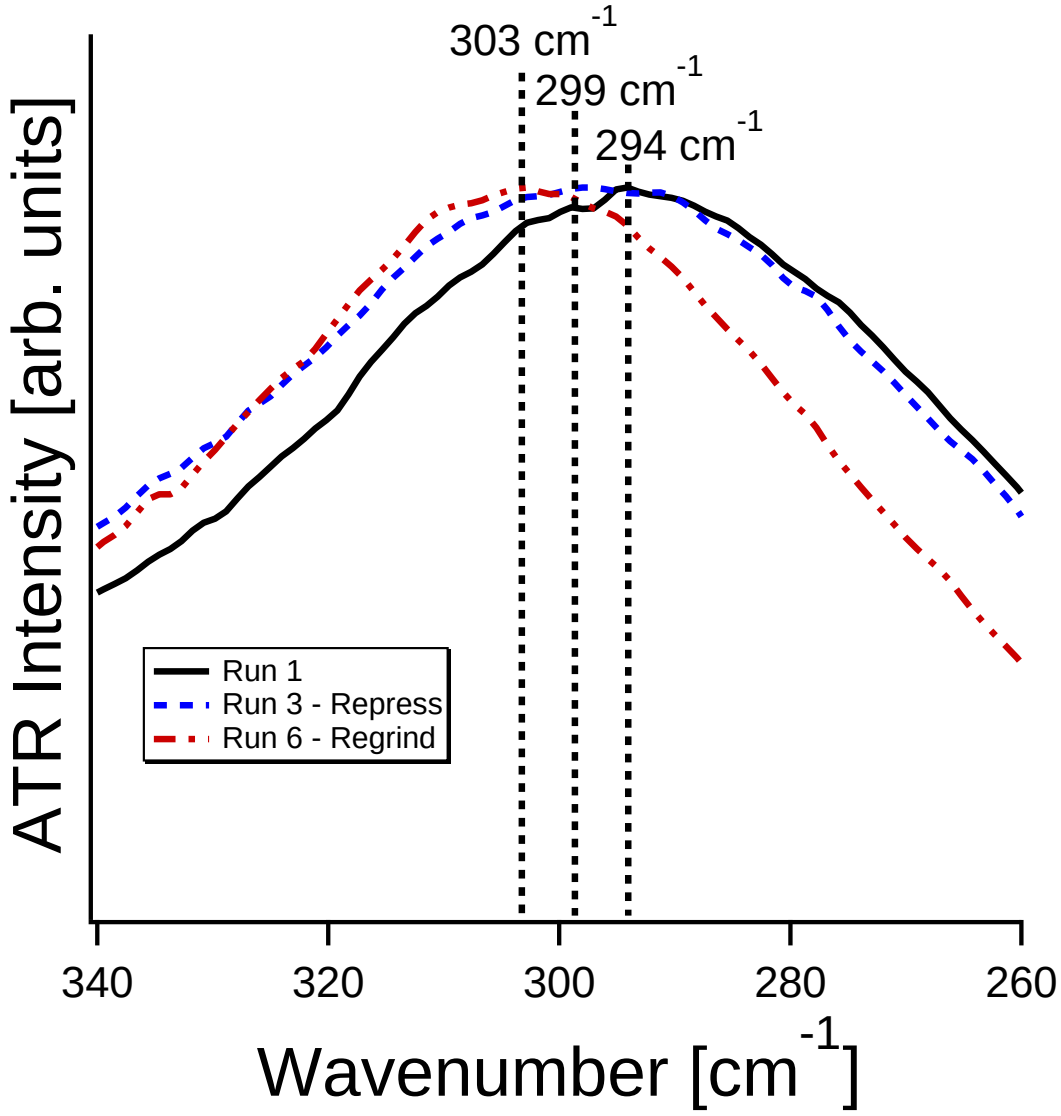

Figure 3.6 The inherent variability associated with repeated measurements of a calcite reference powder. Further grinding results in more narrow peaks. Peak maxima can shift ± 4 cm^{-1}.

Powder X-ray diffraction (PXRD) data

JADE software (MDI)[7] facilitated our assessments of crystalline grain size, microstrain fluctuation values and lattice strain, all of which were based on background subtracted, z-corrected, whole pattern fits for calcite identified diffraction peaks. Microstrain fluctuations and crystalline domain size information can be determined in the JADE software using the Williamson-Hall relation:[17,19]

$$\mathrm{FWHM}\cos\theta = \frac{K\lambda}{r} + 4\sigma\sin\theta \ , \tag{3.1}$$

where FWHM is the full-width at half maximum for a given diffraction peak, θ is the Bragg diffraction angle of the same peak, r is the crystalline domain size, σ is the microstrain fluctuation, λ is the incident X-ray wavelength and K is a dimensionless shape factor. Typically a value of 0.9 is used for particles approximated to be roughly spherical. We considered both crystallite size fixed (large) and free (determined from data).

As described by Equation (3.1), the crystalline domain size, r is related inversely to the y-intercept and the microstrain fluctuation values are directly proportional to the slope of Williamson-Hall plot. These fits can only be as good as the quality of the PXRD peak fits; in other words, poor peak fit data can result in large changes to the slope and intercept used to extract the domain size and microstrain fluctuations. In our analyses, we took significant care in selecting which peaks were accurately fit by JADE's whole pattern fit routine. By removing any poorly fit peaks, we improved the confidence in resultant slope and intercept. Figure 3.7 shows a representative example for a calcite reference (C1).

Letting the slope and intercept run free, the slope tends to refine to near zero (corresponding to microstrain fluctuation values near zero) with large non-zero intercepts (corresponding to crystalline domain sizes that are unreasonably small, on the order of a few nanometers). Alternatively, fixing the intercept at zero (for large crystalline domain sizes, on the order of hundreds of nm) leads to a range of different microstrain fluctuation values and a poor linear fit. The uncertainty values for both the crystalline domain size and microstrain are rather large.

Even when using only the diffraction peaks for which we have higher confidence about their fits,

interpretation of our Williamson-Hall data is dicey. All PXRD peak widths appear to artificially large, which forces the Williamson-Hall fit to have a large intercept, which translates to an interpretation of unphysically small (nm-range) crystalline domain sizes. We believe the origin of these broad PXRD peaks is not likely specimen-related; instead, we suspect that peaks widths were dominated by instrumental broadening effects. Thus, we do not draw any conclusions about crystalline domain size or microstrain fluctuation values from our PXRD data.

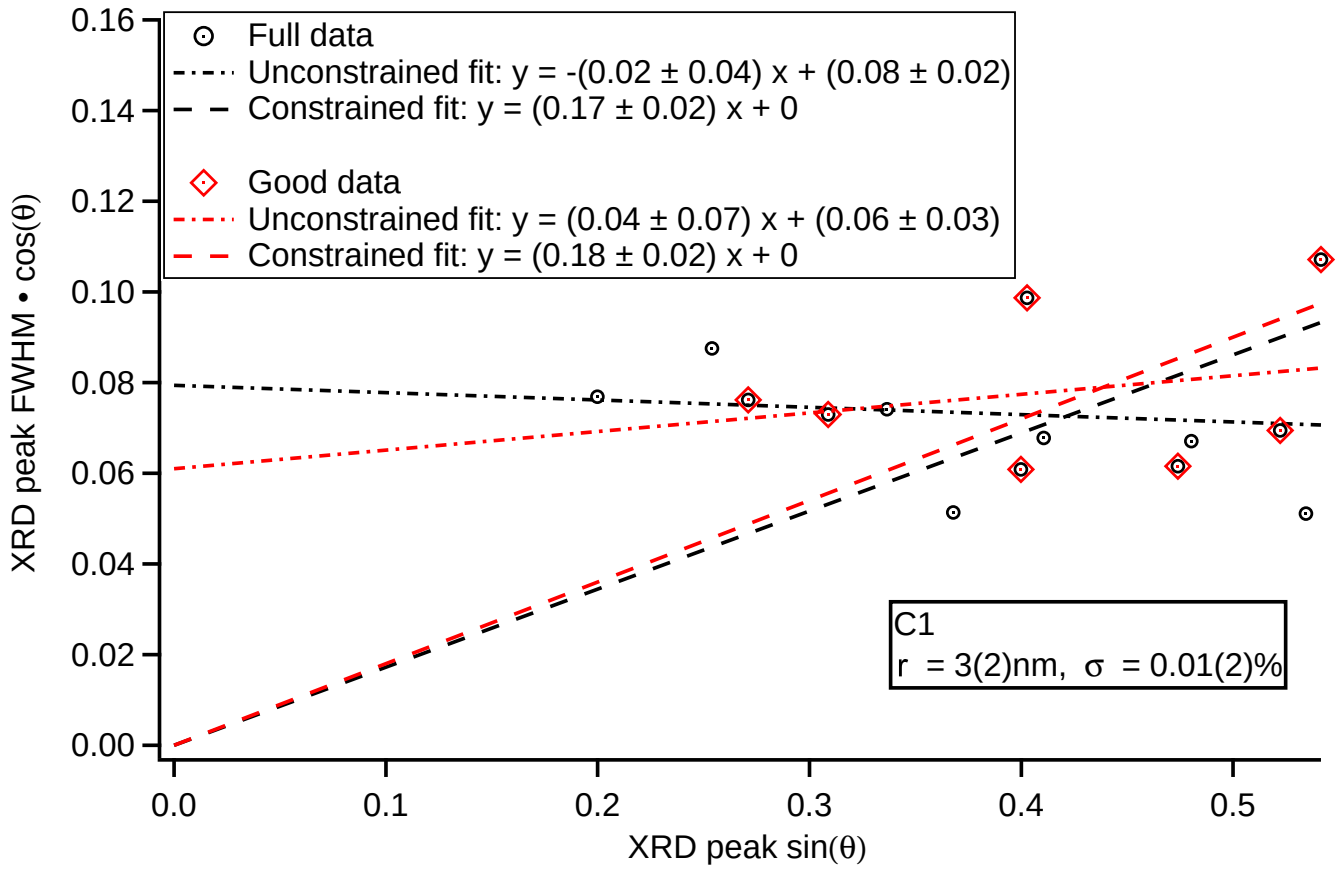

Figure 3.7 Williamson-Hall plot of calcite sample C1. The entire data set (black) and a subset of peaks (red) were fit with either unconstrained intercepts (dot-dashed) or with the intercept forced to zero (dashed).

Bibliography

[1] T. N. Brusentsova, R. E. Peale, D. Maukonen, G. E. Harlow, J. S. Boesenberg, and D. Ebel. Far infrared spectroscopy of carbonate minerals. American Mineralogist, 95(10):1515–1522, 2010.

[2] S. Gates-Rector and T. Blanton. The powder diffraction file: a quality materials characterization database. Powder Diffraction, 34(4):352–360, 2019.

[3] R. Gueta, A. Natan, L. Addadi, S. Weiner, K. Refson, and L. Kronik. Local atomic order and infrared spectra of biogenic calcite. Angewandte Chemie International Edition, 46(1-2):291–294, Jan. 2007. ISSN 1521-3773. doi: 10.1002/anie.200603327.

[4] M. Hussin, M. Bhutta, M. Azreen, P. Ramadhansyah, and J. Mirza. Performance of blended ash geopolymer concrete at elevated temperatures. Materials and Structures, 48(3):709–720, 2015.

[5] C.-L. Jiang, W. Zeng, F.-S. Liu, B. Tang, and Q.-J. Liu. First-principles analysis of vibrational modes of calcite, magnesite and dolomite. Journal of Physics and Chemistry of Solids, 131:1–9, 2019.

[6] D. Lou, F. Sun, and L. Li. Study on vibrational modes by group theory and infrared spectra by DFT for calcite crystal. Chinese Optics Letters, 5(6):370–372, 2007.

[7] MDI. JADE2010 (computer software), 2010. URL `https://materialsdata.com/prodjd.html`.

[8] J. Pan, H. Zhao, M. E. Tucker, J. Zhou, M. Jiang, Y. Wang, Y. Zhao, B. Sun, Z. Han, and H. Yan. Biomineralization of monohydrocalcite induced by the halophile halomonas smyrnensis WMS-3. Minerals, 9(10):632, 2019.

[9] K. M. Poduska, L. Regev, E. Boaretto, L. Addadi, S. Weiner, L. Kronik, and S. Curtarolo. Decoupling local disorder and optical effects in infrared spectra: Differentiating between calcites with different origins. Advanced Materials, 23(4):550–554, 2011. ISSN 1521-4095. doi: 10.1002/adma.201003890.

[10] K. M. Poduska, L. Regev, F. Berna, E. Mintz, I. Milevski, H. Khalaily, S. Weiner, and E. Boaretto. Plaster characterization at the PPNB site of Yiftahel (Israel) including the use of ^{14}C: implications for plaster production, preservation, and dating. Radiocarbon, 54(3-4):887–896, 2012.

[11] Powder Diffraction File. Joint commission on powder diffraction standards – international centre for diffraction data, 2003. URL `www.icdd.com`.

[12] L. Regev, K. M. Poduska, L. Addadi, S. Weiner, and E. Boaretto. Distinguishing between calcites formed by different mechanisms using infrared spectrometry: archaeological applications. Journal of Archaeological Science, 37(12):3022–3029, 2010.

[13] S. Sakai, D. Yang, T. Yasuda, K. Akiyama, T. Kuga, A. Kano, F. Shiraishi, S. Amekawa, S. Ohtsuka, K. Nakaguchi, et al. Pulsed terahertz radiation for sensitive quantification of carbonate minerals. ACS Omega, 4(2):2702–2707, 2019.

[14] M. B. Toffolo and E. Boaretto. Nucleation of aragonite upon carbonation of calcium oxide and calcium hydroxide at ambient temperatures and pressures: a new indicator of fire-related human activities. Journal of Archaeological Science, 49:237–248, 2014.

[15] L. Valenzano, Y. Noel, R. Orlando, C. Zicovich-Wilson, M. Ferrero, and R. Dovesi. Ab initio vibrational spectra and dielectric properties of carbonates: magnesite, calcite and dolomite. Theoretical Chemistry Accounts, 117(5-6):991–1000, 2007. URL `https://tutorials.crystalsolutions.eu/index.html`.

[16] W. B. White. The Carbonate Minerals. In The Infrared Spectra of Minerals. Mineralogical Society of Great Britain and Ireland, 01 1974. ISBN 9780903056052. doi: 10.1180/mono-4.12.

[17] G. Williamson and W. Hall. X-ray line broadening from filed aluminium and wolfram. Acta Metallurgica, 1(1):22–31, 1953.

[18] B. Xu and K. M. Poduska. Linking crystal structure with temperature-sensitive vibrational modes in calcium carbonate minerals. Physical Chemistry Chemical Physics, 16(33):17634–17639, 2014.

[19] B. Xu, M. B. Toffolo, L. Regev, E. Boaretto, and K. M. Poduska. Structural differences in archaeologically relevant calcite. Analytical Methods, 7(21):9304–9309, 2015.

[20] B. Xu, M. B. Toffolo, E. Boaretto, and K. M. Poduska. Assessing local and long-range structural disorder in aggregate-free lime binders. Industrial and Engineering Chemistry Research, 55(30): 8334–8340, 2016.

[21] B. Xu, A. Hirsch, L. Kronik, and K. M. Poduska. Vibrational properties of isotopically enriched materials: the case of calcite. RSC Advances, 8(59):33985–33992, 2018.

[22] Y. Zhu, N. Ma, W. Jin, S. Wu, and C. Sun. Genomic and transcriptomic insights into calcium carbonate biomineralization by marine actinobacterium Brevibacterium linens BS258. Frontiers in Microbiology, 8:602, 2017.

Chapter 4

Photoacoustic detection of weak absorption bands in infrared spectra of calcite

This chapter was published as S. Campbell, M. Dusseault, B. Xu, K. H. Michaelian, and K. M. Poduska. Photoacoustic detection of weak absorption bands in infrared spectra of calcite. Applied Spectroscopy, 75(7):795–801, 2021. doi: 10.1177/00037028211009212. PMID: 33783238.

Following discussions with thesis examiners during the defense proceedings, additions, alterations and further clarifications related to this published work are reported in Appendix C.

Co-authorship statement

As the first author, I contributed to the collection of experimental data, data analysis and manuscript development. Additional experimental data collection was done by Ben Xu and Marisa Dusseault. Dr. Kristin M. Poduska and I developed the original manuscript draft. Dr. Kirk H. Michaelian contributed to subsequent manuscript revisions as well as performed the spectral linearization data analysis. All authors contributed to the review and editing that resulted in the final manuscript.

Abstract

Photoacoustic spectroscopic detection of infrared absorption often produces spectra with enhanced intensities for weaker peaks, enabling the detection of features due to overtones and combinations, as well as less-abundant isotopic species. To illustrate this phenomenon, we present and discuss photoacoustic infrared spectra of calcite ($CaCO_3$). We use linearization of rapid-scan spectra, as well as comparing step-scan and rapid-scan spectra, to demonstrate that saturation is not the driving force behind these enhanced intensities. Our results point to a significant knowledge gap, since a theoretical basis for the enhancement of these weak bands has not yet been developed.

4.1 Introduction

In the field of materials characterization, infrared (IR) spectroscopy can be used to assess structural differences in materials based on differences in the fundamental bands, as well as in the overtones, combinations, and isotopic peaks. The latter three band types are generally much weaker than fundamental bands, making it difficult to obtain information regarding all of the desired peak locations and intensities from a single spectrum. In traditional absorption spectroscopy, weak peaks can be intensified by increasing the quantity of sample that is examined, but this may cause the stronger peaks to become saturated. The identification of weak bands is even more problematic when sample quantities are limited. Alternative methods for the acquisition of IR spectra are needed in these circumstances. In this work, we discuss one such alternative method, photoacoustic spectroscopy (PAS), and its application to the mineral calcite ($CaCO_3$).

The PAS variant of Fourier transform IR (FTIR) spectroscopy is based on the detection of thermal waves induced in a sample as it absorbs modulated IR radiation.[12,18,19] PAS is less common than other IR sampling techniques that are based on transmission measurements for samples embedded in alkali halide pellets or solutions, or others based on attenuated total reflectance (ATR) of powders, solutions, or films. Nevertheless, PAS is the preferred option for strongly absorbing solid materials, as well as viscous liquids and semi-solids that may consist of multiple phases, which are not amenable to grinding or are insoluble in common solvents. Furthermore, PAS can enable depth profiling of

layered or inhomogeneous samples, under specialized experimental conditions. The advantage that PAS offers is based on the fact that the modulated IR energy absorbed by a sample within an enclosed cell produces thermal waves, which in turn create corresponding pressure waves in a carrier gas that surrounds the sample. These pressure (acoustic) waves can be detected by a sensitive microphone or cantilever. The signals produced by these transducers are amplified and then processed by the FTIR spectrometer, yielding an absorptive PAS spectrum.

Calcite, the material under investigation in the present work, has been widely studied using FTIR transmission and ATR techniques, but very little by PAS.[5,7,14,20,24] Calcium carbonate polymorphs, including calcite, appear naturally in many instances and are of importance to materials scientists,[9] archaeologists[23] and those who study biomineralization.[4] FTIR spectroscopy offers distinct advantages relative to diffraction-based techniques because calcium carbonate polymorphs can be easily differentiated from each other even when they are poorly crystallized. This is particularly important in the context of biomineralization, wherein newly mineralized tissues typically form from amorphous calcium carbonate, which then crystallize as they mature.[4,9] In archaeological contexts, calcium carbonate can be poorly crystalline when it originates from wood ash or lime plaster binder, but is well-crystallized in the form of limestone.[17,21,23] Thus, the ability to monitor transitions between amorphous and crystalline $CaCO_3$ – as well as intermediate levels of crystallinity – offers great insights with regard to material identification and transformation.

FTIR spectra acquired using different variants (ATR, transmission or PAS) are not identical, even when the spectra are acquired for the same sample. Previous work on strongly absorbing samples has shown that differences in peak widths and shapes are sometimes observed when comparing PAS and transmission FTIR spectra. These differences are often attributed to partial saturation in the PAS spectra; this phenomenon limits maximum intensities while increasing the apparent widths of the strong bands. In these situations, the intensities of weaker bands, such as those arising from combinations and overtones, are enhanced with respect to the more prominent features in the spectrum.

Previous studies, whether experimental or theoretical, have not fully discussed the origins or implications of these differences. In the present context, the accurate analysis of calcium carbonate materials requires the recognition of which differences in the spectra can be attributed to structural

differences within the minerals themselves. If differences occur in spectra due to the use of alternative measurement methods (ATR, PAS, transmission), then there is a risk that these differences could be erroneously attributed to variations or changes in the materials under study. In this way, materials scientists require a solid working knowledge of the characterization methods on which they rely for structural data.

We show here – and cite examples from other work in the literature – that differences in peak widths, shapes, and relative intensities can occur among PAS, ATR, and transmission IR spectra of calcite. This includes a systematic investigation of saturation-related effects in PAS data.

4.2 Methods

We use calcite (analytical grade $CaCO_3$, Merck) as our benchmark material in this study. Calcite has been studied extensively in our laboratory, and shown to give rise to a number of distinct Mid-IR absorption bands, including isotopic (^{12}C, ^{13}C) peaks, combination modes, and overtones. The assignments of these bands are well known.[25] Prior to each measurement, the calcite powder was manually ground using a mortar and pestle for approximately 2 minutes to sharpen the spectral features, as described in detail elsewhere.[2]

All experiments were carried out with Bruker vacuum FTIR spectrometers. Initial PAS measurements used a Bruker IFS 66v/S instrument equipped with a thermal infrared (globar) source and an MTEC 300 microphone-based PAS cell based at the mid-infrared beamline of the Canadian Light Source. More extensive experiments were carried out with a Bruker Vertex 70v spectrometer and a Gasera PA301 cantilever-based cell located at Memorial University. For PAS data collection, a few milligrams of ground powder were loaded directly into an aluminum sample cup that sits inside the PAS cell. Data were collected either under ambient conditions (Memorial) or after the PAS cell was purged with dry helium gas (Canadian Light Source). Carbon black standards (MTEC and Gasera, respectively) were employed to acquire background (reference) spectra. Rapid-scan (continuous scan) and step-scan data were collected with both spectrometers. Rapid-scan spectra were acquired at different frequencies (specified at 15,800 cm^{-1}, the wavenumber of the internal He-Ne laser) ranging from 1.6 kHz to 18.0 kHz. For this range of scan frequencies, the thermal diffusion length of calcite falls in

the 60-20 μm range. The physical sample depth is much larger than this, on the order of millimetres, when using 2-5 mg of sample. The intensity scale is labelled as arbitrary units; sample spectra were ratioed against reference spectra recorded under like conditions.

Transmission and ATR IR spectra were also collected with the Bruker Vertex 70v system. For each ATR measurement, a few milligrams of powder were pressed directly onto the ATR crystal (Bruker Platinum ATR, single reflection diamond, 45 degree incidence angle), and the data were collected under ambient conditions. Assuming an index of refraction $n = 1.6$ for calcite, the resulting effective penetration depth ranges between 1.8 and 18 μm, for 4000 and 400 cm^{-1}, respectively.

Transmission measurements required diluting the sample ($\sim$1:100) with potassium bromide (KBr) to allow sufficient transparency. The calcite-KBr mixture was ground and re-pressed into a 5 mm pellet using a hand press (Pike Technologies) several times before measurement, in order to minimize particle scattering effects that broaden IR peaks.[16] Transmission measurements were carried out under vacuum conditions. The illumination spot is about 4 mm across, and scattering does not increase the heated area. Diluted samples refer only to transmission measurements (using KBr pellets), not ATR or PAS measurements.

4.3 Results

Figure 4.1 compares rapid-scan PAS, ATR and absorption spectra collected for the same calcite powder sample. The weakest peaks in the ATR and absorption spectra (middle and bottom, respectively) are greatly enhanced – relative to the strongest (ν_3) band – in the PAS spectrum. The weak peaks above 1500 cm^{-1} have been attributed to overtones or combinations.[25]. At lower wavenumbers, the ν_2 and ν_4 bands are also intensified in the PAS spectrum. Furthermore, there is a narrow band at 860 cm^{-1} (the ν_2 vibration of the ^{13}C isotopic species) that is resolved from its ^{12}C counterpart at 878 cm^{-1}. For the two tallest peaks, the ν_3 band is a series of 4-5 overlapping peaks. In contrast, the ν_2 band has only one contributor. This helps to explain why the ν_3 band displays a high-frequency shoulder in the PAS spectrum. Thus, the PAS spectrum shows many enhanced weak spectral features that are less evident in the ATR and absorption spectra.

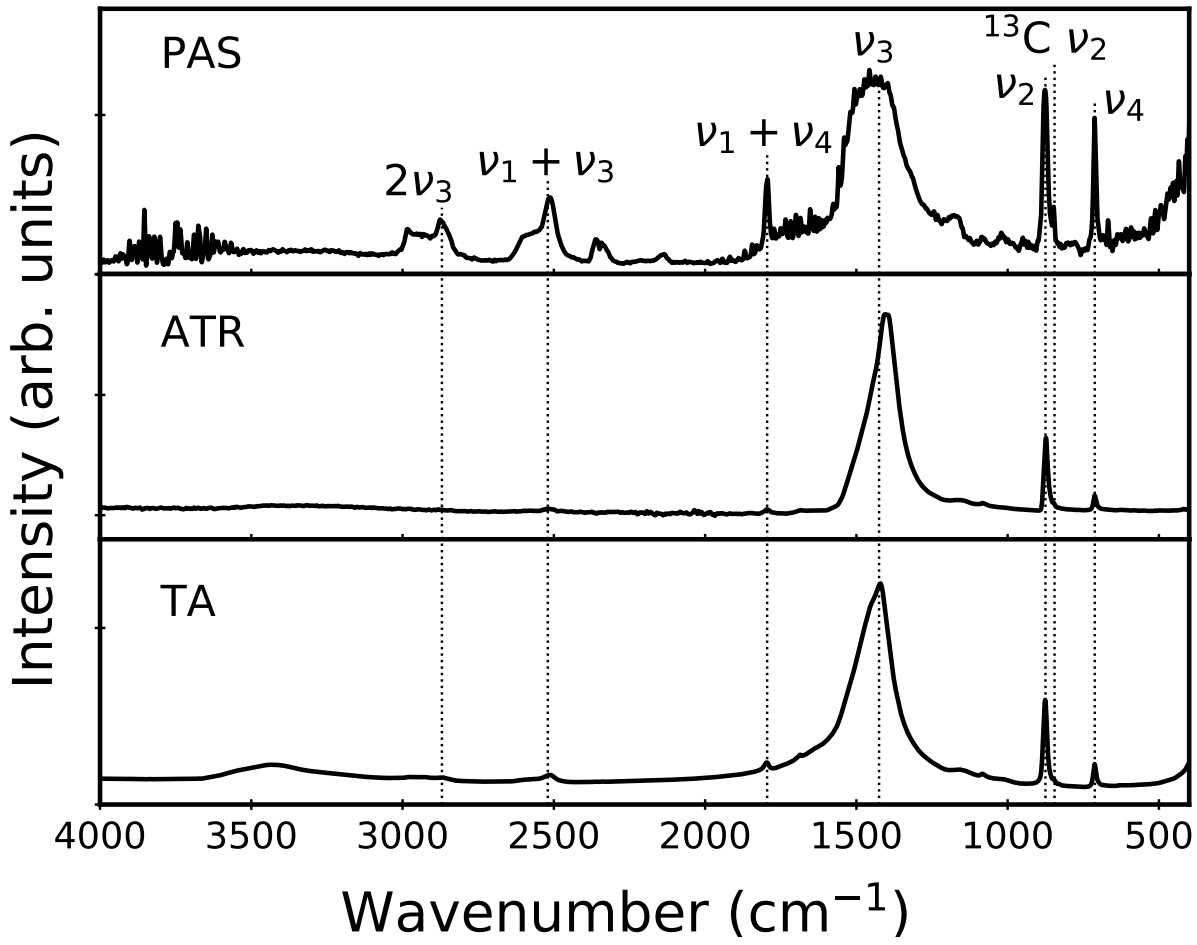

Figure 4.1 Representative FTIR spectra of calcite acquired using three different techniques: PAS (top), ATR (middle), absorption (bottom). Peaks are labelled as fundamentals (ν_2, ν_3 and ν_4), overtone ($2\nu_3$), or combination modes ($\nu_1 + \nu_3$, $\nu_1 + \nu_4$). A fundamental peak for a minority isotopic species (^{13}C ν_2) is also visible.These spectra represent 27 scans for PAS, and 8 scans for ATR and TA.

The intensification of the weak overtone and combination bands in the PAS data is a general result that occurs for many solid materials. Indeed, Natale and Lewis noticed this tendency nearly four decades ago in near-IR PAS data for carbonyl compounds.[13] More recent studies show this effect in Mid-IR PAS data for aromatic hydrocarbons[10,11] and soils.[8] Although this intensification is beneficial for analyzing weak peaks, the effect that causes it is poorly understood. Below, we demonstrate that saturation alone cannot explain the enhancement of the weak peaks in the PAS data. In doing so, we describe how we process the data to eliminate any “artificial" contributions to the data, in accordance with best practices described in the literature.[12]

4.3.1 Linearization of rapid-scan spectra

The striking differences between the PAS data and the ATR and absorption spectra in Figure 4.1 deserve further comment. Given the differences in the overall shape of the strong broad ν_3 band in the PAS data, it is reasonable to suspect some degree of saturation. To investigate this possibility, we compared a series of rapid-scan PAS data at progressively higher scan frequencies ranging from 3.0-18.0 kHz. This experiment relies on the fact that greater scan velocities (modulation frequencies) lead to the reduction – and eventually elimination – of saturation. We note that this series of spectra are adversely affected by cantilever cell resonances at modulation frequencies near 820 and 1640 Hz: these resonances produce nonlinear responses, making some of these spectra unreliable in particular wavenumber regions. We provide a detailed list of the wavenumber ranges we avoided due to the cell resonances – which vary for different scanner velocities (mirror speeds) – as Supplemental Material.

Figure 4.2 displays rapid-scan PA spectra acquired at 3.0, 10.0 and 18.0 kHz. As described above, these frequencies refer to radiation at 15,800 cm^{-1}. In a Michelson interferometer like those used in this work, modulation frequency f (Hz) and wavenumber ν (cm$-$1) are related by $f = 2V\nu$, where V is mirror velocity (cm/s). For the 3.0 kHz spectra discussed in Figures 4.2–4.5, $V = 0.095$ cm/s, and f varies from 76 Hz at 400 cm^{-1} to 760 Hz at 4000 cm^{-1}. The breadth of this frequency range is particularly relevant, since PAS intensity varies approximately as $\frac{1}{f}$.[12] As a consequence, low wavenumber bands such as ν_2 and ν_4 are intensified relative to those at higher wavenumbers in rapid-scan PAS data.

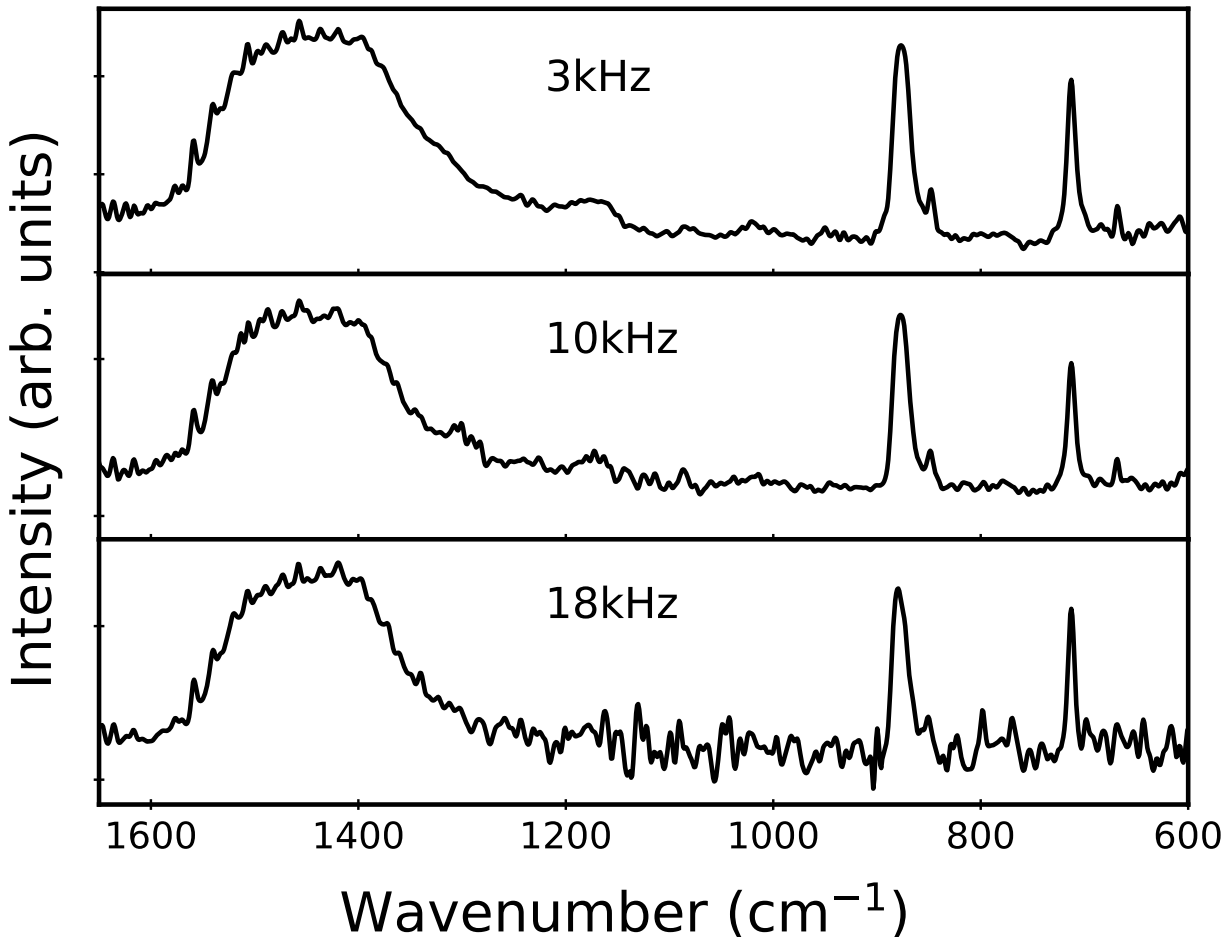

Figure 4.2 Representative rapid-scan PAS data for calcite acquired at 3.0 kHz (top), 10.0 kHz (middle), and 18.0 kHz (bottom) with 2 minute collection time for each. The bottom two spectra show significant noise resulting from the intrinsically weaker spectra at these higher scan frequencies. A wider spectral range for the 3.0 kHz (top) spectrum is provided in Figure 4.3.

Still referring to Figure 4.2, we note that the relative peak intensities of the ν_2 band (878 cm^{-1}) and the ν_3 band (centred near 1450 cm^{-1}) are nearly the same in all three spectra. If the ν_3 band were saturated at lower frequencies, the ν_2/ν_3 intensity ratio would decrease at higher frequencies. The fact that this trend does not occur suggests that the ν_3 band is not saturated to a significant extent in these spectra. Further comparisons of peak heights and widths, in table form, are provided as Supplemental Material.

To make our case for the lack of saturation more quantitative, we linearize the rapid-scan PAS data. This calculation produces spectra that are linear over one or more orders of magnitude of absorption intensity; put simply, this reduces saturation effects in PAS data.[12] In conventional PAS data treatment, a single-channel spectrum from the sample is divided by a carbon black spectrum acquired under like conditions. In contrast, linearization uses a numerical method developed a number of years ago by Burggraf and Leyden[1] that has been used effectively in several PAS studies.[3,15] The linearization calculation utilizes amplitude and phase information for both sample and reference. The procedure uses real and imaginary spectra derived from Fourier transformation of the two interferograms, rather than the more common Mertz phase correction. We emphasize that linearization can correct for intensity saturation effects, but it does not compensate for lineshape differences that occur between PAS and transmission IR spectra.

Figure 4.3 compares linearized and conventional PAS data for calcite. The spectra are quite similar. There is some narrowing of the broad ν_3 band in the linearized spectrum, but only slight changes in the relative peak intensities. Because of the similarities between the conventional and linearized PAS data, there is little reason to suspect that saturation measurably affects the calcite PAS data reported in this work. This conclusion is consistent with the fact that different rapid-scan modulation frequencies also show very little change in relative peak intensities, even at the highest scan velocities.

4.3.2 Step-scan vs. rapid-scan spectra

A cleaner way to avoid saturation effects is to perform a different FTIR experiment that uses step-scan mirror movement. In step-scan (step-and-integrate) spectroscopy, the incident radiation is modulated either by chopping the IR beam (amplitude modulation) or by dithering the mirror at each resting

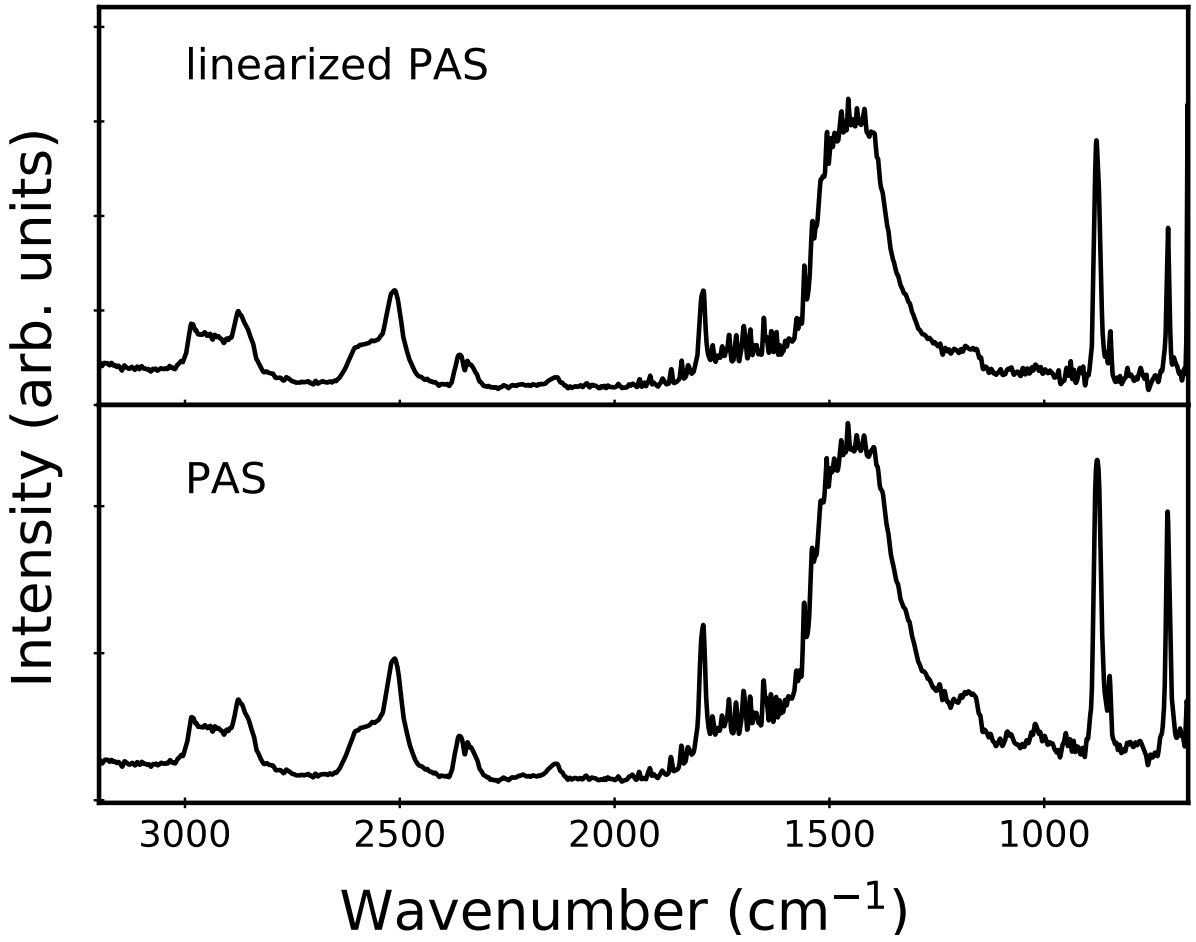

Figure 4.3 Comparison of linearized (top) and standard (bottom) rapid-scan PAS data for calcite, recorded at 3.0 kHz for 27 scans. The intensity scales are different due to the calculation details in the two methods, so we report the intensities in arbitrary units and comment only on relative peak intensity changes.

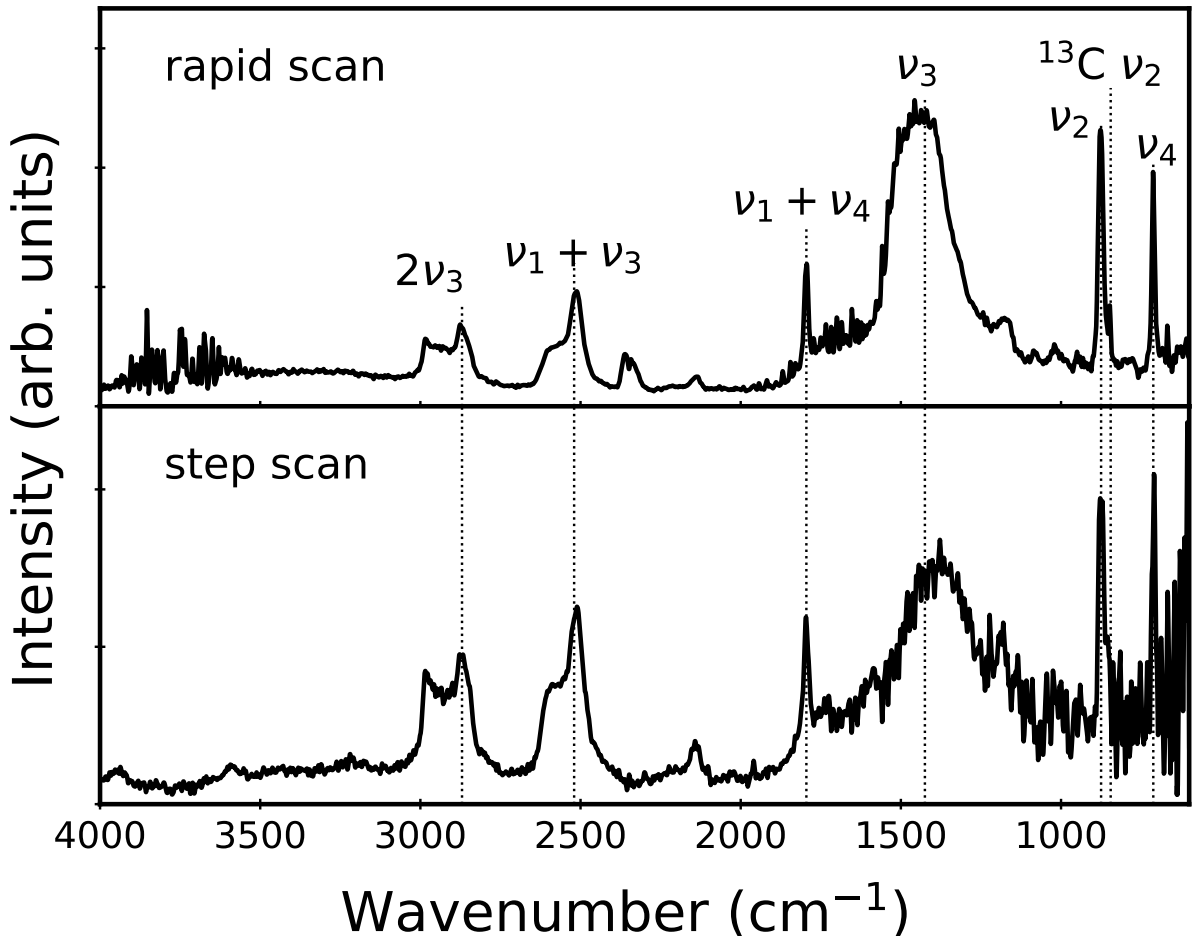

Figure 4.4 Comparison of rapid-scan (top) and step-scan (bottom) PAS data for calcite. The rapid-scan spectrum was obtained at 1.6 kHz for 27 scans, while the step-scan spectrum was acquired using phase modulation at 227 Hz and a modulation amplitude of 2λ (λ = 633 nm) for 64 scans

.

position (phase modulation). Amplitude modulation with a chopper modulates the entire spectrum at a single frequency, but half of the incident intensity is blocked by the chopper blade. Our experiments employed phase modulation thereby utilizing all of the available incident intensity. Nevertheless, both strategies ensure that all PAS data are collected at a single frequency, and eliminate the low-wavenumber bias of the rapid-scan spectra.

Figure 4.4 compares representative step-scan and rapid-scan PAS data for calcite. Band intensities above 2000 cm^{-1} are significantly increased in the step-scan spectrum, as expected. We note that the intensity in this kind of phase modulation spectrum is proportional to a first-order Bessel function,

which rises from zero at 0 cm^{-1} to a maximum whose location varies with modulation amplitude and frequency. A representative example of this effect is provided as Supplemental Material. The Bessel function profile therefore reduces band intensities at low wavenumbers.[12] However, this affects both sample and reference, so it is largely eliminated when the calcite spectrum is ratioed against the carbon black reference spectrum. Any difference in modulation frequency between the two spectra contributes to the relative intensity reduction for the ν_2, ν_3 and ν_4 bands in the step-scan spectrum. What is very significant for the discussion here is that, even though there are some inherent differences, both the step-scan and rapid-scan PAS data show enhancement of the weak peaks at higher wavenumbers.

4.3.3 Transducer effects

The relative peak intensities in PAS data for calcite samples are not affected by transducer type (cantilever vs. microphone) nor by repacking the powdered sample used for the measurement. Figure 4.5 shows illustrative data that support this assertion. The top and middle spectra compare the same calcite powder, loaded in the sample cup and packed on different days. The similarity in the resulting spectra is consistent with earlier reports that show PAS data are usually insensitive to the amount of solid, likely because the penetration depth limits how much of the material is probed.[12] For the bottom panel of Figure 4.5, a spectrum collected with a microphone-based transducer is virtually identical to the cantilever-based spectra shown above it. We note that all PAS data in Figures 4.1-4.4 were collected with a cantilever-based cell.

4.4 Discussion

Our experiments and subsequent analyses, as laid out above, do not point to a reasonable cause for enhanced weak peaks in PAS data for calcite. These effects are not associated solely with either rapid-scan or step-scan data. We demonstrate that our sample is substantially thicker than the optical penetration depth or thermal diffusion length. We compare two different kinds of transducers, and find no clues there. Finally, we present a large number of comparisons (including different mirror speeds, collection times, and linearization corrections) that show that the intensity enhancements are

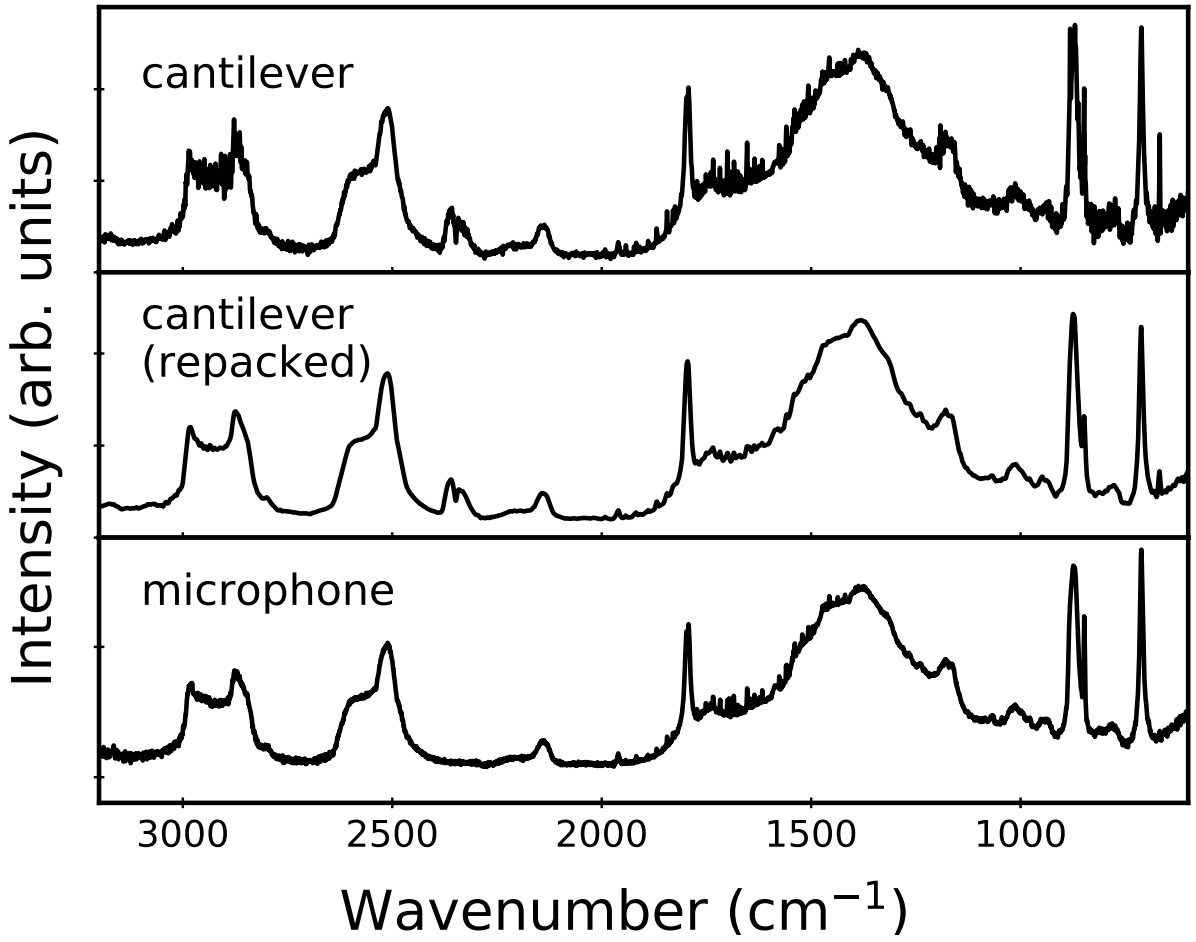

Figure 4.5 Representative rapid-scan PAS data for calcite that compare: cantilever transducer (top), cantilever transducer with repacked sample (middle), microphone transducer (bottom). These spectra represent 8, 32, and 512 scans, respectively.

not consistent with saturation effects.

Existing theories do not help us understand these intensity enhancements. Transmission IR data for calcite have been simulated by many groups using quantum chemical density-functional theory calculations.[6,16,22,25] In these instances, calculations provide energy values for the fundamental vibrational modes, and the IR spectra are then simulated based on initial user-specified broadening parameters and intensities. Relative changes in peak widths and intensities are qualitatively meaningful, but all are based on initial user-specified input, which is based on experimental trends. In this way, the IR peak intensities are not calculated from first principles in the same way that the energies of the vibrational modes are calculated. Furthermore, there are always discrepancies between the calculated and experimentally observed band energies due to anharmonicity. We are not aware of any PAS-specific calculations or simulations for IR spectra of solids.

4.5 Conclusions

PAS spectra show persistent, repeatable enhancement of weak peaks due to combination modes, overtones and isotopic species in calcite relative to transmission and ATR spectra of this material. We have shown that this enhancement is intrinsic to the detection method (PAS) and note that an adequate theoretical explanation for this long-standing phenomenon has not yet been developed.

Bibliography

[1] L. Burggraf and D. Leyden. Quantitative photoacoustic spectroscopy of intensely light-scattering thermally thick samples. Analytical Chemistry, 53(6):759–764, 1981.

[2] S. Campbell and K. M. Poduska. Incorporating far-infrared data into carbonate mineral analyses. Minerals, 10(7):628, 2020. doi: 10.3390/min10070628.

[3] R. Carter III. The application of linear PA/FT-IR to polymer-related problems. Applied Spectroscopy, 46(2):219–224, 1992.

[4] A. Gal, K. Kahil, N. Vidavsky, R. T. DeVol, P. U. P. A. Gilbert, P. Fratzl, S. Weiner, and L. Addadi. Particle accretion mechanism underlies biological crystal growth from an amorphous precursor phase. Advanced Functional Materials, 24(34):5420–5426, 2014. doi: 10.1002/adfm.201400676.

[5] O. Gómez, P. Quintana, D. Aguilar, J. Alvarado-Gil, M. Yánez-Limón, L. Diaz, and D. Aldana. Photothermal characterization of materials biomineralized by mollusks. Review of Scientific Instruments, 74(1):750–754, 2003.

[6] R. Gueta, A. Natan, L. Addadi, S. Weiner, K. Refson, and L. Kronik. Local atomic order and infrared spectra of biogenic calcite. Angewandte Chemie International Edition, 46(1-2):291–294, Jan. 2007. ISSN 1521-3773. doi: 10.1002/anie.200603327.

[7] N. Guskos, G. Papadopoulos, J. Majszczyk, J. Typek, J. Rybicki, A. Guskos, I. Kruk, K. Aidinis, and G. Zolnierkiewicz. Photoacoustic response of sea urchin tissue. Reviews on Advanced Materials Science, 23:76–79, 2010.

[8] P. K. Krivoshein, D. S. Volkov, O. B. Rogova, and M. A. Proskurnin. FTIR photoacoustic spectroscopy for identification and assessment of soil components: chernozems and their size fractions. Photoacoustics, 18:100162, 2020.

[9] F. C. Meldrum and H. Cölfen. Controlling mineral morphologies and structures in biological and synthetic systems. Chemical Reviews, 108(11):4332–4432, 2008. doi: 10.1021/cr8002856.

[10] K. Michaelian, Q. Wen, B. Billinghurst, J. Shaw, and V. Lastovka. Far-and mid-infrared photoacoustic spectra of tetracene, pentacene, perylene and pyrene. Vibrational Spectroscopy, 58: 50–56, 2012.

[11] K. Michaelian, S. Oladepo, J. Shaw, X. Liu, D. Bégué, and I. Baraille. Raman and photoacoustic infrared spectra of fluorene derivatives: Experiment and calculations. Vibrational Spectroscopy, 74:33–46, 2014.

[12] K. H. Michaelian. Photoacoustic IR Spectroscopy: Instrumentation, Applications and Data Analysis. Wiley-VCH, 2010.

[13] M. Natale and L. N. Lewis. Application of PAS for the investigation of overtones and combinations in the near IR. Applied Spectroscopy, 36(4):410–413, 1982.

[14] G. Norton and J. McClelland. Rapid determination of limestone using photoacoustic spectroscopy. Minerals Engineering, 10(2):237–240, 1997.

[15] A. Pichler and M. G. Sowa. Using the linearization approach for synchronizing the phase of photoacoustic reference and sample data. Applied Spectroscopy, 58(10):1228–1235, 2004.

[16] K. M. Poduska, L. Regev, E. Boaretto, L. Addadi, S. Weiner, L. Kronik, and S. Curtarolo. Decoupling local disorder and optical effects in infrared spectra: Differentiating between calcites with different origins. Advanced Materials, 23(4):550–554, 2011. ISSN 1521-4095. doi: 10.1002/adma.201003890.

[17] L. Regev, K. M. Poduska, L. Addadi, S. Weiner, and E. Boaretto. Distinguishing between calcites formed by different mechanisms using infrared spectrometry: archaeological applications. Journal of Archaeological Science, 37(12):3022–3029, 2010.

[18] A. Rosencwaig. Photoacoustics and Photoacoustic Spectroscopy. Wiley, 1980.

[19] A. Rosencwaig and A. Gersho. Theory of the photoacoustic effect with solids. Journal of Applied Physics, 47:64–69, Jan. 1976. doi: 10.1063/1.322296.

[20] M. M. Thompson and R. A. Palmer. In situ fourier transform infrared diffuse reflectance and photoacoustic spectroscopy characterization of sulfur-oxygen species resulting from the reaction of SO_2 with $CaCO_3$. Applied Spectroscopy, 42(6):945–951, 1988.

[21] M. B. Toffolo and E. Boaretto. Nucleation of aragonite upon carbonation of calcium oxide and calcium hydroxide at ambient temperatures and pressures: a new indicator of fire-related human activities. Journal of Archaeological Science, 49:237–248, 2014.

[22] L. Valenzano, Y. Noel, R. Orlando, C. Zicovich-Wilson, M. Ferrero, and R. Dovesi. Ab initio vibrational spectra and dielectric properties of carbonates: magnesite, calcite and dolomite. Theoretical Chemistry Accounts, 117(5-6):991–1000, 2007. URL `https://tutorials.crystalsolutions.eu/index.html`.

[23] S. Weiner. Microarchaeology: Beyond the Visible Archaeological Record. Cambridge University Press, 2010.

[24] E. Wentrup-Byrne, L. Rintoul, J. Smith, and P. Fredericks. Comparison of vibrational spectroscopic techniques for the characterization of human gallstones. Applied Spectroscopy, 49(7): 1028–1036, 1995.

[25] B. Xu, A. Hirsch, L. Kronik, and K. M. Poduska. Vibrational properties of isotopically enriched materials: the case of calcite. RSC Advances, 8(59):33985–33992, 2018.

Acknowledgements

This work was supported by the Natural Sciences and Engineering Research Council (Canada) [grant number 2018-04888]. We thank F. Borondics, T. May, and X. Lu from the Mid-IR beamline at the Canadian Light Source.

Figure	Spectrum	Number of scans
1	PAS	27
	ATR	8
	TA	8
2	3.0 kHz	27
	10.0 kHz	89
	18.0 kHz	160
3	PAS	27
4	rapid scan	27
5	cantilever	8
	cantilever (repacked)	32
	microphone	512

Table 4.1 Number of scans averaged in each spectrum reported in Figures in the main text.

Conflicts of Interest

The Authors declare that there is no conflict of interest.

4.6 Supplemental Materials

4.6.1 Scan numbers

The data presented in the paper represent experiments using different transducer types and measurement geometries. As such, the number of scans averaged for each spectrum varied. Table 4.1 summarizes the number of scans averaged in each spectrum reported in the main text.

4.6.2 Cell resonance details

The Gasera PA301 photoacoustic cell is known to have resonance responses at specific modulation frequencies. Figure 4.6 highlights the effect on carbon black.

The intrinsic resonances of the Gasera PA301 cell can be problematic depending on the position of the spectral bands of interest to the experimenter. The fundamental bands of Calcite (ν_2, ν_3 and, ν_4) fall between 1500 - 700 cm^{-1}. We found that analysis of these (an other weaker) bands became unreasonable when the cell resonance fell close to this range, even with spectra ratioed against reference carbon black. To calculate the position of a resonance in wavenumbers, multiply the He-Ne laser

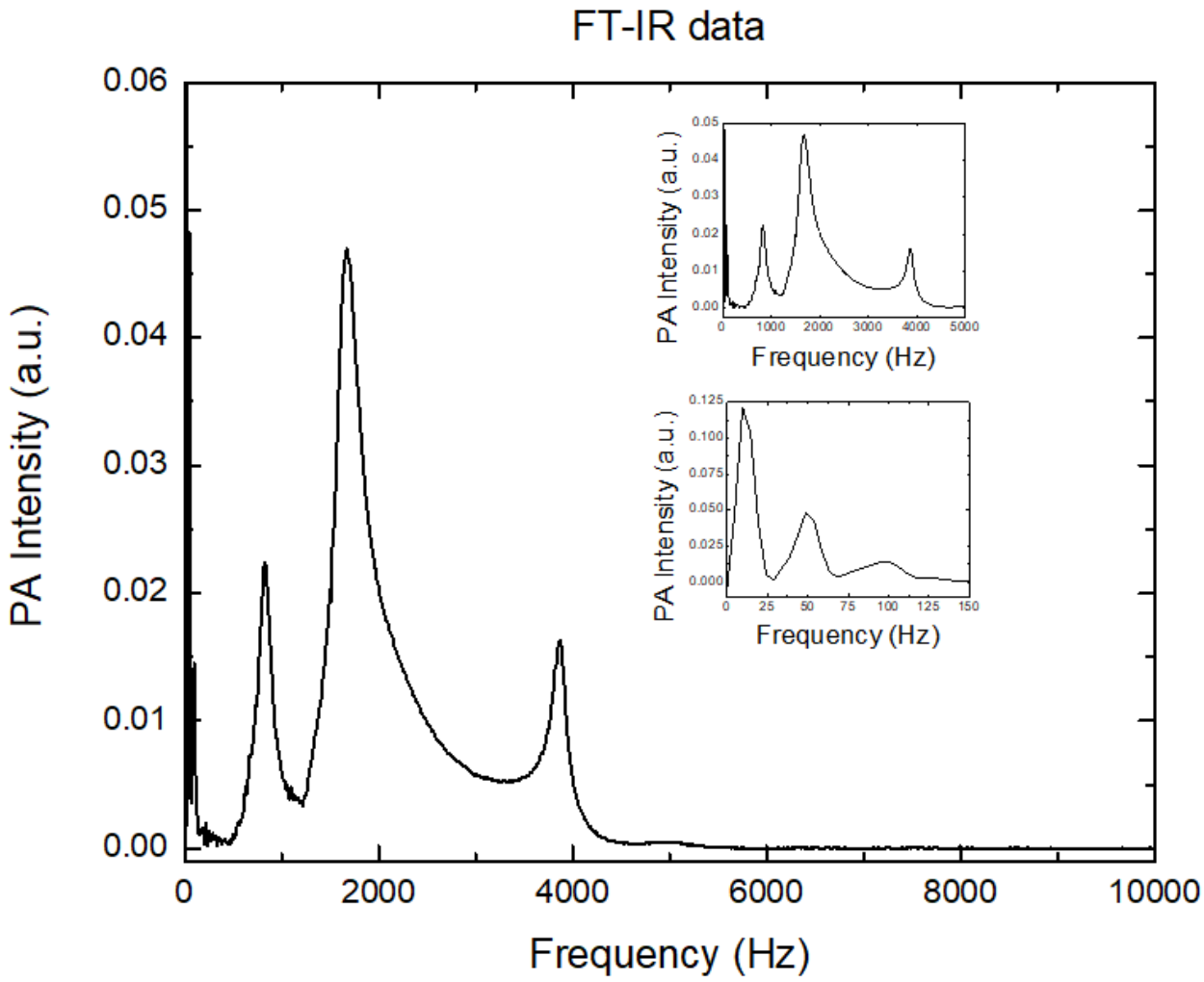

Figure 4.6 Photoacoustic data for carbon black (intensity vs. modulation frequency) collected using a IFS 66 FT-IR system and a Gasera PA301 detector. Peaks of high intensity near 820 Hz, 1640 Hz and 3900 Hz are intrinsic cell resonances and should be avoided where possible.

Table 4.2 Locations of the Gasera PA301 cell resonances in wavenumbers for a given scan frequency. Higher scan frequencies place the location of these resonances near, and in some cases directly on, the calcite spectral peaks.

Scan frequency	820 Hz Resonance position (cm^{-1})	1640 Hz
3.0 kHz	4319	8637
5.0 kHz	2591	5182
7.0 kHz	1851	3702
9.0 kHz	1440	2879
10.0 kHz	1296	2591
11.0 kHz	1178	2356
13.0 kHz	997	1993
15.0 kHz	864	1727
18.0 kHz	720	1440

wavenumber (15800 cm^{-1}) by the ratio of modulation (resonance) frequency to scan frequency:

$$k[\mathrm{cm}^{-1}] = 15800\ \mathrm{cm}^{-1}\,\frac{f_{modulation}}{f_{scan}}. \tag{4.1}$$

For ease, we summarize the positions of the first two Gasera cell resonances (820 Hz and 1640 Hz) in Table 4.2.

4.6.3 Additional details about the linearization calculations

The thermal diffusion constants a_s and a_r are equal to the reciprocals of the thermal diffusion lengths of the sample s and reference r, respectively. The thermal diffusion length for the sample is given by $\mu_s = (\alpha/\pi \mathrm{f})^{\frac{1}{2}} = 1/a_s$ where α is the thermal diffusivity (mm^2/s) and f is frequency. Hence μ_s and a_s are frequency dependent. The relation between the linearized amplitude spectrum q_l and the normalized amplitude spectrum q_n is $q_l = 2^{1/2}\ \mathrm{q}_n/\sin(\psi – \pi/4)$ where ψ is the phase lag due to thermal propagation in the sample. The modulation frequency f affects both sample and reference spectra, and its effect is cancelled when these are ratioed to calculate q_n. Four references are cited in the main text that provide the context and details behind this linearization calculation.[1,3,12,15]

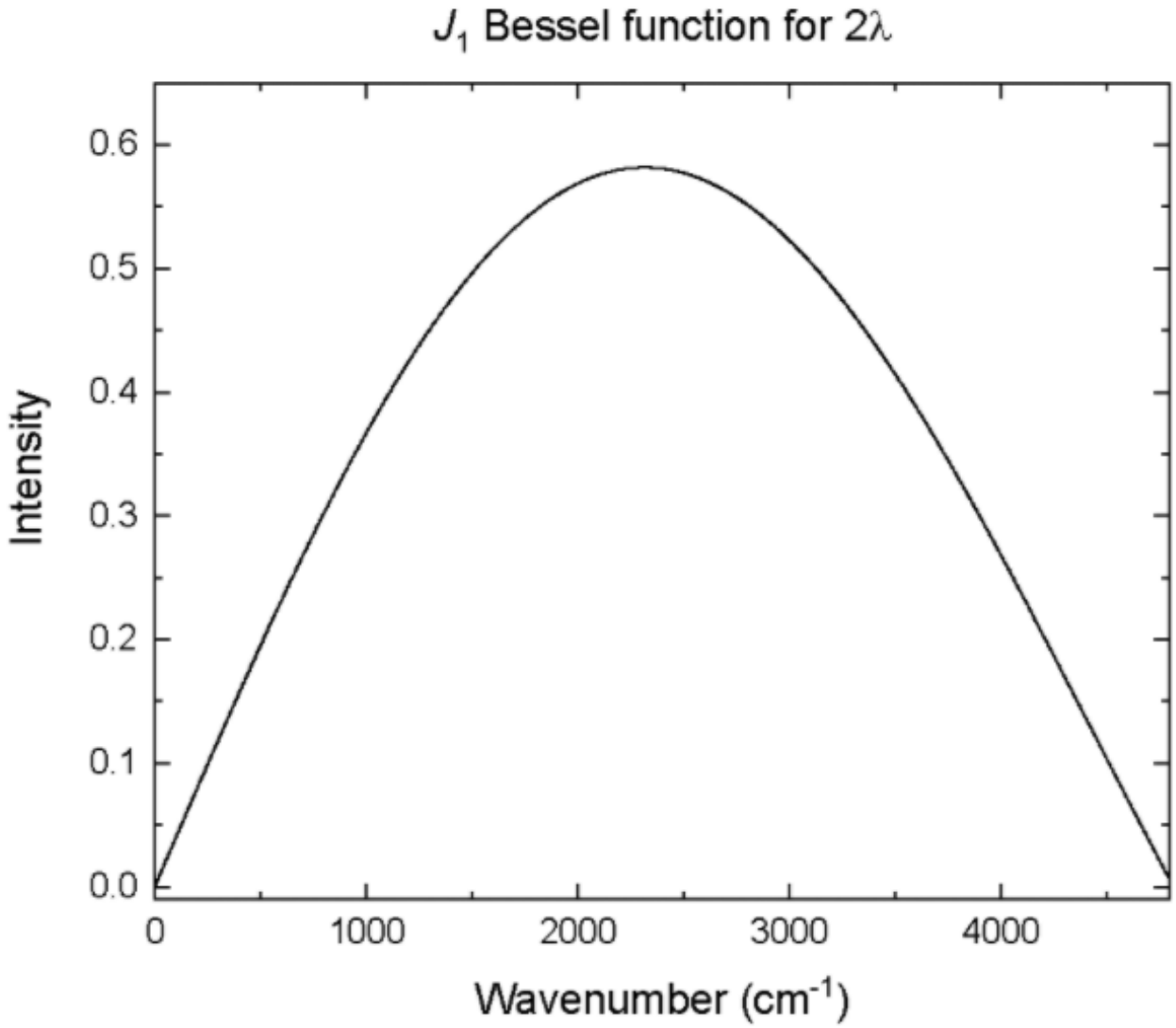

Figure 4.7 Bessel function J_1 for 2λ

Peak height comparisons for rapid-scans (840 - 891 cm^{-1} region, 2 minute scans, from Figure 2

	^{13}C		^{12}C		
Scan Frequency (kHz)	Position (cm^{-1})	**Peak height**	Position (cm^{-1})	**Peak height**	Peak height ratio
3.0	847.9	.017	876.4	.088	.20
9.0	848.7	.020	877.3	.104	.19
10.0	848.8	.017	877.1	.104	.17
16.0*	850.1	.035	877.7	.103	.34
18.0	850.8	.023	879.7	.102	.22

Peak width comparisons for rapid-scans (840 - 891 cm^{-1} region, 2 minute scans, from Figure 2

	^{13}C		^{12}C		
Scan Frequency (kHz)	Position (cm^{-1})	**Width (cm^{-1})**	Position (cm^{-1})	**Width (cm^{-1})**	Peak width ratio
3.0	847.9	9	876.4	18	.50
9.0	848.7	9	877.3	17	.53
10.0	848.8	9	877.1	18	.50
16.0*	850.1	8	877.7	16	.50
18.0	850.8	10	879.7	18	.55

Table 4.3 Comparison of peak heights and widths as a function of scan velocity. * indicates that the spectrum is severely affected by cell resonance effects at this scan frequency

4.6.4 Step-scan phase modulation

To a good approximation, the phase modulation spectrum is equal to $B(\nu)|[J_1(2\pi\nu\varepsilon)]|$ where $B(\nu)$ is the energy density at wavenumber ν (in other words, the empty-instrument energy curve); J_1 is the Bessel function, ε is the modulation amplitude. Figure 4.7 shows this function from 0 cm^{-1} to 4800 cm^{-1}.

4.6.5 Peak height and width comparisons

We provide Table 4.3 that compare selected peak heights and widths for rapid scan that are shown in Figure 2 of the main text. With these data we show that there is a consistent ratio of the weak ^{13}C ν_2 peak near 850 cm^{-1} to the strong ^{12}C ν_2 near 877 cm^{-1} across the range of scan frequencies. Furthermore, there is no significant change in the relative widths as a function of scan frequency.

Chapter 5

Molecular dynamics simulations of aragonite vibrational mode energies

Authorship statement

The work described in this chapter was done in collaboration with Dr. Ivan Saika-Voivod, Dr. Shahrazad Malek, and Dr. Kristin Poduska. Initial implementation of the force field parameters in GROMACS was done by Dr. Malek and me, with input from Dr. Saika-Voivod, using the original work published by Xiao *et al.*[21] This current work makes use of supplemental files made available by Cruz-Chu *et al.*, which are an updated version of the parameters published by Xiao *et al.*[7,21] Data analysis, interpretation and writing were done by me with comments and feedback from Drs. Saika-Voivod, Malek and Poduska.

5.1 How computational modeling complements our experimental data

Computational methods allow materials scientists to study physical systems in a virtual lab environment. This enables the investigators to have fine control over the virtual experiments in a way that,

in a laboratory setting, would be extremely challenging at best or impossible at worst. Previous computational works using quantum chemical density-functional theory have investigated the vibrational modes of calcium carbonate, but those investigations were primarily limited to the internal vibrational modes.[10,16,18,22] This is because the external modes of calcite show significant dispersion compared to the internal carbonate modes and because a large supercell is required to support external vibrational modes.[10]

Previous investigators have successfully examined pure and doped silica's internal and external vibrational modes using molecular dynamics (MD) simulations to calculate a theoretical vibrational density of states (VDOS).[9] That work serves as a proof-of-concept to employ those same methods to generate VDOS plots for calcium carbonate materials. This chapter develops a workflow to generate multiple comparative VDOS plots for aragonite, a calcium carbonate polymorph.

The vibrational density of states (VDOS), sometimes referred to as the phonon density of states, is an important characteristic of a solid system that gives information about the optical and thermodynamical properties of the system.[8] A VDOS is a count of the vibrational modes and their given energies over the energy range of interest for a specific material. Plotting the VDOS as a histogram (number of modes per given energy), we see a dataset similar to an infrared (IR) spectrum. It is important to note that a VDOS and an IR spectrum for the same material are not equivalent. An IR spectrum indicates the photon energies, typically in wavenumbers (cm^{-1}), that were absorbed (or transmitted) by the sample. All peaks present in the IR spectrum will exist in the VDOS but not vice-versa. This is because the VDOS encompasses all possible vibrational modes of the system. In contrast, the IR spectrum over the same energy region will only show the vibrational modes that exhibit a permanent dipole moment, a requirement to be IR active. To experimentally examine the IR inactive modes, one must use an alternate technique, such as Raman spectroscopy, where the selection rules differ. Further, while it may be tempting to compare band intensities between a VDOS and experimental IR spectrum, it is crucial to understand that generating a VDOS plot does not consider anything related to photon-vibrational mode interactions that influence IR band intensities. In this way, the VDOS can identify where the bands should be but gives no information about relative intensities.

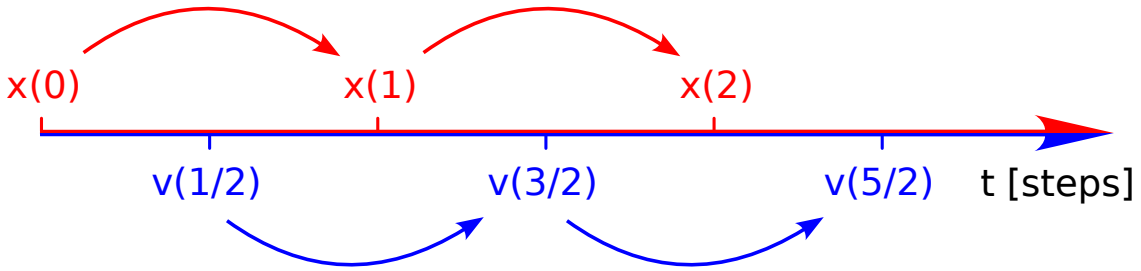

Figure 5.1 Schematic of leap-frog integration method. The positions and velocities of the particles are updated at staggered timesteps, which results in the system energy being conserved.

5.2 Calculations

MD simulations at the barest level involve solving Newton's equations of motion for a many-body system. Additional algorithms are added to account for bonds, atomic charges, temperature, and pressure. By defining a lattice structure, the interaction potentials for the constituent atoms (or molecules), and integrating over time, we can examine the evolution of a virtual calcium carbonate sample and extract relevant information related to the material properties. In our case, we seek to examine the vibrational modes of the system via a VDOS plot.

Our MD simulations use a leap-frog (Verlet) integrator to advance the simulation. This method is used because it is simple, time-reversible, and symplectic.[4] It calculates the velocity and position of the particles (atoms) at staggered points in time.[3] We get the acceleration from the sum of the forces acting on the atom, update the velocity using the acceleration, and then update the position using the velocity. This is summarized visually in Figure 5.1

This work makes use of GROMACS, a molecular dynamics software suite that solves Newton's equations of motion for systems involving many particles (hundreds to millions).[1,2,11,14,15,17,19] GROMACS solves Newton's equations of motion by incorporating essential molecule physics such as temperature, pressure, and electrostatic interactions, for all atoms defined in the input files, into the determination of net force acting on each atom. Following the initial simulation steps necessary to equilibrate the system (*i.e.*, reach a steady state), the atomic coordinates are updated at successive time steps and recorded as the system's trajectory. Details related to the initial setup are the subject of the following sections. The trajectory is a source of successive snapshots of the simulation, which are used as input configurations in the normal mode analysis. The VDOS plot is generated by averaging

the normal modes calculated from these snapshots.

For this work, the ultimate goal is to examine the bulk material properties of aragonite, specifically the vibrational modes and how defects influence them in the material. Regarding CPU cycles, simulating a crystal large enough to be considered bulk would be very computationally expensive. Each integration time step requires, at minimum, a calculation of the forces on each particle, a new particle velocity based on the net force, followed by a new position based on that velocity. As the number of particles increases, so does the number of calculations for particle forces. Rather than attempting to simulate a number of particles on the order of Avogadro's number (10^{23}), these calculations are performed using periodic boundary conditions to reduce the computational load. In this way, the simulation cell is functionally replicated in all directions out to infinity, creating a crystal of infinite size representing the bulk material and eliminating surface effects that may distort the results. A simulation cell of appropriate size is necessary so as not to introduce computational artifacts related to these periodic boundaries.

The first goal for a new simulation is to equilibrate the aragonite lattice to the desired temperature of 300 K and pressure of 1 bar. Specific details related to this process are discussed in greater detail in the following sections. Equilibrium is reached when the system remains stable at these values for a reasonable amount of timesteps. Equilibration is done in three distinct phases; energy minimization, a short run at constant **n**umber of particles, **v**olume and **t**emperature (**NVT**), and finally another short run at constant **n**umber of particles, **p**ressure and temperature (**NPT**). From there, the system can evolve according to the operating parameters outlined in the simulation input files. This includes the interaction potentials defined in the chosen force-field from Xiao *et al.*[7,21] The VDOS is built from an average of many simulations. By allowing the system to run for a sufficient amount of time following equilibration, successive configurations from the trajectory can be used in the normal mode analysis to get meaningful statistics for the VDOS. The general characteristics of the system are not expected to change with time once the system has been equilibrated.

The GROMACS software suite requires three files to begin the simulation. The first required file, a conformation file, assigns a number to each atom, describes the initial positions in X, Y, and Z coordinates, and defines the initial dimensions of the box used to contain the simulation. The topology file

describes the type of particles used in the system, associates them with an atom, and describes how they interact within the system through bonded or non-bonded interactions, constraints, and exclusion rules. The total number of each particle in the system is also specified in the topology file. The final required file, the **m**olecular **d**ynamics **p**arameter (MDP) file, is where all the remaining simulation parameters are defined, such as the integrator, time step, additional algorithms for temperature, pressure, electrostatics, and the output settings.

Using the Xiao *et al.* force-field[21], the system consists of a collection of atoms with bonds defined by improper dihedral angles, so all interactions are considered non-bonded. Cruz-Chu *et al.* modified the Xiao *et al.* force-field to include a spring-bond between the carbon and oxygen atoms of the carbonate units.[7] This modification to the force field does not change how the simulations are executed, only their respective outputs.

5.2.1 Energy minimization

The first step, typical in any MD simulation, is the energy minimization of the system. Energy minimization is repeated after the production run, before the normal mode analysis. The simulation begins with a 125-unit cell (5x5x5) aragonite slab generated using the supplemental files provided by Cruz-Chu *et al.* and the program VMD (see Figure 5.2).[7,12] The objective is to get the structure to an energy minimum before bringing it to the desired temperature (300K) and pressure (1 bar). The choice of these values is two-fold: it is more-or-less ambient temperature and pressure and matches the original parameters used by the authors that developed the force field.[7,21]

After performing the energy minimization, a visual check is made to verify that the energy minimum has been reached by examining the potential energy as a function of time in the simulation. This uses an integrated GROMACS software tool, *energy*. This tool allows the user to examine many system properties, such as, but not limited to, the pressure, volume, temperature, potential energy, or kinetic energy. Figure 5.3 shows the potential energy of the aragonite system during the energy minimization phase. We expect the system's potential energy to decrease with time until either the minimization algorithm can no longer reduce the energy or the maximum force tolerance, defined in

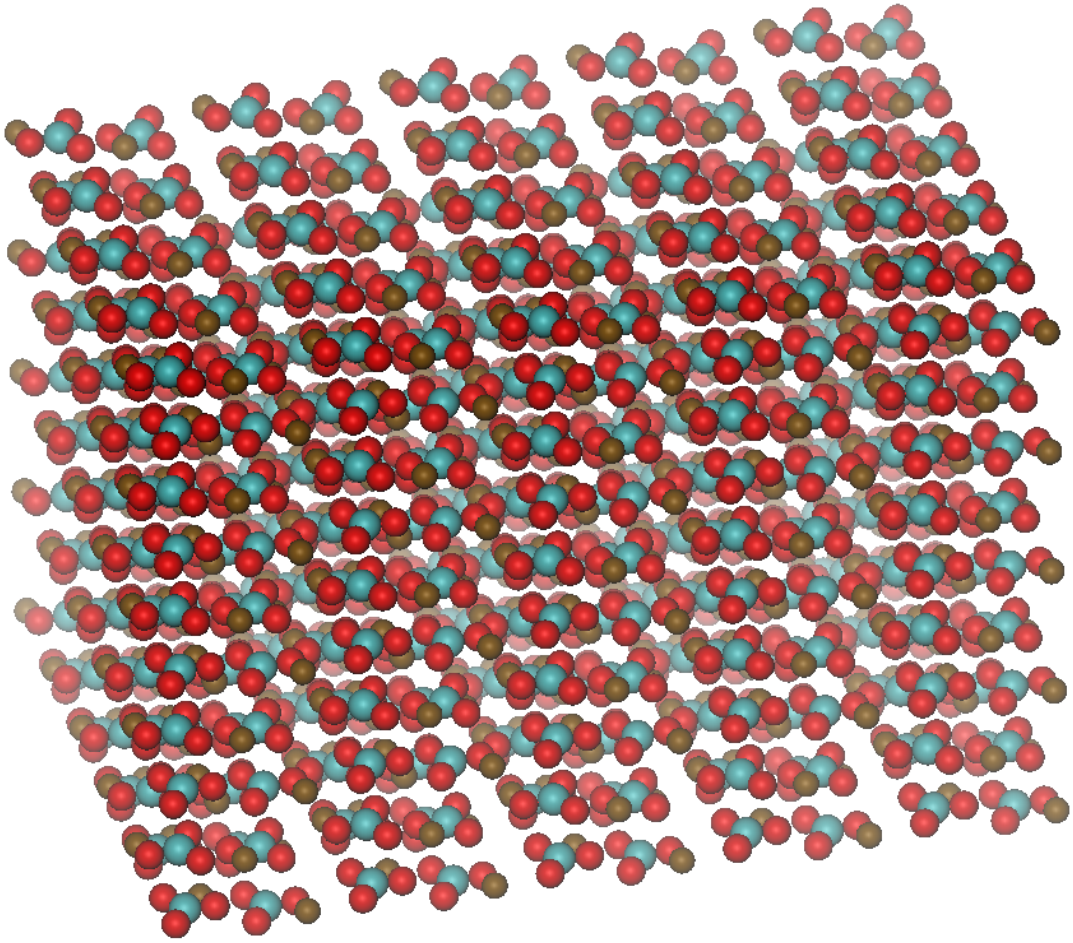

Figure 5.2 Initial configuration of aragonite used as input for GROMACS simulations. The simulation cell includes 125 (5x5x5) aragonite unit cells. Calcium atoms in brown, carbon atoms in teal, and oxygen atoms in red.

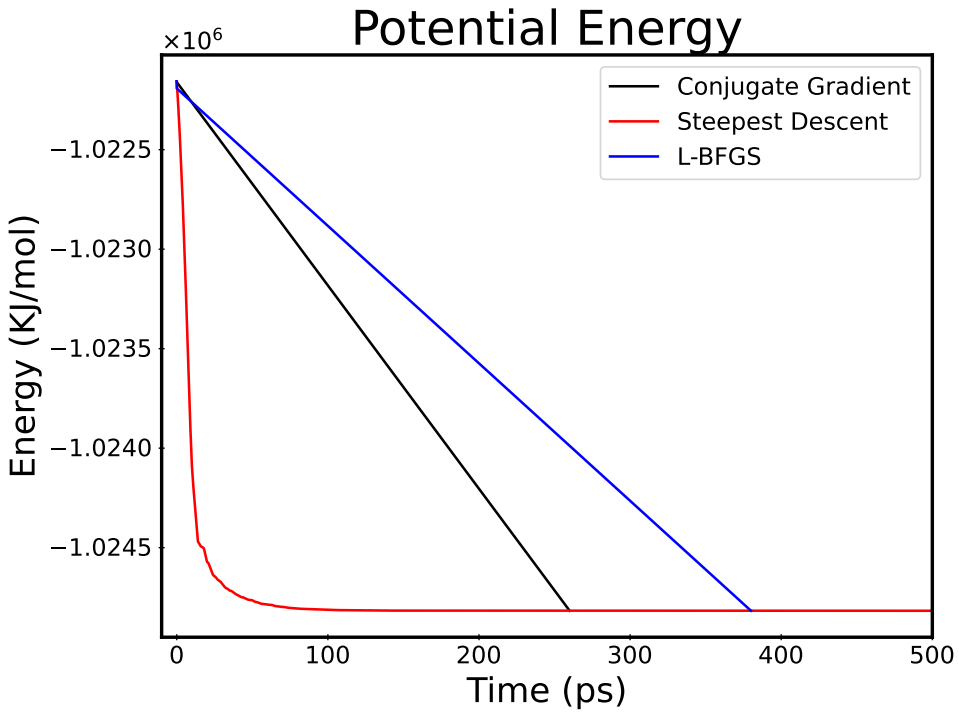

Figure 5.3 The potential energy of the system during energy minimization using the available minimization algorithms: Conjugate Gradient (black), Steepest descent (red), and l-BFGS (blue). All methods converge to the same minimum.

the MDP file as *emtol*, is met. Typical values of *emtol* are suggested to be 0.001 N/mol but will vary with the system simulated. Normal mode analysis requires much more aggressive energy minimization than the initial equilibration. For specific values used in these simulations, the reader is referred to Section B.1 of Appendix B. Figure 5.3 shows the results for all available algorithms: Conjugate Gradient (black), Steepest Descent (red), and limited-memory Broyden-Fletcher-Goldfarb-Shanno quasi-Newtonian minimizer (blue). Each algorithm converges to the same minimum potential energy. We used the conjugate gradient method for production runs since it achieves the minimum in the fewest time steps. Further details on the specifics of the algorithms can be found in the GROMACS documentation.[13]

After the energy minimization, the system is brought to the desired temperature and pressure defined in the MDP file. This is done in two steps to be cautious. The first phase is the NVT run where the simulation is kept at a constant **n**umber of particles, constant **v**olume, and a constant **t**emperature (300 K) using the Berendsen Thermostat algorithm. The simulation cell is placed in a temperature bath at the desired value of 300 K and allowed to evolve according to the input parameters for 100

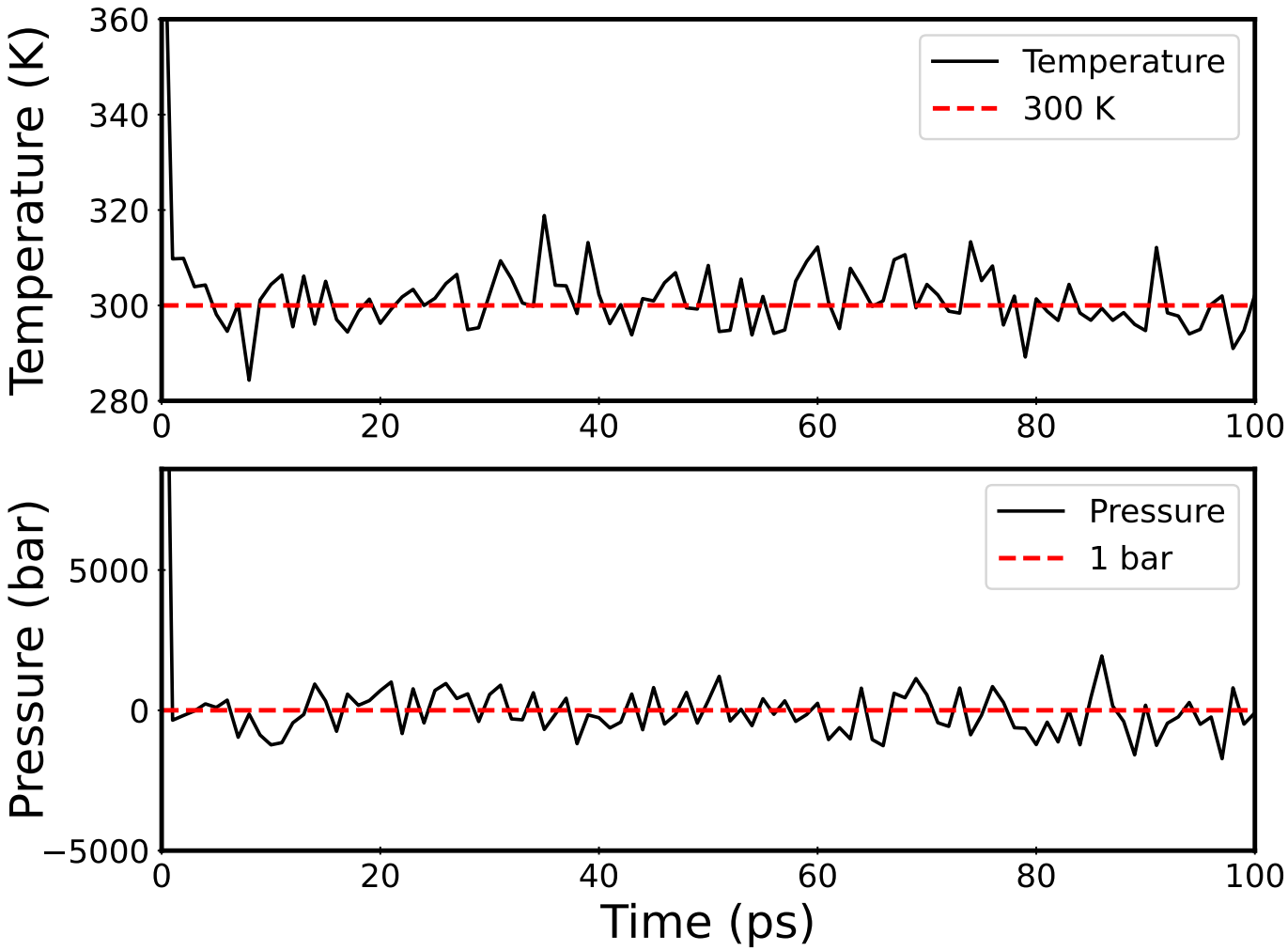

Figure 5.4 Equilibration of the simulation cell is done following energy minimization of the initial configuration shown in Figure 5.2. An NVT run of 100 picoseconds brings the system to the desired temperature of 300 K (top). The simulation is then continued with an NPT run for an additional 100 picoseconds to bring the pressure to a value of 1 bar (bottom).

picoseconds. Figure 5.4(top) shows that the desired average temperature of 300 K is reached and maintained. After the NVT run, the simulation is continued into an NPT (constant **n**umber of particles, **p**ressure and **t**emperature) for an additional 100 picoseconds to allow the pressure to equilibrate at the desired value of 1 bar (see Figure 5.4bottom).

Once the system has equilibrated, a production run of 500 picoseconds is executed. The production run generates a reasonably sized trajectory file that can be split into various snapshots in preparation for the normal mode analysis.

5.2.2 Normal Mode Analysis

As described in the GROMACS documentation, normal-mode analysis is executed by diagonalizing the mass-weighted Hessian, H, as follows:

$$R^T M^{-\frac{1}{2}} H M^{-\frac{1}{2}} R = \text{diag}(\lambda_1, ..., \lambda_{3N}) \tag{5.1}$$

$$\lambda_i = (2\pi\omega_i)^2 \tag{5.2}$$

where M contains the atomic masses, R is a matrix that contains the eigenvectors as columns, λ_i are the eigenvalues and ω_i are the corresponding frequencies. First the $3N \times 3N$ Hessian matrix is calculated according to:

$$H_{ij} = \frac{\partial^2 U}{\partial x_i \partial x_j} \tag{5.3}$$

where x_i and x_j are the coordinates (x, y, or z) of the atoms and U is the potential acting on the atom. Practically, the Hessian is calculated numerically from the force as:

$$H_{ij} = -\frac{f_i(x + he_j) - f_i(x - he_j)}{2h} \tag{5.4}$$

$$f_i = -\frac{\partial U}{\partial x_i} \tag{5.5}$$

where e_j is the unit vector in direction j.[13]

Multiple configurations are extracted from the production run trajectory file at 10 ps intervals to make up the 50 configurations used for the normal mode analysis. The choice of time-slice is only to build multiple VDOS from a single production run and is done for convenience. Each configuration is quenched using the L-BFGS energy minimization integrator and *mdrun*. The *nm* integrator is then used to compute the Hessian Matrix. This matrix is the input for the GROMACS tool *nmeig*, which calculates the eigenvectors and corresponding eigenvalues *via* diagonalizing the Hessian. There are $3N$ - 3 non-zero normal modes where N is the number of particles in the simulation (2500). The first 3 are translations we ignore because there is no energy change. This results in 7497 eigenvectors with

eigenvalues (eigenfrequencies) corresponding to the vibrational mode energy.

Figure 5.5(top) shows each eigenvector's mode energy in wavenumbers. GROMACS sorts the eigenvectors in terms of increasing energy. Regions of low slope, such as between eigenvector index 5000 to 6500, show many vibrational modes of similar energies. In contrast, regions of near-infinite slope show regions where few or no vibrational modes exist with those energies. The eigenfrequencies are more easily interpreted when binned in a histogram to create a VDOS plot. Figure 5.5(bottom) shows the histogram of the vibrational mode energies for one single configuration. A 4 cm^{-1} bin width was used to mirror typical IR data collection settings. We can see qualitative similarities to the calcite and aragonite data previously shown in Chapter 3. No meaningful differences were observed across the individual VDOS plots, supporting the assertion that the system was at equilibrium. The final VDOS for each force-field was created by summating all configurations and normalizing the histogram.

5.3 Force-fields and comparisons to experimental data

The original iteration of the force-field parameters developed by Xiao *et al.* only included improper dihedral angles to constrain the atoms.[21] This was later changed by Cruz-Chu *et al.* to include a rigid bond between the carbon and oxygen atoms for their investigation involving the fracturing of aragonite slabs.[7] I used both of these force fields to generate aragonite VDOS plots to examine the effects of the spring bond on the vibrational mode energies.

Experimental aragonite data collected *via* IR is an excellent point of comparison for the calculated VDOS as, unlike calcite, all internal vibrations are IR-active.[20] It is unclear whether there are any missing aragonite external modes, as the broad nature of experimentally detected bands that incorporate these modes envelop the entire energy range. Others noted that predicted external mode peaks smear together in the vibrational spectra of aragonite.[5,6,20] Figure 5.6(top) shows experimentally collected IR data for a pure aragonite sample in both the Mid-IR region (black, 2000 - 400 cm^{-1}) and the Far-IR region (red, 600 - 100 cm^{-1}). The data are collected separately due to the instrument's optics, as discussed previously in Chapter 3. Each dataset has been normalized to the strongest band (ν_3 for the Mid-IR, B_1 for the Far-IR).

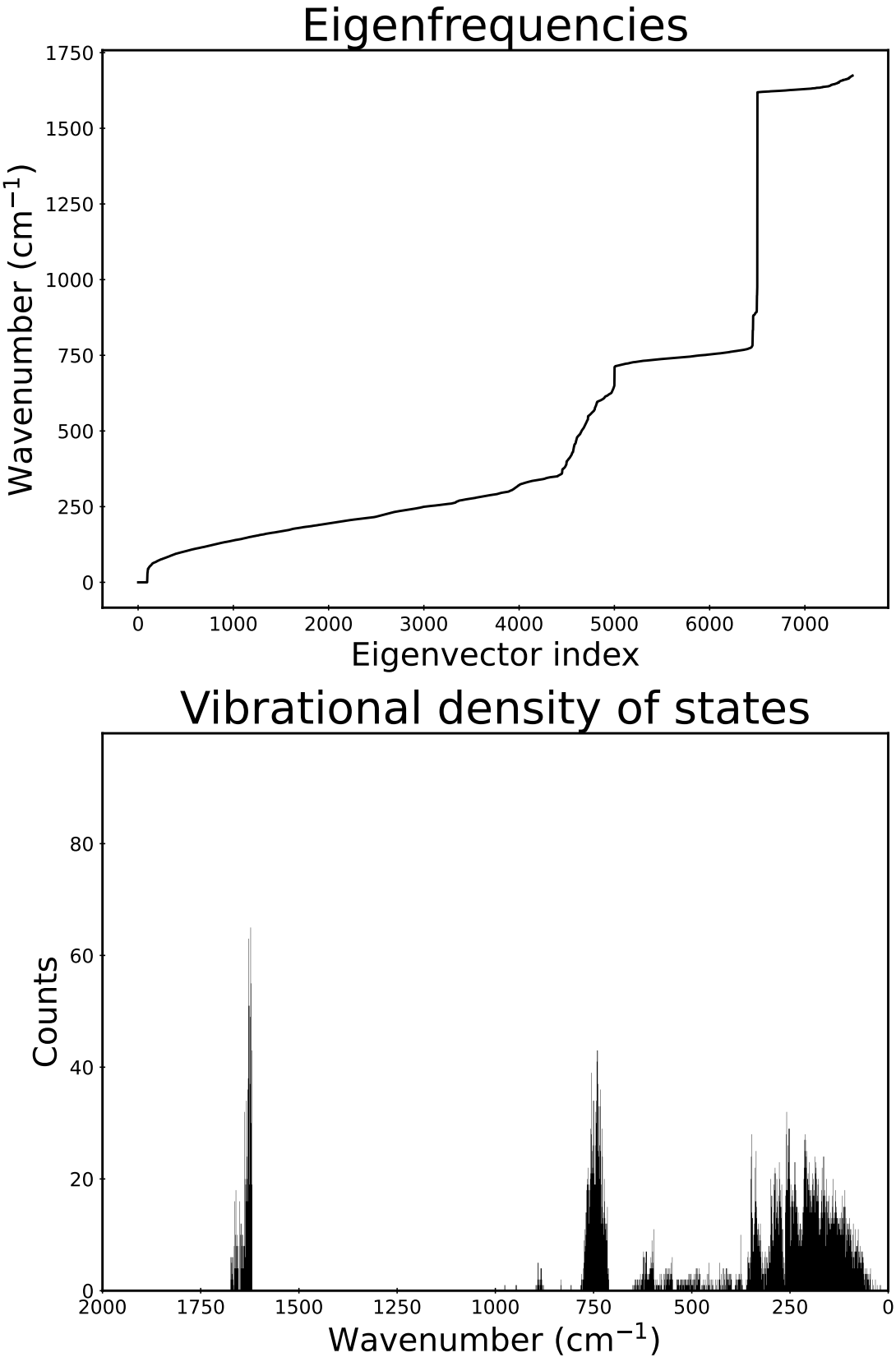

Figure 5.5 The plotted eigenfrequencies (in cm^{-1}) for each eigenvector calculated during the normal mode analysis (top). The vibrational density of states (VDOS) is a histogram generated from these data (bottom).

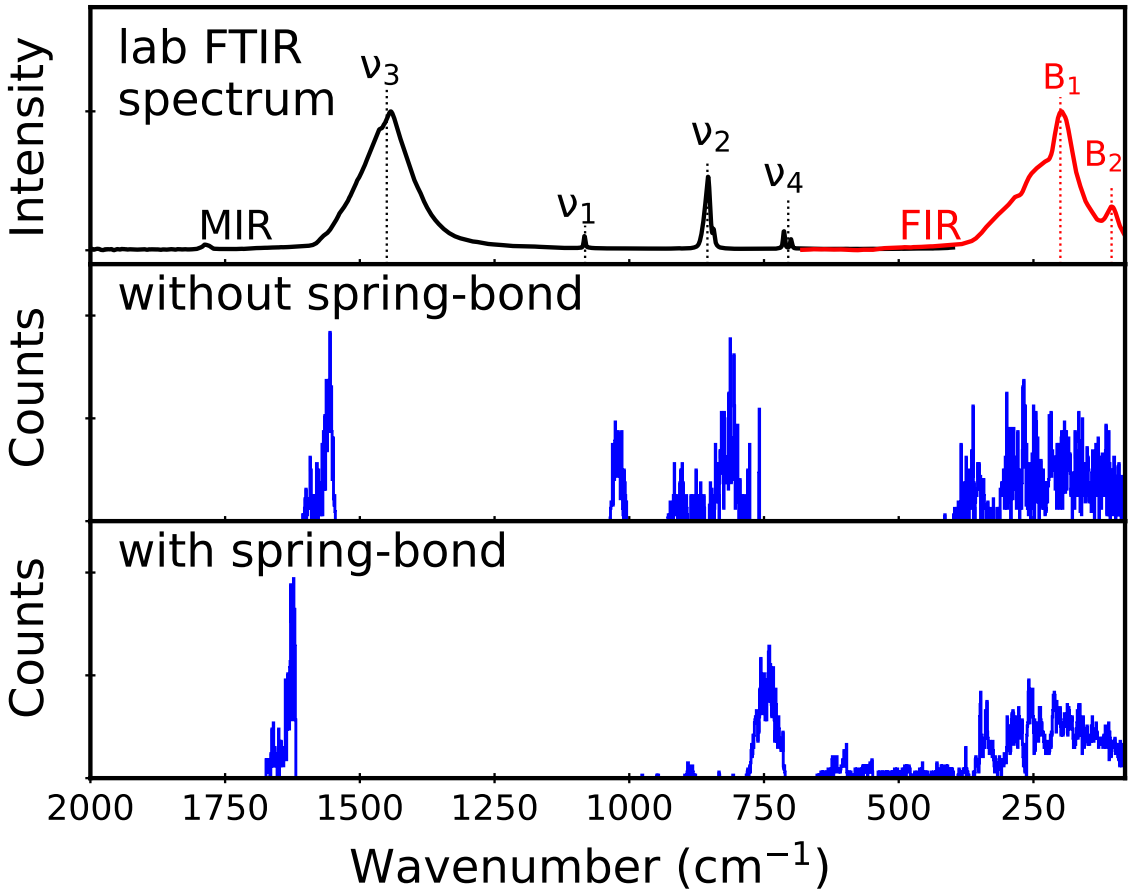

Figure 5.6 Experimental vibrational data for aragonite collected using FTIR methods (top), VDOS using the force field of Xiao *et al.* (middle), which does not include the carbon-oxygen spring bond, and Chuz-Chu *et al.* (bottom) that does. The appearance of internal and external mode bands resembling experimental measurements of aragonite are present in both VDOS. Including the spring bond term (bottom) results in energy changes for the internal modes (2000 - 500 cm^{-1}) and many low-count peaks between 700 cm^{-1} and 400 cm^{-1}, which should not have any modes based on experimental measurements.

The Mid-IR region shows four fundamental internal modes for aragonite. In order of decreasing energy, ν_3 at 1425 cm^{-1} is the most intense. Next is a very weak ν_1 peak at 1080 cm^{-1}. The ν_2 peak at 855 cm^{-1} is the second most prominent. The final vibration, ν_4, is a relatively weak doublet at 712 cm^{-1} and 700 cm^{-1}. The spectral features are significantly broader in the Far-IR region than the Mid-IR peaks. For ease of discussion, the spectral features are described as bands rather than the spectroscopic ν labeled peaks. There are two bands, the most intense B_1 band at 200 cm^{-1}, including an extended shoulder out to nearly 300 cm^{-1}, and a weaker B_2 band at 100 cm^{-1}. We note that B_1 and B_2 are not standard mode designations; they are used as peak labels for our convenience.

A VDOS plot was created using both the Xiao *et al.* force-field (Figure 5.6 middle) and Cruz-Chu *et al.* force-field (Figure 5.6 bottom). The inclusion of the spring-bond term, originally used to maintain the integrity of aragonite slabs, has a visible effect on the vibrational properties of the system, as observed in the VDOS plots. By incorporating the spring bond between the carbon and oxygen atoms, the VDOS shows changes in the internal carbonate mode (above 500 cm^{-1}) and external mode (below 500 cm^{-1}) regions.

Figure 5.6(middle) does not include a rigid bond term between the carbon and oxygen atoms. The Mid-IR region (2000 - 500 cm^{-1}) shows three prominent bands, 1560 cm^{-1}, 1025 cm^{-1}, and 810 cm^{-1}, as well as a minor band at 900 cm^{-1}. As previously described, four is the expected number of bands based on the experimental data for aragonite in the Mid-IR region. Assuming the bands appear in the same order (*i.e.*, ν_1 is higher in energy than ν_2), the bands all appear shifted in terms of energies. The ν_3 peak appears at 1560 cm^{-1}, giving an energy shift of +135 cm^{-1}. The ν_1 mode shifts to lower energies, from 1080 cm^{-1} experimentally to 1025 cm^{-1} in the VDOS (-55 cm^{-1}). Both the ν_2 and ν_4 bands shift upwards, from 855 cm^{-1} to 900 cm^{-1} (+45 cm^{-1}) and 706 cm^{-1} to 810 cm^{-1} (+104 cm^{-1}), respectively. The doublet is no longer resolved in the case of ν_4. The Far-IR region shows significant deviation from the experimental data, now showing one band near 350 cm^{-1} and an additional broad band centered around 200 cm^{-1}, extending from 300 cm^{-1} to 100 cm^{-1}.

The VDOS shown in Figure 5.6(bottom) was generated using the force field that includes a spring-bond interaction between the carbon and oxygen atoms. The Mid-IR region (2000 - 500 cm^{-1}) shows four bands in a different combination of weak and strong peaks than the prior force field. There are

two prominent bands, located at 1620 cm^{-1} and 750 cm^{-1}, with two minor bands at 890 cm^{-1} and 620 cm^{-1}. There is also an extended collection of very weak peaks from 620 cm^{-1} down into the Far-IR region. Again, assuming the correct order of the vibrational energies ($\nu_3 > \nu_1 > \nu_2 > \nu_4$), ν_3 appears at 1650 cm^{-1} (+225 cm^{-1}), ν_1 at 890 cm^{-1} (-190 cm^{-1}), ν_2 centered at 750 cm^{-1} (-105 cm^{-1}) and ν_4, now a resolved doublet, is at 620 cm^{-1} and 605 cm^{-1} (-92 cm^{-1} and -95 cm^{-1}, respectively). The Far-IR region (500 - 100 cm^{-1}) continues to deviate from the experimental data, instead maintaining the broad spectral band from 100 - 300 cm^{-1} and an additional, more narrow, band now at 325 cm^{-1}, that was present in the VDOS plot made using the force-field without C-O the spring-bond (Figure 5.6 middle).

Figure 5.6 exemplifies that the VDOS is sensitive to including a carbon-oxygen spring-bond interaction. This indicates the necessity to validate the results of a given set of simulation parameters against experimental data before exploring the effects of structural changes on the VDOS plots.

It is important to note that the vibrational density of states shows where the energies of the vibrational states are but does not directly indicate what intensities should be expected in the experimental data. These simulations result from normal-mode analysis and, thus, do not incorporate the selection rules for IR or Raman experimental instrumentation. For this reason, it is crucial to resist the temptation to directly compare band intensities between a VDOS and experimental FTIR spectrum. DFT calculations calculate the energies of the modes based on electronic structure and then scale the intensities based on experimental data.[10,22]

5.4 Conclusions

I show that two versions of a currently available molecular dynamics force-field developed by Xaio *et al.*, later modified by Cruz-Chu *et al.*, can be used to simulate the vibrational density of states (VDOS) for aragonite, a polymorph of calcium carbonate. Using a spring-bond interaction term between the carbon and oxygen atoms changes the overall band structure and mode energies. Visual comparison of the computed VDOS plots with experimental IR data for aragonite shows significant deviation for both force fields. The energy shifts are larger overall for the Cruz-Chu *et al.* version (maximum shift +225 cm^{-1}, average 150.5 cm^{-1}), but it appears to encapsulate the Mid-IR profile of aragonite better,

especially with the ν_4 doublet being resolved. By comparing the aragonite VDOS to experimental data, it is clear that both potentials used in this investigation capture many aspects of the basic aragonite IR profile. As such, neither force field can be touted as outright superior when simulating the VDOS of aragonite. Both are reasonable starting points for further VDOS calculations involving disordered calcium carbonate structures.

Important to highlight is the sensitivity of the VDOS plot to the inclusion of the spring-bond term. One of the original goals for this project was to examine the effect of structural changes on the VDOS plots of calcium carbonate minerals, namely aragonite. It was unclear to us at the outset what type and magnitude of structural change to the system would be necessary to induce changes in the VDOS. This research shows that the VDOS of aragonite can be influenced meaningfully by comparing the effects of parameter changes.

The priority for future work should be identifying the type of motion exhibited for each band in the VDOS. GROMACS has tools related to normal mode analysis for this purpose. Having this information would significantly improve the qualitative comparisons that can be made between the VDOS and experimental data. With this information accessible, the next priority should be to tune the potentials to better match experimental data in the internal vibrational mode region. The internal carbonate modes of aragonite are better resolved in energy than the external modes experimentally, and a more extensive wealth of experimental data is available that one can use to validate. It is vital to take this step before using the VDOS in a predictive manner to gain insight into how structural differences would be expected to change experimental IR or Raman data. Once the basic workflow is established, it becomes much easier to computationally investigate modified aragonite lattices, such as those showing lattice strain or elemental substitutions, for comparison with vibrational mode data of less pristine real-world samples.

Bibliography

[1] M. J. Abraham, T. Murtola, R. Schulz, S. Páll, J. C. Smith, B. Hess, and E. Lindahl. Gromacs: High performance molecular simulations through multi-level parallelism from laptops to supercomputers. SoftwareX, 1:19–25, 2015.

[2] H. Berendsen, D. van der Spoel, and R. van Drunen. GROMACS: A message-passing parallel molecular dynamics implementation. Computer Physics Communications, 91(1):43–56, 1995. ISSN 0010-4655. doi: https://doi.org/10.1016/0010-4655(95)00042-E.

[3] H. J. Berendsen. Practical algorithms for dynamic simulations. Molecular-Dynamics Simulation of Statistical-Mechanical Systems, 1986.

[4] H. J. Berendsen. Molecular dynamics simulations: The limits and beyond. In Computational Molecular Dynamics: Challenges, Methods, Ideas: Proceedings of the 2nd International Symposium on Algorithms for Macromolecular Modelling, Berlin, May 21–24, 1997, pages 3–36. Springer, 1999.

[5] T. N. Brusentsova, R. E. Peale, D. Maukonen, G. E. Harlow, J. S. Boesenberg, and D. Ebel. Far infrared spectroscopy of carbonate minerals. American Mineralogist, 95(10):1515–1522, 2010.

[6] L. Couture. Etude des spectres de vibrations de monocristaux ioniques. In Annales de physique, volume 12, pages 5–94. EDP Sciences, 1947.

[7] E. R. Cruz-Chú, S. Xiao, S. P. Patil, K. Gkagkas, and F. Gräter. Organic filling mitigates flaw-sensitivity of nanoscale aragonite. ACS Biomaterials Science & Engineering, 3(3):260–268, 2017.

[8] S. Gonçalves and H. Bonadeo. Vibrational densities of states from molecular-dynamics calculations. Physical Review B, 46(18):12019, 1992.

[9] V. R. Grandy, K. M. Poduska, and I. Saika-Voivod. Vibrational signatures of chemical- and density-induced structural changes in simulated amorphous silica. Canadian Journal of Physics, 92(7/8): 615–618, Jan. 2014. ISSN 0008-4204. doi: 10.1139/cjp-2013-0639.

[10] R. Gueta, A. Natan, L. Addadi, S. Weiner, K. Refson, and L. Kronik. Local atomic order and infrared spectra of biogenic calcite. Angewandte Chemie International Edition, 46(1-2):291–294, Jan. 2007. ISSN 1521-3773. doi: 10.1002/anie.200603327.

[11] B. Hess, C. Kutzner, D. Van Der Spoel, and E. Lindahl. GROMACS 4: algorithms for highly efficient, load-balanced, and scalable molecular simulation. Journal of Chemical Theory and Computation, 4(3):435–447, 2008.

[12] W. Humphrey, A. Dalke, and K. Schulten. VMD: visual molecular dynamics. Journal of Molecular Graphics, 14(1):33–38, 1996.

[13] Lindahl, Abraham, Hess, and van der Spoel. GROMACS 2021.1 manual, Mar. 2021.

[14] E. Lindahl, B. Hess, and D. Van Der Spoel. GROMACS 3.0: a package for molecular simulation and trajectory analysis. Molecular Modeling Annual, 7(8):306–317, 2001.

[15] S. Páll, M. J. Abraham, C. Kutzner, B. Hess, and E. Lindahl. Tackling exascale software challenges in molecular dynamics simulations with GROMACS. In International Conference on Exascale Applications and Software, pages 3–27. Springer, 2014.

[16] K. M. Poduska, L. Regev, E. Boaretto, L. Addadi, S. Weiner, L. Kronik, and S. Curtarolo. Decoupling local disorder and optical effects in infrared spectra: Differentiating between calcites with different origins. Advanced Materials, 23(4):550–554, 2011. ISSN 1521-4095. doi: 10.1002/adma.201003890.

[17] S. Pronk, S. Páll, R. Schulz, P. Larsson, P. Bjelkmar, R. Apostolov, M. R. Shirts, J. C. Smith, P. M. Kasson, D. Van Der Spoel, et al. GROMACS 4.5: a high-throughput and highly parallel open source molecular simulation toolkit. Bioinformatics, 29(7):845–854, 2013.

[18] L. Valenzano, Y. Noel, R. Orlando, C. Zicovich-Wilson, M. Ferrero, and R. Dovesi. Ab initio vibrational spectra and dielectric properties of carbonates: magnesite, calcite and dolomite. Theoretical Chemistry Accounts, 117(5-6):991–1000, 2007. URL https://tutorials.crystalsolutions.eu/index.html.

[19] D. Van Der Spoel, E. Lindahl, B. Hess, G. Groenhof, A. E. Mark, and H. J. Berendsen. GROMACS: fast, flexible, and free. Journal of Computational Chemistry, 26(16):1701–1718, 2005.

[20] W. B. White. The Carbonate Minerals. In The Infrared Spectra of Minerals. Mineralogical Society of Great Britain and Ireland, 01 1974. ISBN 9780903056052. doi: 10.1180/mono-4.12.

[21] S. Xiao, S. A. Edwards, and F. Gräter. A new transferable forcefield for simulating the mechanics of $CaCO_3$ crystals. The Journal of Physical Chemistry C, 115(41):20067–20075, 2011.

[22] B. Xu, A. Hirsch, L. Kronik, and K. M. Poduska. Vibrational properties of isotopically enriched materials: the case of calcite. RSC Advances, 8(59):33985–33992, 2018.

Chapter 6

Conclusions

6.1 Summary of thesis work

The techniques described in the preceding chapters can be used to examine the vibrational properties of solids. Understanding the nuances of these methods before leveraging them to advance the current scientific knowledge base related to disorder in solid materials is essential. This work highlights the strengths and weaknesses of the techniques using calcium carbonate. We added to the knowledge base for both the methods and the material.

Previous studies have highlighted vibrational spectroscopy's ability to identify signatures of structural differences using the internal carbonate vibrational modes.[6,9,12,24,25] Prior to this thesis research, vibrational spectroscopic techniques had not been used to assess the effects of structural differences on external mode vibrations in carbonate mineral samples. Our explicit links between far-infrared (Far-IR, 650-80 cm^{-1}) and mid-infrared (Mid-IR, 4000-400 cm^{-1}) data is the first of its kind, and it helps move us toward our ultimate goal of using spectroscopic analysis strategies for tracking structural differences in materials due to processing, aging, or use-based changes. We demonstrate that calcite-aragonite-portlandite mixtures can show apparent peak shifts in the Far-IR spectral range using spectra collected using attenuated total reflectance (ATR) Fourier transform infrared spectroscopy (FTIR). We show that relative peak intensity changes between overlapping peaks – without peak energy shifts in the constituent peaks – are sufficient to explain peak position changes. These results

benefit those working with heat-treated calcium carbonate samples wherein phase mixtures are commonly observed. Another takeaway from this work was that the lower energy bands are significantly broader than the internal modes. Past experimental work has shown that IR vibrations broaden with increasing temperature.[24] When a crystal lattice change (*i.e.* phase transition) is not relevant, as is the case with calcite and aragonite below 700 K, this effect is attributed to the anharmonic nature of the vibrations. The expectation is that since the external mode energies are comparable to k_BT (corresponding to an energy of 207 cm^{-1} at 300 K), the bands should be broader than the internal modes, as they have comparatively more thermal energy at room temperature. Combine this with the very similar energies of 2 sets of 2 modes (ν_6 and ν_8, ν_7 and ν_{10}), and it is perhaps not surprising that the resultant spectra show three prominent bands instead of 5. Ultimately, it makes it significantly harder to identify and decouple the changes we look for, such as peak broadening, peak shifts, and relative intensity changes, in the external modes compared to the internal modes. We attempted Williamson-Hall analysis on the powder X-ray diffraction (PXRD) data. However, it was unsuccessful, likely due to the Bragg peak widths being dominated by instrumental broadening rather than structural effects. To address the instrument broadening quantitatively, one would use a silicon standard to measure it, thus enabling the sample data to be adjusted.

Photoacoustic spectra in the Mid-IR range show persistent, repeatable enhancement of weak peaks associated with combination modes, overtones, and isotopic species in calcite relative to transmission and ATR spectra of this material. To help explain this phenomenon, we conducted experiments centered around the idea that these effects were related to the saturation of fundamental peaks. By exploring the effects of mirror speed and transducer type, data collected with step-scan and rapid-scan modes, and the linearization data correction method, we show that saturation effects are not a reasonable explanation for this enhancement. Instead, this enhancement is intrinsic to the detection method (PAS), and we note that an adequate theoretical explanation for this long-standing phenomenon has yet to be developed.

Calculations of the vibrational modes of calcium carbonate structures have previously used density functional theory (DFT) methods to investigate the effects of structural changes on the internal carbonate vibrational modes. However, these methods are not feasible for the external modes.[6,20]

Molecular dynamics (MD) methods offer the ability to explore the effects of structural differences on the vibrational density of states (VDOS), a similar type of data to that collected *via* vibrational spectroscopic methods. The goal of the MD simulations was first to replicate the work of Grandy *et al.* for calcium carbonates rather than silicates. That is, to run a molecular dynamics simulation that encapsulates the intrinsic vibrational properties of calcium carbonate systems. The first milestone is to do this for pure systems before extending this to systems modified intelligently (*i.e.* include specific disorder) to help understand and interpret experimental data. Specifically, we seek to study the effects of different types of disorder on the VDOS of the system as an analog for the currently available and future FTIR data.[2–4,9,10,18,24–26]

The currently available force field parameters used for calcium carbonate simulations of Xiao *et al.*[23] and Cruz-Chu *et al.*[5] are reasonable starting points to generate a VDOS that shows qualitative agreement with experimentally collected data. This comparison shows that the model captures the basic profile of aragonite, but it remains to be seen whether the vibrational mode energies correspond to their experimentally measured counterparts.

Overall, these projects identify some of the strengths and weaknesses of the methods in leveraging vibrational modes better to understand the effects of structural disorder in solids. Further, they highlight opportunities for additional experimental and computational work surrounding calcium carbonate minerals.

6.2 Broader view and future work

This dissertation seeks to advance the scientific understanding of ordering in solid materials by anchoring new data related to either novel energy ranges or oft-overlooked measurement technique idiosyncrasies with our current understanding and expertise of the case study materials. The initial conception was to use our established expertise with calcium carbonate materials and our understanding of the fundamental technique, Fourier transform infrared spectroscopy (FTIR), to explore these materials' minimally examined external mode vibrations in the context of structural disorder. No single experimental technique can examine atomic level disorder across the length scales we investigated. Instead, we must build our understanding by combining data and conclusions from different

techniques to explain what is happening in the material.

The energy ranges explored by Far-IR FTIR overlap with techniques used to explore quasi-particles such as magnons.[1,19] Researchers have examined the vibrational dynamics of different systems to elucidate the mechanisms for photoinduced phase transitions.[21] According to Wang *et al.* "understanding and manipulating complex phase transition phenomena in strongly correlated oxides are among the most important issues in condensed matter physics, with both fundamental and technological implications."[21] The authors allude to the potential of the studied material, highlighting the potential of selectively triggering an electronic transition for improved speed of optical/electrical modulation devices since this transition does not require a lattice transformation to happen.

Each of the projects discussed in this dissertation has natural continuations that would advance the ability of researchers to leverage vibrational mode information of solids to understand the effects of structural disorder. The following is an outline of further directions that this work could be taken.

6.2.1 Photoacoustic detection

The results of this study address a fascinating and long-standing effect consistent with published and unpublished data from others, but that has never been addressed directly in published literature. This is the first time anyone has attempted to describe the weak peak enhancement inherent to FTIR-PAS. We could only show conclusively that PAS weak peak enhancement is not caused by detector saturation. Further, the results leave the obvious next steps in plain sight: identify the cause of the enhancement. The Rosencwaig-Gersho theory[13–16] describing the photoacoustic effect in solids depicts how the magnitude and phase of the photoacoustic signal vary with chopping frequency (modulation) and normalized thermal diffusion length. Theoretical explanations of the vibrational mode intensities, both the fundamental modes and the weaker isotopic, overtone, and combination modes, are yet to be developed.

One of the manuscript reviewers suggested that the enhancement originated from the lateral scattering of the photoacoustic (PA) signal. A minimum amount of sample, typically enough to cover the bottom of the cup completely, is required to get the maximum signal experimentally. However, beyond this amount, no increase in signal has been observed. This suggests that the photoacoustic signal of

powdered samples is only generated within the top layers. As such, lateral scattering of the thermal radiation in this signal-generating layer may enhance the PA signal. However, it remains to be seen why the weak bands appear enhanced compared to the fundamentals without evidence of saturation.

The experiments to examine the signal increase due to lateral scattering are straightforward. By diluting the sample powder using spectroscopic grade potassium bromide in varying ratios, the data should clearly show the effect of reduced lateral scattering as the dilutant:sample ratio increases. If this hypothesis is correct, the effects should be similar to those observed in transmission measurements when sample pellets are reground and pressed again.[9]

6.2.2 FTIR-ATR external modes

The external modes of calcium carbonate materials are understood theoretically and have been measured previously experimentally using FTIR methods as well as similar Terahertz Time-Domain Spectroscopy (THz-TDS).[2,7,17,20,22] THz-TDS is another spectroscopic technique that operates in a comparable energy range to vibrational modes. The method involves generating a broadband terahertz pulse to probe the sample rather than the broadband IR source used in FTIR. While commercial THz-TDS setups are limited to the low end of the Far-IR region (typically up to near 110 cm^{-1}), some systems have been developed that can extend well into the Mid-IR region. Ignoring the possible bandwidth-related issues, THz-TDS is exciting as it measures the electric field of the THz pulse, allowing for data collected to contain information about the sample's effect on both amplitude and phase at a given frequency (wavenumber). This could lead to vibrational mode information that is not accessible using FTIR.

FTIR has often been used to identify vibrational bands, or peaks, of calcium carbonates to distinguish between different types of samples, such as aragonite and calcite. My research uses these same techniques to compare differences between samples of the same structure to identify more subtle disparities that correlate with structural differences. This methodology has been successfully used with calcite samples' internal carbonate vibrational modes.[9,12,18,24]

Difficulties distinguishing trends in the external modes primarily arose from using mixed-phase samples that dominated the spectral changes. Future work could repeat these measurements using

carefully curated samples of calcite or aragonite, but not mixtures, to help identify structural change signatures in the external modes.

A drawback of using these specific FTIR methods is that the Mid-IR and Far-IR energy ranges must be collected separately due to optical limitations. Moving forward, a bandwidth encompassing both the internal and external modes of calcium carbonates could be achieved simultaneously using a THz-TDS apparatus. This opens up the possibility for relative peak intensity comparisons between the internal and external modes. This may help identify interesting trends we cannot assess due to the two separate collection windows used in FTIR setups. This project would take significant work, as it requires the familiarization of calcium carbonate vibrational modes measured using a more novel method. Published THz-TDS data for calcium carbonates appear similar to the Far-IR data visually[17], but care must be taken when working with these samples. Our work highlighted that observed changes could come from alternate sources, such as phase mixing, so similar sample selection considerations must be given. Using the internal modes in conjunction with the external modes to resolve ambiguity worked for FTIR methods and should also be possible using THz-TDS.

6.2.3 Molecular Dynamics vibrational density of states

The molecular dynamics (MD) simulations resulted in two similar, distinct vibrational density of states (VDOS) plots for aragonite (see Figure 5.6). The types of vibrations (*i.e.*, bend, stretch, or wag) appearing in these plots as peaks remain to be determined. Doing so would allow for more comprehensive comparisons between the VDOS and experimentally collected data. This critical step opens up the ability to simulate specific types of disorder in the material and examine the effect on the VDOS. From there, links between available experimental data could result in a way to identify the type of disorder that causes the observed IR spectral changes.

To further develop the MD simulations as a reliable tool for experimental data correlations, additional steps should be taken to improve confidence in the methodology. Alternate force field parameters for calcium carbonate MD simulations available in the literature should be used to generate VDOS data.[8,11] The parameters used in this investigation were not explicitly developed to encapsulate the vibrational modes of these materials. The original motivation was to capture the elastic properties of

these solids.[23] Comparing all available force fields should be a priority.

Additionally, simulations of calcite would open up additional experimental data for comparison. Both minerals are relevant for many of the same fields. Once these fundamental steps are taken, work involving disordered systems should begin earnestly. Simulating a phase-mixture would be ideal for directly comparing the Far-IR work discussed in Chapter 3. One way this could be accomplished is to generate a VDOS for each aragonite and calcite and then calculate a linear-combination VDOS at different percentages to compare with the experimental data discussed in Chapter 3. Alternatively, a more sophisticated simulation involving the nucleation of calcium carbonate from ions in solution could be used to produce mixed phases. This could lead to inter-growths of the two crystal phases, generating interesting types of disorder at the phase boundaries. Additional experimental work would be necessary to get comparative data.

Bibliography

[1] V. Besse, A. Golov, V. Vlasov, A. Alekhin, D. Kuzmin, I. Bychkov, L. Kotov, and V. Temnov. Generation of exchange magnons in thin ferromagnetic films by ultrashort acoustic pulses. Journal of Magnetism and Magnetic Materials, 502:166320, 2020.

[2] T. N. Brusentsova, R. E. Peale, D. Maukonen, G. E. Harlow, J. S. Boesenberg, and D. Ebel. Far infrared spectroscopy of carbonate minerals. American Mineralogist, 95(10):1515–1522, 2010.

[3] S. Campbell and K. M. Poduska. Incorporating far-infrared data into carbonate mineral analyses. Minerals, 10(7):628, 2020. doi: 10.3390/min10070628.

[4] S. Campbell, M. Dusseault, B. Xu, K. H. Michaelian, and K. M. Poduska. Photoacoustic detection of weak absorption bands in infrared spectra of calcite. Applied Spectroscopy, 75(7):795–801, 2021. doi: 10.1177/00037028211009212. PMID: 33783238.

[5] E. R. Cruz-Chú, S. Xiao, S. P. Patil, K. Gkagkas, and F. Gräter. Organic filling mitigates flaw-sensitivity of nanoscale aragonite. ACS Biomaterials Science & Engineering, 3(3):260–268, 2017.

[6] R. Gueta, A. Natan, L. Addadi, S. Weiner, K. Refson, and L. Kronik. Local atomic order and infrared spectra of biogenic calcite. Angewandte Chemie International Edition, 46(1-2):291–294, Jan. 2007. ISSN 1521-3773. doi: 10.1002/anie.200603327.

[7] L. L. Long, M. R. Querry, R. J. Bell, and R. W. Alexander. Optical properties of calcite and gypsum in crystalline and powdered form in the infrared and far-infrared. Infrared Physics, 34:191–201, 1993. URL https://api.semanticscholar.org/CorpusID:12236767.

[8] A. Pavese, M. Catti, G. Price, and R. Jackson. Interatomic potentials for $CaCO_3$ polymorphs (calcite and aragonite), fitted to elastic and vibrational data. Physics and Chemistry of Minerals, 19(2):80–87, 1992.

[9] K. M. Poduska, L. Regev, E. Boaretto, L. Addadi, S. Weiner, L. Kronik, and S. Curtarolo. Decoupling local disorder and optical effects in infrared spectra: Differentiating between calcites with different origins. Advanced Materials, 23(4):550–554, 2011. ISSN 1521-4095. doi: 10.1002/adma.201003890.

[10] K. M. Poduska, L. Regev, F. Berna, E. Mintz, I. Milevski, H. Khalaily, S. Weiner, and E. Boaretto. Plaster characterization at the PPNB site of Yiftahel (Israel) including the use of ^{14}C: implications for plaster production, preservation, and dating. Radiocarbon, 54(3-4):887–896, 2012.

[11] P. Raiteri and J. D. Gale. Water is the key to nonclassical nucleation of amorphous calcium carbonate. Journal of the American Chemical Society, 132(49):17623–17634, 2010.

[12] L. Regev, K. M. Poduska, L. Addadi, S. Weiner, and E. Boaretto. Distinguishing between calcites formed by different mechanisms using infrared spectrometry: archaeological applications. Journal of Archaeological Science, 37(12):3022–3029, 2010.

[13] A. Rosencwaig. Photoacoustic spectroscopy of solids. Optics Communications, 7(4):305 – 308, 1973. ISSN 0030-4018. doi: http://dx.doi.org/10.1016/0030-4018(73)90039-4.

[14] A. Rosencwaig. Photoacoustic spectroscopy. New tool for investigation of solids. Analytical Chemistry, 47(6):592A–604a, May 1975. ISSN 0003-2700. doi: 10.1021/ac60356a015.

[15] A. Rosencwaig. Photoacoustics and Photoacoustic Spectroscopy. Wiley, 1980.

[16] A. Rosencwaig and A. Gersho. Theory of the photoacoustic effect with solids. Journal of Applied Physics, 47:64–69, Jan. 1976. doi: 10.1063/1.322296.

[17] S. Sakai, D. Yang, T. Yasuda, K. Akiyama, T. Kuga, A. Kano, F. Shiraishi, S. Amekawa, S. Ohtsuka, K. Nakaguchi, et al. Pulsed terahertz radiation for sensitive quantification of carbonate minerals. ACS Omega, 4(2):2702–2707, 2019.

[18] M. B. Toffolo and E. Boaretto. Nucleation of aragonite upon carbonation of calcium oxide and calcium hydroxide at ambient temperatures and pressures: a new indicator of fire-related human activities. Journal of Archaeological Science, 49:237–248, 2014.

[19] A. Trzaskowska, P. Graczyk, N. Babu, M. Zdunek, H. Głowiński, J. Kłos, and S. Mielcarek. The studies on phonons and magnons in $[CoFeB/Au]_n$ multilayers of different number of repetitions. Journal of Magnetism and Magnetic Materials, 549:169049, 2022.

[20] L. Valenzano, Y. Noel, R. Orlando, C. Zicovich-Wilson, M. Ferrero, and R. Dovesi. Ab initio vibrational spectra and dielectric properties of carbonates: magnesite, calcite and dolomite. Theoretical Chemistry Accounts, 117(5-6):991–1000, 2007. URL `https://tutorials.crystalsolutions.eu/index.html`.

[21] Y. Wang, Z. Nie, Y. Shi, Y. Wang, and F. Wang. Coherent vibrational dynamics of NbO_2 film. Physical Review Materials, 6(3):035005, 2022.

[22] W. B. White. The Carbonate Minerals. In The Infrared Spectra of Minerals. Mineralogical Society of Great Britain and Ireland, 01 1974. ISBN 9780903056052. doi: 10.1180/mono-4.12.

[23] S. Xiao, S. A. Edwards, and F. Gräter. A new transferable forcefield for simulating the mechanics of $CaCO_3$ crystals. The Journal of Physical Chemistry C, 115(41):20067–20075, 2011.

[24] B. Xu and K. M. Poduska. Linking crystal structure with temperature-sensitive vibrational modes in calcium carbonate minerals. Physical Chemistry Chemical Physics, 16(33):17634–17639, 2014.

[25] B. Xu, M. B. Toffolo, L. Regev, E. Boaretto, and K. M. Poduska. Structural differences in archaeologically relevant calcite. Analytical Methods, 7(21):9304–9309, 2015.

[26] B. Xu, M. B. Toffolo, E. Boaretto, and K. M. Poduska. Assessing local and long-range structural disorder in aggregate-free lime binders. Industrial and Engineering Chemistry Research, 55(30): 8334–8340, 2016.

Appendix A

The effects of modulation frequency on PAS spectra

A.1 Motivation

The PA301 photoacoustic cell (Gasera) is known to have detrimental resonance effects at specific modulation frequencies. Measurements taken in rapid-scan mode modulate each wavenumber with a different frequency, resulting in cell resonance effects appearing at different wavenumbers for different modulation frequencies.

The same sample preparation of high crystallinity calcite (Alfa Aesar, purchased) was used to investigate the usable range of modulation frequencies and to generate a spectrum where all vibrational modes of interest (1600 cm^{-1}- 600 cm^{-1}) are not saturated. The powder was ground for approximately 3 minutes before loading in a sample cup. Carbon black (Gasera) was used as a reference sample.

These scans were executed in ambient air in the interest of time saved. The PAS cell was not purged prior to data collection. For this reason, water and CO_2 are present in all spectra.

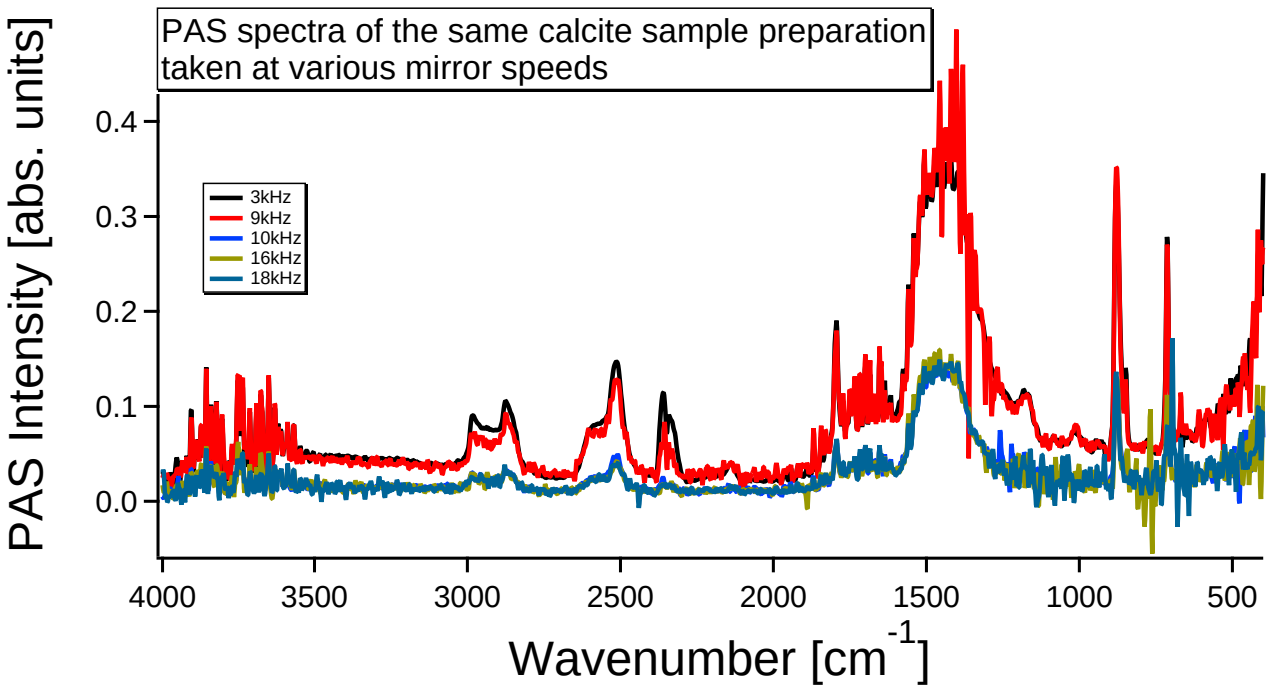

Figure A.1 PAS spectra of the same highly crystalline calcite sample. All bands of calcite are present and appear unaffected by cell resonance issues.

A.2 Data plots

Figure A.1 shows a selection of modulation frequencies across the entire experimental range. These data appear unaffected by cell resonance effects. There is an apparent change in overall signal intensity between 9 kHz and 10 kHz. All relevant bands of calcite are present. Interestingly, the relative peak intensity ratios appear constant based on rough estimates of the ν_3 peak intensity. The spectrum taken at 18 kHz shows a decrease in nu_4 relative intensity but does not have the ^{13}C ν_2 band, suggesting that this modulation frequency may be unusable. The fingerprint region for the same data is highlighted in Figure A.2.

It was found that certain speeds were not viable for calcite samples, as at least one of the vibrational modes in the fingerprint region was distorted beyond usability. Figure A.4 shows the data collected at modulation frequencies of 14, 17, 19, 20, 25, and 30 kHz. The region highlighting the vibrational modes of interest (900 cm^{-1}- 690 cm^{-1}) for the problematic scans is shown in Figure A.5.

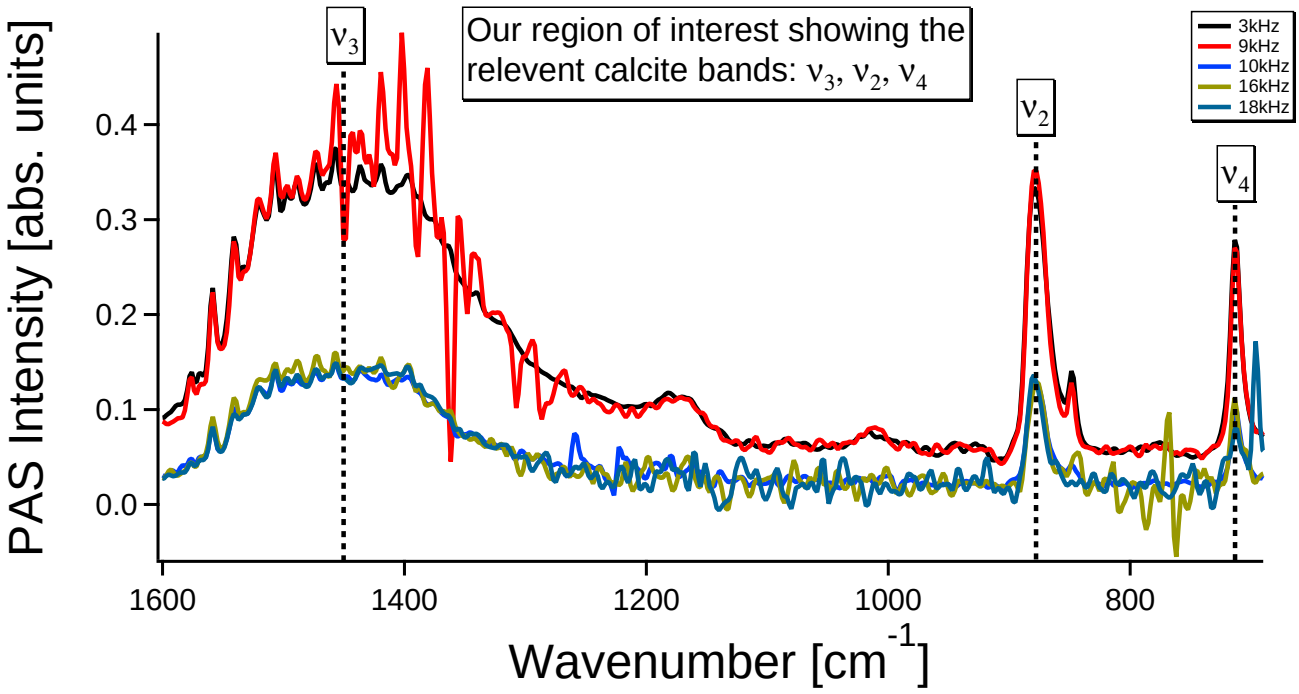

Figure A.2 Fingerprint region for calcite modulation frequency checks. Relative peak intensities appear constant in all scans except for 18 kHz.

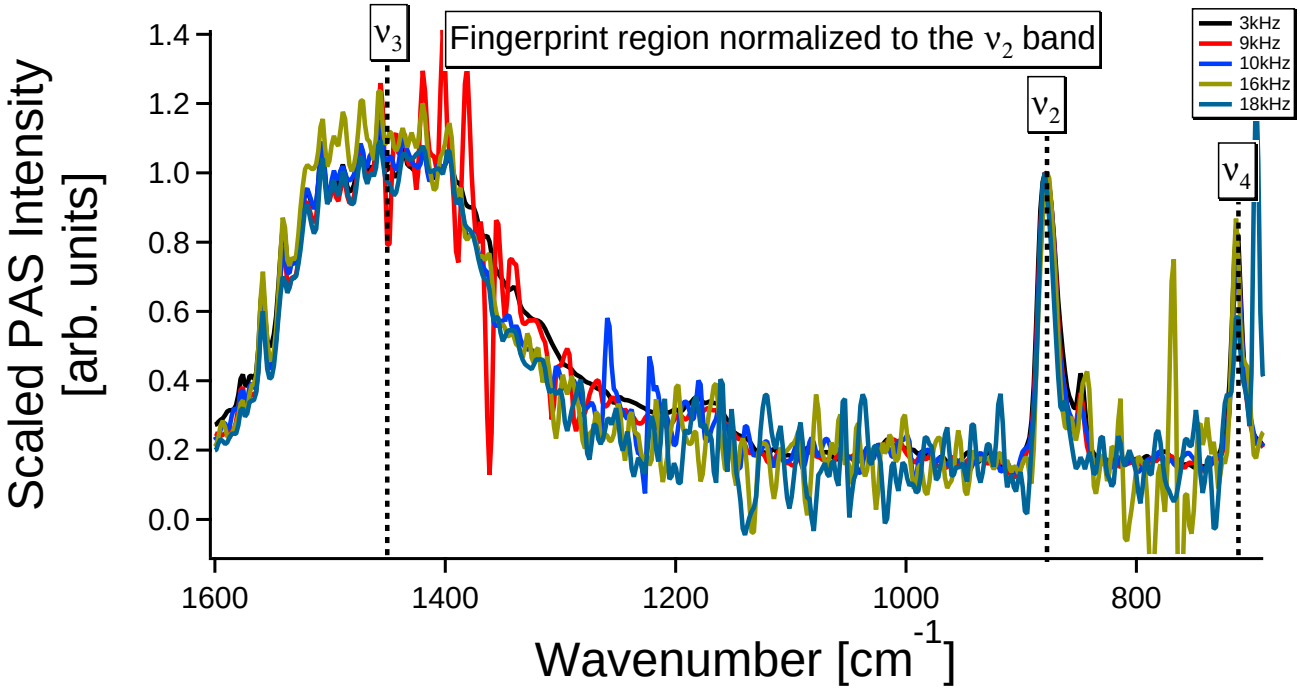

Figure A.3 Fingerprint region of calcite normalized to the ν_2 band. This wavenumber range highlights the consistency of the relative peak intensities at these modulation frequencies, excluding 18 kHz.

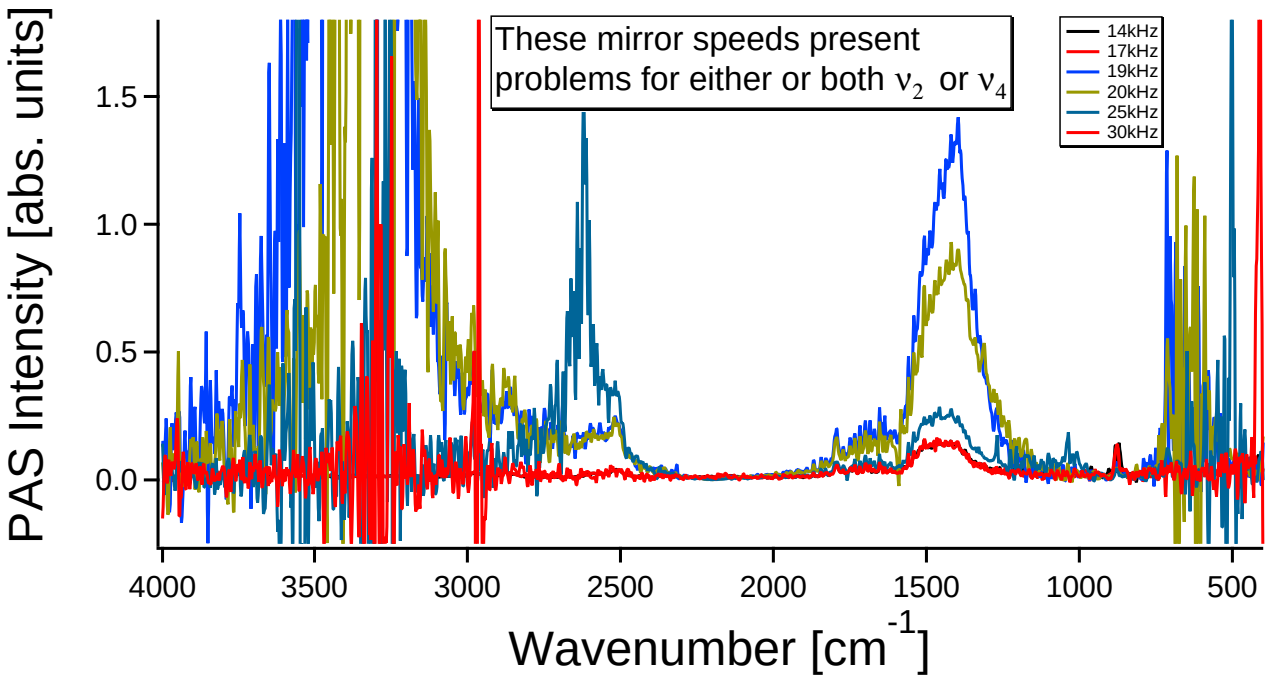

Figure A.4 Data collected with modulation frequencies of 14, 17, 19, 20, 25, and 30 kHz so significant distortions to the ν_2 and ν_4 vibrational modes. Intensity cut off at 1.8 absorbance units for clarity.

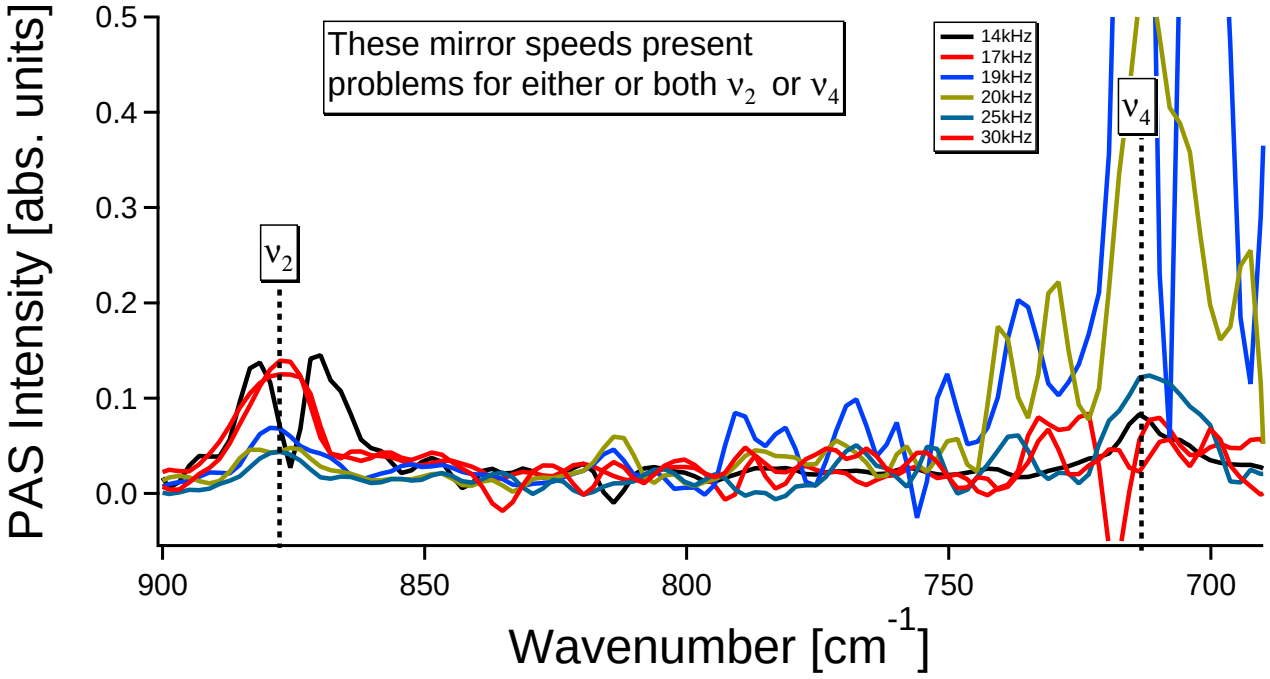

Figure A.5 The ν_2 and ν_4 vibrational modes are affected by cell resonance issues such that the data cannot be trusted.

Appendix B

Calculation process details

The following outlines how to create a vibrational density of states step-by-step. The following input files enable one to reproduce procedures described in Chapter 5.

B.1 Energy minimization

The first step towards creating a vibrational density of states for aragonite is to minimize the system energy. To do this, using the GROMACS software suite requires three input files: the molecular dynamics parameters (.mdp), the structure (.gro), and the topology (.top). The structure and topology files (conf.gro and topol.top, respectively) were created following the instructions outlined in the supplementary files made available by Cruz-Chu *et al.* [1] The molecular dynamics parameters (minim.mdp, nvt.mdp, npt.mdp, md.mdp, nm.mdp, and lbfgs.mdp) are included below.

Listing B.1 minim.mdp input file for energy minimization

```
1 ; minim.mdp - used as input into grompp to generate em.tpr
2 ; Parameters describing what to do, when to stop, and what to save
3 integrator  = cg             ; Conjugate-gradient minimization algorithm
4 nstcgsteep  = 100            ; Perform a steepest decent step every <nstcgsteep> steps
5 emtol       = 0.001          ; Stop minimization when the maximum force < 0.001 kJ/mol/
      nm
6 emstep      = 0.0001         ; Minimization step size
7 nsteps      = 50000          ; Maximum number of (minimization) steps to perform
```

```
8
9 ; Parameters describing how to find the neighbors of each atom and how to calculate the
      interactions
10 nstlist         = 1          ; Frequency to update the neighbor list and long range
      forces
11 cutoff-scheme   = Verlet     ; Buffered neighbor searching
12 ns_type         = grid       ; Method to determine neighbor list (simple, grid)
13 coulombtype     = PME        ; Treatment of long range electrostatic interactions
14 rcoulomb        = 1.0        ; Short-range electrostatic cut-off
15 rvdw            = 1.0        ; Short-range Van der Waals cut-off
16 pbc             = xyz        ; Periodic Boundary Conditions in all 3 dimensions
```

B.2 Constant number of particles, volume, and temperature (NVT)

Following the energy minimization, the system needs to be brought up to the simulation temperature of 300K.

Listing B.2 nvt.mdp input file for constant NVT

```
1 title                   = CaCO3 NVT equilibration
2
3 ; RUN CONTROL PARAMETERS
4 integrator               = md        ; leap-frog integrator
5 nsteps                   = 50000     ; 2 * 50000 = 100 ps
6 dt                       = 0.002     ; 2 fs
7 comm-mode                = Linear    ; mode for center of mass motion removal
8 nstcomm                  = 1         ; number of steps for center of mass motion removal
9
10 ; OUTPUT CONTROL OPTIONS
11 nstxout                 = 500       ; save coordinates every 1.0 ps
12 nstvout                 = 500       ; save velocities every 1.0 ps
13 nstenergy               = 500       ; save energies every 1.0 ps
14 nstlog                  = 500       ; update log file every 1.0 ps
15
16 ; OPTIONS FOR BONDS
```

```
17 ; Bond parameters
18 continuation            = no         ; first dynamics run
19 constraint_algorithm    = lincs      ; holonomic constraints
20 constraints             = all-angles ; all bond angles
21 lincs-iter              = 1          ; accuracy of LINCS
22 lincs-order             = 4          ; also related to accuracy
23 lincs-warnangle         = 90         ; maximum angle that a bond can rotate before LINCS
       will complain
24
25 ; Nonbonded settings
26 cutoff-scheme           = Verlet     ; Buffered neighbor searching
27 ns_type                 = grid       ; search neighboring grid cells
28 nstlist                 = 100        ; 100 fs, largely irrelevant with Verlet
29 rcoulomb                = 1.0        ; short-range electrostatic cutoff (in nm)
30 rvdw                    = 1.0        ; short-range van der Waals cutoff (in nm)
31 DispCorr                = EnerPres   ; Apply long range dispersion corrections for
      Energy and Pressure
32 table-extension         = 1          ; Extension of the potential lookup tables beyond
      the cut-off
33
34 ; Electrostatics
35 coulombtype             = PME        ; Particle Mesh Ewald for long-range electrostatics
36 pme_order               = 4          ; cubic interpolation
37 fourierspacing          = 0.16       ; grid spacing for FFT
38 vdw-type                = cut-off    ; Method for doing Van der Waals
39
40 ; Temperature coupling is on
41 tcoupl                  = nose-hoover ; Nose-Hoover thermostat
42 tc-grps                 = system      ; no groups in our aragonite slab
43 tau_t                   = 0.1         ; time constant, in ps
44 ref_t                   = 300         ; reference temperature, in K
45 ; Pressure coupling is off
46 pcoupl                  = no        ; no pressure coupling in NVT
47 ; Periodic boundary conditions
```

```
48 pbc                    = xyz       ; 3-D PBC
49 ; Velocity generation
50 gen_vel                = yes       ; assign velocities from Maxwell distribution
51 gen_temp               = 300       ; temperature for Maxwell distribution
52 gen_seed               = 508934891 ; the seed Shahrazad had given me
```

B.3 Constant number of particles, pressure, and temperature (NPT)

Listing B.3 npt.mdp input file for constant NPT

```
1 title                   = CaCO3 NPT equilibration
2
3 ; RUN CONTROL PARAMETERS
4 integrator              = md        ; leap-frog integrator
5 nsteps                  = 50000     ; 2 * 50000 = 100 ps
6 dt                      = 0.002     ; 2 fs
7 comm-mode               = Linear    ; mode for center of mass motion removal
8 nstcomm                 = 1         ; number of steps for center of mass motion removal
9
10 ; OUTPUT CONTROL OPTIONS
11 nstxout                = 500       ; save coordinates every 1.0 ps
12 nstvout                = 500       ; save velocities every 1.0 ps
13 nstenergy              = 500       ; save energies every 1.0 ps
14 nstlog                 = 500       ; update log file every 1.0 ps
15
16
17 ; OPTIONS FOR BONDS
18 ; Bond parameters
19 continuation           = yes       ; Restarting after NVT
20 constraint_algorithm   = lincs     ; holonomic constraints
21 constraints            = all-angles ; all bond angles
22 lincs-iter             = 1         ; accuracy of LINCS
23 lincs-order            = 4         ; also related to accuracy
24 lincs-warnangle        = 90        ; maximum angle that a bond can rotate before LINCS
       will complain
```

```
25
26 ; Nonbonded settings
27 cutoff-scheme           = Verlet     ; Buffered neighbor searching
28 ns_type                 = grid       ; search neighboring grid cells
29 nstlist                 = 10         ; 20 fs, largely irrelevant with Verlet
30 rcoulomb                = 1.0        ; short-range electrostatic cutoff (in nm)
31 rvdw                    = 1.0        ; short-range van der Waals cutoff (in nm)
32 DispCorr                = EnerPres   ; Apply long range dispersion corrections for
       Energy and Pressure
33 table-extension         = 1          ; Extension of the potential lookup tables beyond
       the cut-off
34
35 ; Electrostatics
36 coulombtype             = PME        ; Particle Mesh Ewald for long-range electrostatics
37 pme_order               = 4          ; cubic interpolation
38 fourierspacing          = 0.16       ; grid spacing for FFT
39 vdw-type                = cut-off    ; Method for doing Van der Waals
40
41 ; Temperature coupling is on
42 tcoupl                  = nose-hoover ; Nose-Hoover thermostat
43 tc-grps                 = system      ; no groups in our aragonite slab
44 tau_t                   = 0.1         ; time constant, in ps
45 ref_t                   = 300         ; reference temperature, in K
46 ; Pressure coupling is on
47 pcoupl                  = berendsen   ; Pressure coupling on in NPT
48 pcoupltype              = isotropic   ; uniform scaling of box vectors
49 tau_p                   = 1.0         ; time constant, in ps
50 ref_p                   = 1           ; reference pressure, in bar
51 compressibility         = 5e-5        ; Taken from Xaio et. al. via Shahrazad
52
53 ; Periodic boundary conditions
54 pbc                     = xyz       ; 3-D PBC
55 ; Velocity generation
56 gen_vel                 = no        ; Velocity generation is off
```

B.4 Production run

Listing B.4 md.mdp input file for production run

```
title                    = CaCO3 Production MD

; RUN CONTROL PARAMETERS
integrator               = md        ; leap-frog integrator
nsteps                   = 250000    ; 2 * 250000 = 500 ps
dt                       = 0.002     ; 2 fs
comm-mode                = Linear    ; mode for center of mass motion removal
nstcomm                  = 1         ; number of steps for center of mass motion removal

; OUTPUT CONTROL OPTIONS
nstxout                  = 1000      ; save coordinates every 2.0 ps
nstvout                  = 1000      ; save velocities every 2.0 ps
nstenergy                = 1000      ; save energies every 2.0 ps
nstlog                   = 1000      ; update log file every 2.0 ps
nstxout-compressed       = 1000      ; save the compressed coordinates every 2.0 ps
compressed-x-grps        = System    ; save the whole system


; OPTIONS FOR BONDS
; Bond parameters
continuation             = yes       ; Restarting after NPT
constraint_algorithm     = lincs     ; holonomic constraints
constraints              = all-angles ; all bonds are constrained
lincs-iter               = 1         ; accuracy of LINCS
lincs-order              = 4         ; also related to accuracy
lincs-warnangle          = 90        ; maximum angle that a bond can rotate before LINCS
      will complain, deg

; Nonbonded settings
cutoff-scheme            = Verlet    ; Buffered neighbor searching
ns_type                  = grid      ; search neighboring grid cells
```

```
31 nstlist                = 10         ; 20 fs, largely irrelevant with Verlet
32 rcoulomb               = 1.0        ; short-range electrostatic cutoff (in nm)
33 rvdw                   = 1.0        ; short-range van der Waals cutoff (in nm)
34 DispCorr               = EnerPres   ; Apply long range dispersion corrections for
       Energy and Pressure
35 table-extension        = 1          ; Extension of the potential lookup tables beyond
       the cut-off
36
37 ; Electrostatics
38 coulombtype            = PME        ; Particle Mesh Ewald for long-range electrostatics
39 pme_order              = 4          ; cubic interpolation
40 fourierspacing         = 0.16       ; grid spacing for FFT
41 vdw-type               = cut-off    ; Method for doing Van der Waals
42
43 ; Temperature coupling is on
44 tcoupl                 = nose-hoover ; Nose-Hoover thermostat
45 tc-grps                = system      ; no groups in our aragonite slab
46 tau_t                  = 0.1         ; time constant, in ps
47 ref_t                  = 300         ; reference temperature, in K
48 ; Pressure coupling is on
49 pcoupl                 = berendsen   ; Pressure coupling on in NPT
50 pcoupltype             = isotropic   ; uniform scaling of box vectors
51 tau_p                  = 1.0         ; time constant, in ps
52 ref_p                  = 1           ; reference pressure, in bar
53 compressibility        = 5e-5        ; Taken from Xaio et. al. via Shahrazad
54
55 ; Periodic boundary conditions
56 pbc                    = xyz       ; 3-D PBC
57 ; Velocity generation
58 gen_vel                = no        ; Velocity generation is off
```

B.5 Normal mode analysis

Listing B.5 nm.mdp input file for production run

```
1 title                    = CaCO3 Production MD
2
3 ; RUN CONTROL PARAMETERS
4 integrator               = nm        ; normal mode integrator
5 nsteps                   = 100000    ; 2 * 100000 = 200 ps
6 dt                       = 0.002     ; 2 fs
7 comm-mode                = Linear    ; mode for center of mass motion removal
8 nstcomm                  = 1         ; number of steps for center of mass motion removal
9
10 ; OUTPUT CONTROL OPTIONS
11 nstxout                 = 500       ; save coordinates every 1.0 ps
12 nstvout                 = 500       ; save velocities every 1.0 ps
13 nstenergy               = 500       ; save energies every 1.0 ps
14 nstlog                  = 500       ; update log file every 1.0 ps
15 nstxout-compressed      = 500       ; save the compressed coordinates every 1.0 ps
16 compressed-x-grps       = System    ; save the whole system
17
18
19 ; Parameters describing how to find the neighbors of each atom and how to calculate the
       interactions
20 nstlist         = 10              ; Frequency to update the neighbor list and long range
        forces
21 rlist           = 1.2             ; Cut-off distance for the short-range neighbor list
22 cutoff-scheme   = Verlet          ; Buffered neighbor searching
23 coulombtype     = PME-Switch      ; Treatment of long range electrostatic interactions
24 rcoulomb        = 1.0             ; Short-range electrostatic cut-off
25 rcoulomb-switch = 0.8             ;
26 vdwtype         = Cut-off         ;
27 vdw-modifier    = Potential-switch ;
28 rvdw            = 1.0             ; Short-range Van der Waals cut-off
29 rvdw-switch     = 0.8             ;
30 pbc             = xyz             ; Periodic Boundary Conditions in all 3 dimensions
31
32 ; Temperature coupling is off
```

```
33 tcoupl                  = no
34
35 ; Pressure coupling is off
36 pcoupl                  = no
37
38 ; Velocity generation
39 gen_vel                 = no        ; Velocity generation is off
```

Listing B.6 lbfgs.mdp input file for production run

```
1 ; lbfgs.mdp - used as input into grompp to generate em.tpr
2 ; Parameters describing what to do, when to stop and what to save
3 integrator  = l-bfgs             ; Conjugate-gradient minimization algorithm
4 nstcgsteep  = 10                 ; Number of correction steps to use for L-BGFS
      minimization. Higher=better&slower
5 emtol       = 0.001              ; Stop minimization when the maximum force < 0.001 kJ/
      mol/nm
6 emstep      = 0.0001             ; Minimization step size
7 nsteps      = 50000              ; Maximum number of (minimization) steps to perform
8
9 ; Parameters describing how to find the neighbors of each atom and how to calculate the
      interactions
10 nstlist         = 10            ; Frequency to update the neighbor list and long range
       forces
11 rlist           = 1.2           ; Cut-off distance for the short-range neighbor list
12 cutoff-scheme   = Verlet        ; Buffered neighbor searching
13 coulombtype     = PME-Switch    ; Treatment of long range electrostatic interactions
14 rcoulomb        = 1.0           ; Short-range electrostatic cut-off
15 rcoulomb-switch = 0.8           ;
16 vdwtype         = Cut-off       ;
17 vdw-modifier    = Potential-switch ;
18 rvdw            = 1.0           ; Short-range Van der Waals cut-off
19 rvdw-switch     = 0.8           ;
20 pbc             = xyz           ; Periodic Boundary Conditions in all 3 dimensions
```

Bibliography

[1] E. R. Cruz-Chú, S. Xiao, S. P. Patil, K. Gkagkas, and F. Gräter. Organic filling mitigates flaw-sensitivity of nanoscale aragonite. ACS Biomaterials Science & Engineering, 3(3):260–268, 2017.

Appendix C

Addendum and additions following thesis defense

This appendix is written as an addendum to Chapters 3 and 4 following discussions with thesis examiners during the defense proceedings as these chapters are reproductions of published papers, additions, alterations, and further clarifications are reported here.

C.1 Incorporating far infrared data into carbonate mineral analyses

Table 3.1 summarizes the samples used in this investigation. Samples were ground to prepare for measurement, but otherwise used "as-received." Readers interested in further sample preparation details specific to the heat-formed (H1-H5) samples are referred to their respective citations. The lab-synthesized aragonite sample, AR, was used only as a comparative sample when discussing the phase-mixture peak shifting (see Figure 3.5). As such, this data was not included in Figures 3.1 - 3.4. The observed shift of the ν_4 band for sample M1 confirms Mg-calcite and has previously been documented in the literature.[3]

An additional reference was brought to my attention related to the Far-IR measurements of calcite: L. Long, M. R. Querry, R. J. Bell, and R. W. Alexander. Optical properties of calcite and gypsum in

crystalline and powdered form in the infrared and far-infrared. Infrared Physics, 34:191–201, 1993.[2]. The data reported here agrees with my experimental data for external mode bands at approximately the same energies in the Far-IR region for calcite samples.

Further clarification on the procedure of regrinding and repressing was requested. In all cases within the manuscript, FTIR data presented represent samples that were sufficiently ground such that detected peaks ceased to narrow meaningfully, and the detected positions of the maxima moved ± 2 cm^{-1} at most, even with further repressings of the sample. The reported uncertainty in the peak positions of ± 2 cm^{-1} was for the largest observed shift, seen in the B1 external mode band. All other peaks showed less variation than this. We reported the maximum value as the paper's intent was to inform on the ATR-FTIR method and report on the novel results related to calcium carbonates.

C.2 Photoacoustic detection of weak absorption bands in infrared spectra of calcite

Figure 4.5 shows rapid-scan PAS data for calcite collected using a Gasera PA-301 cell (labeled "cantilever" and an MTEC 300 cell (labeled "microphone"). Data collection with the cantilever-based cell was not done following a dry nitrogen purge, resulting in the CO_2 doublet near 2400 cm^{-1} and a water peak near 500 cm^{-1}. The presence of these peaks does not detract from the points related to the anomalous enhancement of weak spectral peaks in calcite asserted by my co-authors and myself.

Differences in the number of scans for individual spectra, specifically those published in Figure 4.1, are related to the specifics of the instrumentation. Transmission measurements have the highest signal-to-noise ratio (followed by ATR, then PAS) and, thus, require fewer scans than ATR and PAS.

A point was raised as to why saturation of peaks cannot simply be avoided using multiple experiments with different sample quantities. While this may be a practical methodology for transmission measurements, ATR and PAS signals are affected by depth into the sample. It is challenging to control the amount of sample used in either measurement such that saturation of strong features could be avoided. More relevant for my research is that we often seek to make comparisons of relative peak intensities, as it can highlight interesting information about a sample's formation or degradation

through use. This comparison is not possible to do when comparing features from multiple spectra.

The Gasera PA-301 photoacoustic cell resonance has been partly addressed by the data presented in the supplemental materials Section 4.6.2. For additional information, the interested reader is directed to the undergraduate thesis of a past research group member, Marisa Dusseault, titled “Limits and Potential of FTIR Analysis in Archaeology”.[1]

It is tempting to characterize the vibrational bands by their full-width at half-maximum (FWHM) if saturation is the suspected cause of the weak peak enhancement. Due to the complicated peak shape of the ν_3 band owing to the multiple contributing atomic motions,[4] this is not a reasonable approach. Instead, I reiterate that the experiments performed in the paper highlight that the band is, in fact, not saturated. It remains unclear why the photoacoustic detection of ν_3 results is such a drastically different band shape compared to ATR or transmission detection.

Bibliography

[1] M. Dusseault. Limits and potential of ftir analysis in archaeology. Bachelor's thesis, Memorial University of Newfoundland, St. John's, Newfoundland, August 2019.

[2] L. L. Long, M. R. Querry, R. J. Bell, and R. W. Alexander. Optical properties of calcite and gypsum in crystalline and powdered form in the infrared and far-infrared. Infrared Physics, 34:191–201, 1993. URL https://api.semanticscholar.org/CorpusID:12236767.

[3] L. Regev, K. M. Poduska, L. Addadi, S. Weiner, and E. Boaretto. Distinguishing between calcites formed by different mechanisms using infrared spectrometry: archaeological applications. Journal of Archaeological Science, 37(12):3022–3029, 2010.

[4] B. Xu, A. Hirsch, L. Kronik, and K. M. Poduska. Vibrational properties of isotopically enriched materials: the case of calcite. RSC Advances, 8(59):33985–33992, 2018.

Appendix D

Figure use permission

Included below is a screen capture of permission granted by the publisher for use of Figure 2.1.

ELSEVIER LICENSE
TERMS AND CONDITIONS

May 24, 2023

This Agreement between Mr. Stephen Campbell ("You") and Elsevier ("Elsevier") consists of your license details and the terms and conditions provided by Elsevier and Copyright Clearance Center.

License Number	5364901422787
License date	Aug 09, 2022
Licensed Content Publisher	Elsevier
Licensed Content Publication	TrAC Trends in Analytical Chemistry
Licensed Content Title	Review in terahertz spectral analysis
Licensed Content Author	Josette El Haddad,Bruno Bousquet,Lionel Canioni,Patrick Mounaix
Licensed Content Date	Mar 1, 2013
Licensed Content Volume	44
Licensed Content Issue	n/a
Licensed Content Pages	8
Start Page	98
End Page	105
Type of Use	reuse in a thesis/dissertation
Portion	figures/tables/illustrations
Number of figures/tables/illustrations	1
Format	both print and electronic
Are you the author of this Elsevier article?	No
Will you be translating?	No
Title	Instructional Assistant
Institution name	Memorial University of Newfoundland
Expected presentation date	Dec 2022
Order reference number	00001
Portions	Figure 1
Requestor Location	Mr. Stephen Campbell 283 Prince Philip Drive Memorial University of Newfoundland Department of Physics

	St. John's, NL A1B 3X7 Canada Attn: Mr. Stephen Campbell
Publisher Tax ID	GB 494 6272 12
Total	**0.00 CAD**
Terms and Conditions	

INTRODUCTION

1. The publisher for this copyrighted material is Elsevier. By clicking "accept" in connection with completing this licensing transaction, you agree that the following terms and conditions apply to this transaction (along with the Billing and Payment terms and conditions established by Copyright Clearance Center, Inc. ("CCC"), at the time that you opened your Rightslink account and that are available at any time at http://myaccount.copyright.com).

GENERAL TERMS

2. Elsevier hereby grants you permission to reproduce the aforementioned material subject to the terms and conditions indicated.
3. Acknowledgement: If any part of the material to be used (for example, figures) has appeared in our publication with credit or acknowledgement to another source, permission must also be sought from that source. If such permission is not obtained then that material may not be included in your publication/copies. Suitable acknowledgement to the source must be made, either as a footnote or in a reference list at the end of your publication, as follows:
"Reprinted from Publication title, Vol /edition number, Author(s), Title of article / title of chapter, Pages No., Copyright (Year), with permission from Elsevier [OR APPLICABLE SOCIETY COPYRIGHT OWNER]." Also Lancet special credit - "Reprinted from The Lancet, Vol. number, Author(s), Title of article, Pages No., Copyright (Year), with permission from Elsevier."
4. Reproduction of this material is confined to the purpose and/or media for which permission is hereby given.
5. Altering/Modifying Material: Not Permitted. However figures and illustrations may be altered/adapted minimally to serve your work. Any other abbreviations, additions, deletions and/or any other alterations shall be made only with prior written authorization of Elsevier Ltd. (Please contact Elsevier's permissions helpdesk here). No modifications can be made to any Lancet figures/tables and they must be reproduced in full.
6. If the permission fee for the requested use of our material is waived in this instance, please be advised that your future requests for Elsevier materials may attract a fee.
7. Reservation of Rights: Publisher reserves all rights not specifically granted in the combination of (i) the license details provided by you and accepted in the course of this licensing transaction, (ii) these terms and conditions and (iii) CCC's Billing and Payment terms and conditions.
8. License Contingent Upon Payment: While you may exercise the rights licensed immediately upon issuance of the license at the end of the licensing process for the transaction, provided that you have disclosed complete and accurate details of your proposed use, no license is finally effective unless and until full payment is received from you (either by publisher or by CCC) as provided in CCC's Billing and Payment terms and conditions. If full payment is not received on a timely basis, then any license preliminarily granted shall be deemed automatically revoked and shall be void as if never granted. Further, in the event that you breach any of these terms and conditions or any of CCC's Billing and Payment terms and conditions, the license is automatically revoked and shall be void as if never granted. Use of materials as described in a revoked license, as well as any use of the materials beyond the scope of an unrevoked license, may constitute copyright infringement and publisher reserves the right to take any and all action to protect its copyright in the materials.
9. Warranties: Publisher makes no representations or warranties with respect to the licensed material.
10. Indemnity: You hereby indemnify and agree to hold harmless publisher and CCC, and their respective officers, directors, employees and agents, from and against any and all claims arising out of your use of the licensed material other than as specifically authorized pursuant to this license.
11. No Transfer of License: This license is personal to you and may not be sublicensed, assigned, or transferred by you to any other person without publisher's written permission.
12. No Amendment Except in Writing: This license may not be amended except in a writing signed by both parties (or, in the case of publisher, by CCC on publisher's behalf).
13. Objection to Contrary Terms: Publisher hereby objects to any terms contained in any purchase order, acknowledgment, check endorsement or other writing prepared by you, which terms are inconsistent with these terms and conditions or CCC's Billing and Payment terms and conditions. These terms and conditions, together with CCC's Billing and Payment terms and conditions (which are incorporated herein), comprise the entire agreement between you and publisher (and CCC) concerning this licensing transaction. In the event of any conflict between your obligations established by these terms and conditions and those established by CCC's Billing and Payment terms and conditions, these terms and conditions shall control.
14. Revocation: Elsevier or Copyright Clearance Center may deny the permissions described in this License at their sole discretion, for any reason or no reason, with a full refund payable to you. Notice of such denial will be made using the contact information provided by you. Failure to receive such notice will not alter or invalidate the denial. In no event

will Elsevier or Copyright Clearance Center be responsible or liable for any costs, expenses or damage incurred by you as a result of a denial of your permission request, other than a refund of the amount(s) paid by you to Elsevier and/or Copyright Clearance Center for denied permissions.

LIMITED LICENSE

The following terms and conditions apply only to specific license types:

15. **Translation**: This permission is granted for non-exclusive world **English** rights only unless your license was granted for translation rights. If you licensed translation rights you may only translate this content into the languages you requested. A professional translator must perform all translations and reproduce the content word for word preserving the integrity of the article.

16. **Posting licensed content on any Website**: The following terms and conditions apply as follows: Licensing material from an Elsevier journal: All content posted to the web site must maintain the copyright information line on the bottom of each image; A hyper-text must be included to the Homepage of the journal from which you are licensing at http://www.sciencedirect.com/science/journal/xxxxx or the Elsevier homepage for books at http://www.elsevier.com; Central Storage: This license does not include permission for a scanned version of the material to be stored in a central repository such as that provided by Heron/XanEdu.

Licensing material from an Elsevier book: A hyper-text link must be included to the Elsevier homepage at http://www.elsevier.com . All content posted to the web site must maintain the copyright information line on the bottom of each image.

Posting licensed content on Electronic reserve: In addition to the above the following clauses are applicable: The web site must be password-protected and made available only to bona fide students registered on a relevant course. This permission is granted for 1 year only. You may obtain a new license for future website posting.

17. **For journal authors:** the following clauses are applicable in addition to the above:

Preprints:

A preprint is an author's own write-up of research results and analysis, it has not been peer-reviewed, nor has it had any other value added to it by a publisher (such as formatting, copyright, technical enhancement etc.).

Authors can share their preprints anywhere at any time. Preprints should not be added to or enhanced in any way in order to appear more like, or to substitute for, the final versions of articles however authors can update their preprints on arXiv or RePEc with their Accepted Author Manuscript (see below).

If accepted for publication, we encourage authors to link from the preprint to their formal publication via its DOI. Millions of researchers have access to the formal publications on ScienceDirect, and so links will help users to find, access, cite and use the best available version. Please note that Cell Press, The Lancet and some society-owned have different preprint policies. Information on these policies is available on the journal homepage.

Accepted Author Manuscripts: An accepted author manuscript is the manuscript of an article that has been accepted for publication and which typically includes author-incorporated changes suggested during submission, peer review and editor-author communications.

Authors can share their accepted author manuscript:

- immediately
  - via their non-commercial person homepage or blog
  - by updating a preprint in arXiv or RePEc with the accepted manuscript
  - via their research institute or institutional repository for internal institutional uses or as part of an invitation-only research collaboration work-group
  - directly by providing copies to their students or to research collaborators for their personal use
  - for private scholarly sharing as part of an invitation-only work group on commercial sites with which Elsevier has an agreement
- After the embargo period
  - via non-commercial hosting platforms such as their institutional repository
  - via commercial sites with which Elsevier has an agreement

In all cases accepted manuscripts should:

- link to the formal publication via its DOI
- bear a CC-BY-NC-ND license - this is easy to do
- if aggregated with other manuscripts, for example in a repository or other site, be shared in alignment with our hosting policy not be added to or enhanced in any way to appear more like, or to substitute for, the published journal article.

Published journal article (JPA): A published journal article (PJA) is the definitive final record of published research that appears or will appear in the journal and embodies all value-adding publishing activities including peer review co-ordination, copy-editing, formatting, (if relevant) pagination and online enrichment.

Policies for sharing publishing journal articles differ for subscription and gold open access articles:

Subscription Articles: If you are an author, please share a link to your article rather than the full-text. Millions of researchers have access to the formal publications on ScienceDirect, and so links will help your users to find, access, cite, and use the best available version.

Theses and dissertations which contain embedded PJAs as part of the formal submission can be posted publicly by the awarding institution with DOI links back to the formal publications on ScienceDirect.

If you are affiliated with a library that subscribes to ScienceDirect you have additional private sharing rights for others' research accessed under that agreement. This includes use for classroom teaching and internal training at the institution (including use in course packs and courseware programs), and inclusion of the article for grant funding purposes.

Gold Open Access Articles: May be shared according to the author-selected end-user license and should contain a CrossMark logo, the end user license, and a DOI link to the formal publication on ScienceDirect.

Please refer to Elsevier's posting policy for further information.

18. **For book authors** the following clauses are applicable in addition to the above: Authors are permitted to place a brief summary of their work online only. You are not allowed to download and post the published electronic version of your chapter, nor may you scan the printed edition to create an electronic version. **Posting to a repository:** Authors are permitted to post a summary of their chapter only in their institution's repository.

19. **Thesis/Dissertation**: If your license is for use in a thesis/dissertation your thesis may be submitted to your institution in either print or electronic form. Should your thesis be published commercially, please reapply for permission. These requirements include permission for the Library and Archives of Canada to supply single copies, on demand, of the complete thesis and include permission for Proquest/UMI to supply single copies, on demand, of the complete thesis. Should your thesis be published commercially, please reapply for permission. Theses and dissertations which contain embedded PJAs as part of the formal submission can be posted publicly by the awarding institution with DOI links back to the formal publications on ScienceDirect.

Elsevier Open Access Terms and Conditions

You can publish open access with Elsevier in hundreds of open access journals or in nearly 2000 established subscription journals that support open access publishing. Permitted third party re-use of these open access articles is defined by the author's choice of Creative Commons user license. See our open access license policy for more information.

Terms & Conditions applicable to all Open Access articles published with Elsevier:

Any reuse of the article must not represent the author as endorsing the adaptation of the article nor should the article be modified in such a way as to damage the author's honour or reputation. If any changes have been made, such changes must be clearly indicated.

The author(s) must be appropriately credited and we ask that you include the end user license and a DOI link to the formal publication on ScienceDirect.

If any part of the material to be used (for example, figures) has appeared in our publication with credit or acknowledgement to another source it is the responsibility of the user to ensure their reuse complies with the terms and conditions determined by the rights holder.

Additional Terms & Conditions applicable to each Creative Commons user license:

CC BY: The CC-BY license allows users to copy, to create extracts, abstracts and new works from the Article, to alter and revise the Article and to make commercial use of the Article (including reuse and/or resale of the Article by commercial entities), provided the user gives appropriate credit (with a link to the formal publication through the relevant DOI), provides a link to the license, indicates if changes were made and the licensor is not represented as endorsing the use made of the work. The full details of the license are available at http://creativecommons.org/licenses/by/4.0.

CC BY NC SA: The CC BY-NC-SA license allows users to copy, to create extracts, abstracts and new works from the Article, to alter and revise the Article, provided this is not done for commercial purposes, and that the user gives appropriate credit (with a link to the formal publication through the relevant DOI), provides a link to the license, indicates if changes were made and the licensor is not represented as endorsing the use made of the work. Further, any new works must be made available on the same conditions. The full details of the license are available at http://creativecommons.org/licenses/by-nc-sa/4.0.

CC BY NC ND: The CC BY-NC-ND license allows users to copy and distribute the Article, provided this is not done for commercial purposes and further does not permit distribution of the Article if it is changed or edited in any way, and provided the user gives appropriate credit (with a link to the formal publication through the relevant DOI), provides a link to the license, and that the licensor is not represented as endorsing the use made of the work. The full details of the license are available at http://creativecommons.org/licenses/by-nc-nd/4.0. Any commercial reuse of Open Access articles published with a CC BY NC SA or CC BY NC ND license requires permission from Elsevier and will be subject to a fee.

Commercial reuse includes:

- Associating advertising with the full text of the Article
- Charging fees for document delivery or access
- Article aggregation
- Systematic distribution via e-mail lists or share buttons

Posting or linking by commercial companies for use by customers of those companies.

20. **Other Conditions**:

v1.10

Questions? E-mail us at customercare@copyright.com.